FACULTY OF ENGINEERING
AND ARCHITECTURE

Human Electromagnetic Field Exposure from Ultra Small Cell and Massive MIMO Technologies

Sergei Shikhantsov

Doctoral dissertation submitted to obtain the academic degree of
Doctor of Engineering Physics

Supervisors

Prof. Wout Joseph, PhD - Prof. Piet Demeester, PhD

Department of Information Technology
Faculty of Engineering and Architecture, Ghent University

May 2022

GHENT
UNIVERSITY

FACULTY OF ENGINEERING AND ARCHITECTURE

Human Electromagnetic Field Exposure from Ultra Small Cell and Massive MIMO Technologies

Sergei Shikhantsov

Doctoral dissertation submitted to obtain the academic degree of
Doctor of Engineering Physics

Supervisors
Prof. Wout Joseph, PhD - Prof. Piet Demeester, PhD

Department of Information Technology
Faculty of Engineering and Architecture, Ghent University

May 2022

GHENT UNIVERSITY

ISBN 978-94-6355-587-6
NUR 959, 926
Wettelijk depot: D/2022/10.500/28

Members of the Examination Board

Chair

Prof. Patrick De Baets, PhD, Ghent University

Other members entitled to vote

Prof. Emile Björnson, PhD, KTH Royal Institute of Technology, Sweden
Prof. Em. Marc Moeneclaey, PhD, Ghent University
Prof. Ingrid Moerman, PhD, Ghent University
Prof. Claude Oestges, PhD, Université catholique de Louvain
Prof. Arno Thielens, PhD, Ghent University

Supervisors

Prof. Wout Joseph, PhD, Ghent University
Prof. Piet Demeester, PhD, Ghent University

Acknowledgment

First of all, I would like to thank my promoter Prof. Wout Joseph for giving me the opportunity to work on this project and for his support during these years. He was always there to share his vast knowledge and experience in the field, guiding me through my first steps as a researcher, while offering full creative freedom. I also thank my co-promoter Prof. Piet Demeester for the fruitful feedback during our regular meetings.

Secondly, I would like to thank my friends and colleagues who contributed (sometimes unknowingly) to the contents of the present book and my heart. Arno, for all the enlightening discussions, relentlessly scrutinizing my every written word, and always setting the bar high. Sam, for epic journeys (not only scientific) and sharing truly unforgettable moments. Günter, Leen and Emmeric, for teaching me both software and hardware operation skills, and helping out on countless occasions. Marwan and Rodney for great beans and great company. Kris, for his help with network and system administration. Maarten, for setting the mood. Clea, for emphatically believing in me with no apparent reason. Mechant, for teaching me real science friction. Gloria, for showing Belgian nature at its finest. Xiajie, for keeping an eye on my vitals.

In addition, I would like to thank Prof. Jasper De Bock and Prof. Dick Botteldooren, who's lectures I was lucky enough to attend.

Last but not least, one special word of appreciation goes to Isabelle and Judith for managing and explaining to me (time and again) the most entangled administrative procedures.

Ghent, April, 2022
Sergei Shikhantsov

Table of Contents

List of Figures

List of Tables

List of Acronyms

0-9

1G	First Generation
2G	Second Generation
3G	Third Generation
3GPP	3rd Generation Partnership Project
4G	Forth Generation
5G	Fifth Generation

A

AP	access point

B

BS	base station

C

CBBF	codebook beamforming
CDF	Cumulative Distribution Function
CENELEC	European Committee for Electrotechnical Standardization
CSI	channel-state information
CU	control unit

D

DC	duty cycle
DL	downlink
DMaMIMO	Distributed Massive MIMO
DoA	direction-of-arrival
DoD	direction-of-departure

E

EGT	Equal Gain Transmission
EIRP	Equivalent Isotropic Radiated Power
EL	Extremely Large Aperture Arrays
EM	Electromagnetic
EMF	Electromagnetic field

F

FDTD	Finite-Difference Time-Domain
FS-LOS	Free-Space Line-of-Sight
FWHM	full width half maximum

G

GoB	grid-of-beams
GSM	Global System for Mobile Communications

I

ICNIRP	International Commission of Non-Ionizing Radiation Protection
IEC	International Electrotechnical Commission
IEEE	Institute of Electrical and Electronics Engineers

L

LAN	Local Area Network
L-BFGS-B	Limited memory Broyden–Fletcher–Goldfarb–Shanno algorithm with bound constraints
LOS	line-of-sight
LTE	Long Term Evolution

M

MIMO	multiple-input multiple-output
MPR	matrix power ratio
MRT	Maximum Ratio Transmission
MU-MIMO	Multi-User MIMO

N

NLOS	non-line-of-sight
NR	New Radio

NTP	Network Time Protocol

P

PDF	Probability Density Function
PEC	perfect electric conductor
PML	Perfectly Matched Layer
PL	Path Loss
psSAR_{10g}	peak-spatial Specific Absorption Rate averaged over a 10-g cube
PW	plane wave

R

RAN	radio access network
RF	radio-frequency
RMS	root-mean-square
RT	Ray-Tracing

S

SAR	Specific Absorption Rate
SIR	signal-to-interference ratio
SNR	signal-to-noise ratio
SVS	singular value spread

T

ToF	time-of-flight

U

UE	user equipment
UL	uplink
UMTS	Universal Mobile Telecommunications Service
UTD	Uniform Theory of Diffraction

W

WLAN	Wireless LAN

Z

ZF	Zero-Forcing

Nederlandse samenvatting

Moeiteloze draadloze communicatie wordt tegenwoordig beschouwd als een integraal en onmisbaar deel van ons alledaags leven. De continu stijgende vraag naar connectiviteit en het grote aantal opkomende innovatieve industriële toepassingen sturen de ontwikkeling van vijfdegeneratienetwerken (5G) en het enthousiasme voor de invoering ervan aan. Wereldwijd wordt het mobiele dataverkeer dan ook verwacht te groeien met 40

De snelle uitrol van 5G-pilootnetwerken in landen over de hele wereld geeft tevens aanleiding tot bezorgdheid bij de bevolking over de menselijke blootstelling aan radiofrequente (RF) elektromagnetische velden (EMV) opgewekt door de nieuwe technologieën. In Europa wordt het niveau van omgevings-RF-EMV wettelijk ingeperkt door regelgevende instanties die zich daarvoor baseren op aanbevelingen en richtlijnen uitgevaardigd door de International Commission on Non-Ionizing Radiation Protection (ICNIRP). Soms worden op nationaal of regionaal niveau ook strengere normen opgelegd (in België, Zwitserland, etc.). Naleving van de bestaande voorschriften wordt gewoonlijk geëvalueerd aan de hand van een rechtstreekse meting van de EMV in een operationeel netwerk, gebruik makend van gevestigde meetprocedures. Recent uitgerolde 5G-netwerken moeten hun volledig potentieel qua dataverkeer echter nog bereiken, wat er voor zorgt dat meetresultaten nog niet representatief kunnen zijn. Daarenboven werden de gevestigde meetprocedures ontwikkeld in het kader van mobiele netwerken van de voorgaande generaties (2G–4G) waardoor ze eerst geactualiseerd moeten worden om 5G-specificiteiten correct te kunnen evalueren. Naast metingen worden ook numerieke simulaties veelvuldig ingezet om de RF-EMV-blootstelling in mensen te voorspellen. Maar om de EMV geïnduceerd door 5G-basisstations in mensen te modelleren werd tot nog toe geen diepgaande methode voorgesteld. Ten slotte zijn de huidige beperkingen gebaseerd op aannames specifiek voor de netwerken van vorige generaties, dewelke mogelijks niet meer gelden.

Dit proefschrift behandelt de numerieke studie van de downlink-blootstelling (m.a.w. de blootstelling aan RF-EMV uitgestraald door de basisstations) geïnduceerd door twee 5G-technologieën: 5G New Radio (NR) massieve Multiple-Input-Multiple-Output (MIMO) en ultrakleine cellen (zgn. ATTO-cellen). De eerste zal naar verwachting de dominante technologie worden in basisstations in buitenshuisnetwerken. Ze gebruikt een grote antenne-array met tientallen tot honderden elementen om de downlink-transmissie te focussen in de ruimte via dynamische bundelvorming of om driedimensionale hotspots rond het gebruikersdoelwit te creëren door middel van geprecodeerde MIMO-technieken. De tweede is gericht op toekomstige

industriële faciliteiten en toepassingen in een Industry 4.0-context. De gebruikers in zulke ultrakleine celnetwerken zijn een grote schare autonome robots die een constante verbinding met lage latentie en hoge snelheid vereisen. In dit geval bestaat het basisstation uit een groot aantal gekoppelde ATTO-cellen, rechtstreeks ingebouwd in de fabrieksvloer, die elk enkel in dienst staan van een gebruiker er recht bovenop.

Het proefschrift bevat acht hoofdstukken. Hoofdstuk 1 introduceert de bestudeerde technologieën in meer detail en bediscussieert de blootstellingsvoorschriften in deze context. Hoofdstukken 2 tot 7 worden hieronder kort samengevat.

In Hoofdstuk 2 wordt de blootstelling onderzocht van een arbeider op een fabrieksvloer bedekt met ATTO-cellen. De Finite-Difference-Time-Domain (FDTD) methode wordt gebruikt om de EMV geïnduceerd in de benen van een realistisch menselijk fantoommodel te berekenen bij simultane bestraling door meerdere operationele cellen. Daarnaast wordt het effect van EMV-interferentie op de resulterende fantoomblootstelling geëvalueerd. Ten slotte wordt de maximale blootstelling op de vloer voor een gegeven uitgangsvermogen van de cellen bepaald en vergeleken met de gangbare normen.

In Hoofdstuk 3 wordt een methode voorgesteld om de blootstelling te bepalen van een gebruiker in een hotspot gecreëerd door een basisstation met massieve MIMO. De voorgestelde aanpak combineert een FDTD-methode om de blootstelling te bepalen met een Ray-Tracing (RT) methode om de RF-propagatie te modelleren en de eigenschappen van het draadloze kanaal te berekenen. Het geval van een basisstation dat Equal Gain Transmission toepast in een binnenhuisomgeving wordt bestudeerd. De verkregen kanalen worden vergeleken met theoretische kanalen die doorgaans gebruikt worden in de theoretische analyse van de efficiëntie van massieve MIMO. De EMV geïnduceerd rond het fantoomhoofd en de lokale piekblootstelling in het hoofd worden bepaald met de FDTD-methode. Gebaseerd op deze resultaten wordt het maximale uitgangsvermogen van het basisstation bepaald waarmee nog voldaan wordt aan de ICNIRP-richtlijnen.

In Hoofdstuk 4 wordt de methodologie geïntroduceerd in Hoofdstuk 3 uitgebreid om ook rekening te kunnen houden met de effecten die de koppeling tussen een gebruikerstoestel (UE) en het fantoomlichaam heeft op het kanaal, de hotspot, en de resulterende blootstelling. Het praktisch meer relevante Maximum Ratio Transmission (MRT) schema wordt bestudeerd in dezelfde omgeving als in Hoofdstuk 3. De grootte en de piekintensiteit van de hotspot gevormd rond een UE gepositioneerd nabij het hoofd worden bestudeerd in scenario's zonder rechtstreeks propagatiepad tussen basisstation en UE. De hotspotwinst in vergelijking met de path-lossfading wordt afgeleid van de verkregen EMV-distributies. De waarschijlijkheid dat de piekblootstelling zich voordoet in de nabijheid van de UE wordt op een stochastiche wijze berekend op basis van de resulaten van een grote set aan RT-omgevingen. Er wordt ten slotte aangetoond dat de ICNIRP-richtlijnen conservatief zijn in het limiteren van de geïnduceerde lokale blootstelling met betrekking tot de EMV-niveaus in de hotspot.

In Hoofdstuk 5 wordt een vergelijkende studie voorgesteld tussen topologieën met gecolloceerde en gedistribueerde massieve MIMO basisstations vanuit het

standpunt van menselijke RF-EMV-blootstelling. De methodologie ontwikkeld in Hoofdstukken 3 en 4 wordt toegepast op een industrieel binnenshuisomgevingsmodel (de zgn. "factory of the future"). De blootstelling van arbeiders die zich verplaatsen in de fabriekshal wordt bepaald als functie van de afstand van de UE tot het hoofd van de gebruiker. Er wordt aangetoond dat het gedistribueerde systeem een hogere hotspotwinst produceert, maar dat de path loss gemiddeld ook hoger ligt. Er wordt tevens aangetoond dat hoewel onder een bepaalde afstand tussen de UE en het hoofd van de gebruiker de downlink-blootstelling vrijwel constant blijft, de hotspotpiek en de locatie van de UE uit elkaar gaan, wat het basisstation eventueel aanspoort zijn uitgangsvermogen te verhogen. Inzichten in methoden om de blootstelling aan EMV in 5G-hotspotscenario's te bepalen worden voorzien.

In Hoofdstuk 6 wordt in een buitenshuisomgeving dynamische bundelvorming met andere massieve MIMO-technieken vergeleken. In een buitenshuisomgeving zijn gebruikers gewoonlijk blootgesteld in het verre veld van het basisstation, en hun blootstelling is rechtstreeks verbonden met de tijdsgemiddelde inkomende EMV, dewelke op hun beurt afgeleid worden van de tijdsafhankelijke antennewinst van het basisstation. De tijdsafhankelijke antennewinst wordt in dit Hoofdstuk berekend gedurende verschillende multi-gebruikersscenario's, waarbij de veranderlijke gebruikersdistributies stochastich gesimuleerd worden en de EMV-propagatie gemodelleerd via de RF-methode, en de tijdsgemiddelde winst wordt bepaald volgens de ICNIRP-richtlijnen. De maximale tijdsgemiddelde antennewinst wordt gerapporteerd en vergeleken met state-of-the-art-resultaten gebaseerd op niet-deterministische propagatiemodellen, waarbij een goede overeenkomst wordt bekomen. De voorgestelde resulaten kunnen gebruikt worden om praktische nalevingsgrenzen te bepalen bij 5G-basisstationuitrollen.

In Hoofdstuk 7 wordt de experimentele validatie van RT als methode voor het modelleren van massieve MIMO-propagatie uitgevoerd. De meetcampagne bevindt zich buitenshuis met een massieve MIMO-basisstationtestbed. De positie van de UE wordt vanop afstand bestuurd gebruik makend van een robotisch positioneringsysteem met hoge precisie, en de staat en de positie van het draadloze kanaal worden gelijktijdig opgenomen. De resultaten van deze metingen worden vergeleken met de RT-simulaties met een model van de meetlocatie. De grootte van de correlatie tussen de kanaalstaatvectoren is gerelateerd aan de grootte van de hotspot gecreëerd door het basisstation. De simulaties zijn in staat de kanaalcorrelatie op verschillende plaatsen in de omgeving nauwkeurig te voorspellen, wat de bruikbaarheid van de RT-methode voor het voorspellen van massieve MIMO-propagatie aantoont.

In Hoofdstuk 8 worden ten slotte de conclusies besproken en de mogelijke toekomstige onderzoeksrichtingen geschetst.

Het onderzoek dat hierboven geschetst resulteerde in vijf aan peer review onderworpen publicaties als eerste auteur in internationele tijdschriften en werd gepresenteerd op zes wetenschappelijke congressen.

English Summary

Effortless wireless communication is nowadays perceived as an integral, essential part of our everyday life. Our ever-increasing demand for connectivity as well as the emerging innovative industrial applications drive the development and an eager adoption of the fifth-generation (5G) networks. The global mobile traffic growth is estimated at over 40% per year, with 5G surpassing the technologies of the previous generation (4G) in the number of new subscriptions in Q2 2021.

The rapid pilot deployment of 5G around the world also raises the public concern for the human radio frequency (RF) Electromagnetic field (EMF) exposure to these new technologies. In Europe, the environmental Electromagnetic field (EMF) levels are legally limited by regulatory bodies based on the recommendations of the International Commission on Non-Ionizing Radiation Protection (ICNIRP). Sometimes more stringent local national and regional policies (e.g., in Belgium, Switzerland) are adopted. The compliance to the existing regulations is usually assessed by directly measuring the EMF in an operating network, according to the established procedures. However, recently deployed 5G networks are yet to reach their full load capacity, which makes the measurement results not representative. Additionally, the measurement procedures were developed to be used in networks of the previous generations and need to be updated to account for 5G-specific effects. As an alternative, numerical simulations are extensively utilized to predict the RF EMF exposure in humans. And yet, no method to model the interaction of the human body with the EMF induced by the 5G BSs was proposed. On top of that, current restrictions themselves are based on assumptions specific to the previous generations' technologies, which may not hold any longer.

This dissertation presents a numerical study of the downlink (DL) exposure induced by two 5G technologies: 5G New Radio massive Multiple-Input Multiple-Output (MIMO) and ultra-small cells. The former is expected to gradually take over and eventually fully replace the existing outdoor cellular sites. It employs a large antenna array (hundreds of elements and more) at the base station to focus the DL transmission in space via dynamic beamforming or creates 3D hot-spots around target users using MIMO precoding schemes. The latter is targeted towards the future industrial facilities and applications in the context of Industry 4.0. The users in such ultra-small cell networks are multitudes of autonomous robots, requiring a constant low-latency and high-speed connection. The BS is made up of a large number of interconnected (ultra-small) cells, built-in directly into the factory floor surface, each serving only the user right on top of it.

The dissertation consist of eight chapters. Chapter 1 introduces the studied

technologies in more detail and discusses the existing exposure regulations in this context. Chapter 8 draws conclusions and outlines the prospective future research directions. Chapters 2 to 7 are briefly summarized below.

In Chapter 2, the exposure of a human worker on top of the factory floor covered with ultra-small cells (ATTO-floor) is studied. The Finite-Difference Time-Domain (FDTD) method is used to calculate the EMF induced in the legs of a realistic human phantom model by the simultaneous radiation of multiple cells. The effect of the EMF interference on the resulting phantom exposure was evaluated. Additionally, the maximum exposure on the floor for the given output cell power is established and compared with the existing guidelines.

In Chapter 3, a methodology to assess the exposure of a user in a hot-spot created by a massive MIMO BS is proposed. The proposed method combines the FDTD method of exposure assessment with the Ray-Tracing (RT) method to model the RF propagation and calculate the wireless channel properties. A case of the BS performing the Equal Gain Transmission is studied in an indoor environment. The obtained channels are compared to the theoretical ones, which are common in the theoretical analysis of the massive MIMO efficiency. The EMF induced around the phantom's head and the localized peak exposure induced inside it are evaluated using the FDTD method. Based on these results, the maximum BS output power complying to the ICNIRP guidelines is derived.

In Chapter 4, the methodology introduced in Chapter 3 is extended to account for the effects that the UE coupling with the phantom body has on the channel, the hot-spot, and the resulting exposure. A more practically relevant Maximum Ratio Transmission scheme is studied in the same environment. The size and peak intensity of the hot-spot formed around the UE positioned close to the phantom's head are studied in scenarios with no direct BS-to-UE propagation paths. The hot-spot EMF gain over Path Loss fading is derived from the obtained EMF distributions. The probability of having the peak localized exposure in proximity of the UE is calculated from the results of a large set of the RT environments in a stochastic way. It is shown that the ICNIRP guidelines are conservative in limiting the induced localized exposure with respect to the EMF levels in the hot-spot.

In Chapter 5, a comparative study of the collocated and distributed massive MIMO BS topologies from the human exposure point of view is presented. The methodology developed in Chapters 3 and 4 is applied to an industrial indoor environment model ("factory of the future"). The exposure of human workers moving around the factory floor is assessed as a function of the head to UE separation distance. It was demonstrated that the distributed system produces higher hot-spot EMF gain over fading, but also experiences higher (on average) path loss. It is also shown that even thought below a certain head-UE separation distance the exposure remains nearly constant, the hot-spot peak and the UE location diverge, which might prompt the BS to increase its output power. Insights into the possible EMF assessment methods for 5G hot-spot scenarios are provided.

In Chapter 6, an outdoor urban environment comparing the beamforming and massive MIMO BSs is studied. The users outdoors are usually exposed in the far-field region of the BS, and their exposure is directly related to the time-average

incident EMF, which is in turn derived from the time-average BS gain. We evaluate the gain that the BS outputs in multi-user scenarios and calculate its time-average according to the ICNIRP guidelines by simulating a distribution of users in the environment and modeling the EMF propagation with the RT method. The maximum time-averaged BS gain is reported and compared with the state-of-the art results based on the non-deterministic propagation modeling techniques, showing good agreement. The presented results can be applied to establish the compliance boundaries of practical 5G BS deployments.

In Chapter 7, we conduct the experimental validation of the RT as a method for the massive MIMO propagation modeling used throughout the thesis. The measurement campaign was carried out indoors with a real massive MIMO BS testbed. The UE location was remotely controlled by means of a high-precision robotic positioning system, and its wireless channel state and position were synchronously recorded. We compare the results of these measurements to the RT simulations performed in a model of the measurement site. The amount correlation between the channel state vectors is related to the hot-spot size that the BS produced. The simulations are able to accurately predict the channel correlation at different locations in the environment, which demonstrates the suitability of the RT method as a tool for the massive MIMO propagation prediction.

The research outlined above resulted in five first-author publications in international peer-reviewed journals, and was presented at six international conferences.

1 Introduction

1.1 Context and Motivation

Today's technologically developed societies are hardly imaginable without ubiquitous wireless connectivity readily available to everyone. This is most often achieved by transmitting and receiving the Electromagnetic (EM) waves in the radio-frequency (RF) spectrum, ranging from hundreds of MHz to around 10 GHz. Radio access networks (RANs) of the first generation (1G) were launched in the early 1980s. They allowed mobile users to perform voice calls and were the first to realize the cellular concept [1], which became the basis for the modern RANs. In cellular networks a base station (BS) provides services within its designated area or cell. The second generation (2G) networks introduced the Global System for Mobile Communications (GSM) standard which superseded 1G in Europe in the 1990s. The third generation (3G) Universal Mobile Telecommunications Service (UMTS) systems appeared in the 2000s, allowing for faster data transfer rates. The fourth generation (4G) Long Term Evolution (LTE) networks were deployed in the 2010s and are currently leading in number of worldwide subscriptions and the net mobile data traffic. While in the US the 2G/3G major network operators started to shut down the 2G/3G service, and it is expected to be largely phased out in 2022 [2], in Europe these legacy technologies are likely to endure another five or six years [3]. As we are entering the third decade of the 21st century, pilot deployments of the fifth generation (5G) networks are under way [4–6], augmenting the existing cellular sites.

Cell types are usually categorized based on the size of the area they cover. Dense outdoor urban networks comprise cells up to around 500 m in size, called *microcells*. Indoor networks are usually spanned by shorter range access points - *femtocells*. An important feature that is shared by all currently (widely) adopted technologies is that the user is located in the *far-field* region of the base station (BS) antenna in the vast majority of the usage scenarios.

Two implications of this are relevant for further discussion. First, the user is not *coupled* with the BS antenna, meaning that the user body location or position does not perturb the BS transmission. Second, in the far-field region, the EM waves radiated from the BS antenna diverged enough to be regarded as a collection of plane wave-fronts. This means that the EM field (EMF) incident at the user during the downlink (DL) transmission can be accurately represented by a stochastic combination of plane waves, originating from various propagation paths between the BS and the user. Interference between the signals arriving from different propagation paths results in the *fast-fading* phenomenon, i.e. random variation of the received signal strength over short distances [7]. It can be accurately described by statistical models, e.g., Rician fading model [8], that assign the amplitudes and phases of the received signals based on a probability density function. We further show that such approach is not applicable in many 5G scenarios.

The 5G technologies studied in this thesis employ BSs consisting of a large number of individually controlled antenna elements (see Fig. 1.1). In the 5G New Radio (5G-NR) the focusing is often realized via *beamforming*. It leverages the large array's ability to dynamically adjust its *radiation pattern*, steering narrow, high-gain lobes (or "beams") in the desired direction [9, 10]. Put simply, to produce a beam in a given direction, the array elements' phases are set such that the signals at a large distance in that direction arrive with equal phases and interfere constructively, thus boosting the total received signal. The set of directions in which the beams can be generated is predetermined (fixed for a given BS), tiling the cell in the BS's direction-of-departure (DoD) space. This type of beamforming is referred to as the *grid-of-beams* (GoB) [11] or *codebook beamforming* (CBBF) [12], depending on the underlying implementation.

Massive multiple-input multiple-output (MIMO) [13, 14] departs from the beam-steering in the angular domain of the BS's DoDs and instead sets the transmission weighs of the BS antenna elements according to the real-time wireless channel estimate and a *precoding* scheme it implements [15, 16]. The channel is estimated by measuring the unique *pilot sequences* transmitted uplink by the UEs and utilizing the channel reciprocity [7]. The most commonly analyzed MIMO precoding scheme is the Maximum Ratio Transmission (MRT), also known as conjugate precoding/beamforming, has been around for at least half a century [7, 17], and is known to deliver the maximum theoretically achievable received signal strength (given the total power constraint). Importantly, when used with a very

large array, and given *favorable* propagation conditions, the same precoding scheme results in the interference cancellation between the target receivers [18]. A more precise meaning of the propagation conditions being favorable will be discussed in Chapter 3 and 4. If fulfilled, this allows to transmit using the same time-frequency resources to multiple, possibly closely-spaced, users. Such *multiplexing* of users is not possible with the CBBF if they are too close to each other and share a beam.

The aforementioned properties of these 5G technologies set them apart from the previous generations' technologies in the way they interact with the human body. Updating the exposure protection regulations for 5G is an essential step in promoting its wide adoption. Therefore, it is crucial to have accurate numerical methods to predict and quantify the 5G-specific exposure aspects. **The aim of this thesis is to design the numerical approaches for modelling of the human EMF exposure induced by the BSs in the sub-6 GHz 5G wireless networks.**

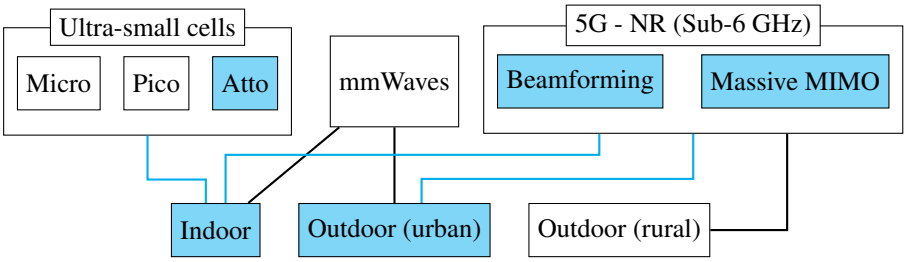

Figure 1.1: An overview of 5G concepts and scenarios. Technologies studied in this thesis are highlighted with blue.

1.1.1 Human EMF exposure protection guidelines

The EMF in the RF part of the spectrum is non-ionizing, meaning that the photons at these frequencies do not carry enough energy to completely remove an electron from an atom or molecule. Human RF EMF exposure assessment and protection is aimed at determining and limiting the temperature increase in the human body due to the EMF absorption. The thermoregulatory response of the human body has been modelled numerically [19, 20], tested experimentally [21, 22] and extensively applied to situations where the temperature elevation is actually desirable, e.g., in the RF-induced hyperthermia cancer treatment. The International Commission on Non-Ionizing Radiation Protection (ICNIRP) issues guidelines for limiting the exposure [23, 24], that are used as a reference for setting the local regulations by the governmental bodies. In the frequency range from 100 kHz to 6 GHz, the physical quantity used to assess the human EMF exposure is the Specific Absorption Rate (SAR), which is the EMF power absorbed per unit of mass (W/kg). The basic

restriction limits are established by the ICNIRP for the SAR averaged over the whole body (SAR_{wb}) and the spatial maximum of local SAR, averaged over a cube volume, containing 10 g of tissue ($psSAR_{10g}$). A threshold of $1\,^{\circ}\mathrm{C}$ is set as a limit for the body core temperature elevation due to the EMF absorption, which is equivalent to 4 W/kg SAR_{wb}, averaged over a 30-minute interval. A factor of 10 is applied as a safety margin to set the occupational SAR_{wb} limits (for workers who can actively mitigate the exposure risks), giving 0.4 W/kg. To protect the general public, unaware of the possible exposure, an even larger safety factor of 50 was set, resulting in a more strict 0.08 W/kg SAR_{wb} basic restriction. Similar reasoning is used to set the basic restrictions on $psSAR_{10g}$, for which a 6-minute averaging is required. For $psSAR_{10g}$ assessed in head and torso the general public basic restriction value of 2 W/kg is set (10 W/kg for workers). The basic restriction for $psSAR_{10g}$ in limbs is 4 W/kg for general public and 20 W/kg for workers. These basic restrictions must be satisfied when measuring the SAR directly in the human phantoms, e.g., in compliance testing of body-worn or handheld equipment according to the Institute of Electrical and Electronics Engineers (IEEE), European Committee for Electrotechnical Standardization (CENELEC), or International Electrotechnical Commission (IEC) standard procedures [25, 26]. In many countries (including Belgium), every consumer device has to undergo such testing before entering the market. However, in real scenarios users of mobile devices are exposed not only by the user device itself (uplink exposure), but also by the BS that provides service to it (DL exposure). It is far more practical to conduct environmental EMF measurements than to measure the SAR directly in such scenarios, and ICNIRP provides reference levels for the incident power density and the E-field strength, that are aimed to assure an equivalent level of the exposure protection. These levels are based on the experimental data [27–29] and verified with exhaustive Finite-Difference Time-Domain (FDTD) simulations using high-precision anatomical human models [30–32].

The FDTD approach for the temperature increase and SAR assessment was validated empirically using direct measurements in rats [33], flat [34] and cylindrical [35] phantoms, and patient-specific Magnetic Resonance Imaging (MRI) human models. The relative error of the SAR calculated with the FDTD method was found to be around 5% [35, 36], which is far below the SAR variation due to the body morphology, posture [37], and tissue dielectric parameters [38, 39]. Moreover, in [37, 40], the effects of the whole-body and organ-specific resonance on SAR was studied for frequencies up to 3 GHz in phantoms exposed by a plane-wave, highlighting the importance of the phantom heterogeneity for numerical human exposure estimation. Due to its versatility in handling lossy bodies of complex geometry, the FDTD approach remains to be the de facto standard numerical tool for the RF-EMF dosimetry [41, 42].

Extensive numerical studies of the exposure to the 4G and earlier generation's

BSs were conducted to verify their compliance with the established exposure protection guidelines. In [43], the exposure of a user in the near field of a single-antenna GSM BS was calculated by performing full-wave FDTD simulations with a heterogeneous human phantom. In [37, 40], the effects of the whole-body and organ-specific resonance on SAR was studied for frequencies up to 3 GHz in phantoms exposed by a plane-wave. In [44], the near-field exposure to Bluetooth and WiFi sources at 2.4 GHz in realistic scenarios was studied using the FDTD method. In [45, 46], a surrogate model was built based on a large set of SAR estimates obtained with the Huygens box excitation of the FTDTD domain, allowing a fast exposure estimation to a WiFi BS in diverse indoor scenarios. In [47], approximate formulas for fast exposure estimation in the radiating near- and far-field of a generic BS antenna (up to 5 GHz) was proposed, based on the plane-wave FDTD simulations. In [48], the SAR resulting from a combined simultaneous exposure to multiple sources was estimated using fast surrogate modelling-based method. Developed to model the exposure in the previous generations' networks, these methods are not readily applicable in most 5G scenarios for reasons described in the next section.

1.1.2 Exposure aspects of 5G

Numerical methods to model the exposure of humans to the 5G array BSs have attracted considerable attention in recent years. In [49], the SAR induced by a 64-element BS was evaluated at 3.7 GHz and 14 GHz in FDTD, comparing different human phantoms. In [50], the 3rd Generation Partnership Project (3GPP) channel model was used to generate the EMF incident at a human phantom in the FDTD domain at 3.5 GHz. In [51], a combination of the spherical near-field transformation and the FDTD methods was applied to study the SAR and temperature rise induced by a 4-by-4 antenna array at 28 GHz. The results of [49–52] show that the FDTD method is a suitable tool for the 5G exposure modelling, however they neglect the expected inter-antenna interference effects resulting from the per-element controlled transmission actually occurring in 5G scenarios.

Several approaches were proposed to determine the time-averaged gain and the Equivalent Isotropic Radiated Power (EIRP) of 5G antenna-array BSs in the far-field region. In [53–55], analytical models of the UE scheduling and spatial distribution in the cell were used to calculate the time-averaged maximum gain and the IERP of a sub-6 GHz 5G BS. In [4], the EIRP calculated from a trial 5G BS deployment data at 3.5 GHz confirmed the theoretical predictions. In [56] the approach of [55] was extended to assess the EIRP (in the far-field region) and the time-averaged power flux density (in the radiating near-field region) of a 8-by-24 element BS at 28 GHz. The EIRP is traditionally used as a proxy to simplify assessment of the SAR in the far-field of a BS, assuming that at a large enough distance from the

BS, the incident EMF is well approximated by a plane wave. However, users in 5G networks, though located in the far-field region of the BS array, do experience near-field-like effects, such as spherical wave-fronts [57], which calls into question the accuracy of the plane-wave exposure approximation.

The uplink exposure in 5G scenarios, i.e., the exposure to the EMF induced by the UE connected to a 5G BS, was addressed extensively in literature. As the distance between the user and the UE is limited by around 1 m in most usage scenarios, it is computationally viable to eclose the complete user-UE system in the FDTD domain. Such FDTD-based studies were conducted for the UE devices operating in 3G [58] and 4G [59] networks. More recently, a study of the uplink 5G exposure to a UE with 4 antenna elements operating at 28 GHz was performed using the FDTD method directly [52]. One challenge of estimating the uplink exposure in 5G is determining the UE duty cycle and average transmit power in realistic scenarios. A numerical approach is described in [60, 61], and in [62], UE transmit power levels were measured in first commercial 5G networks at 3.5 GHz. The uplink component of the 5G exposure is beyond the scope of this dissertation.

1.1.2.1 ATTO-floor

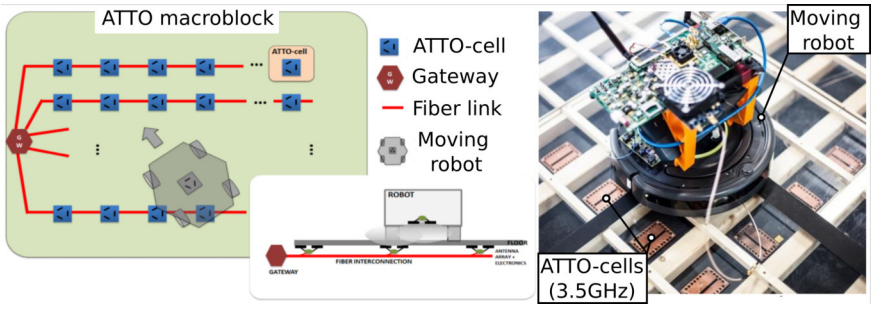

Figure 1.2: Schematic description of the ATTO-floor (left). Picture of the proof-of-concept demonstrator (right). Adapted from [63].

The first 5G technology that will be looked into is the use of ultra-small cells ('ATTO-cells' in Fig. 1.2). Ultra-small cells generally refer to the novel network designs in which the cell size is an order of magnitude smaller than that of a femtocell (less than 10 m^2). Over the recent years several ultra-small cell concepts were proposed [64–66]. In Chapter 2 of this thesis, the human exposure to one such technology, the ATTO-cell floor, first described in [67], is investigated.

The ATTO-floor is a new concept for ultra-high capacity wireless networking, designed to provide connection to autonomous robots (see Fig. 1.2, right), it targets industrial/commercial applications (smart factories in Industry 4.0). The ATTO cells are integrated directly into the floor surface, on which both robots and human

workers move freely. The system concept is designed to provide a very high bitrate (up to 100 Gbps), bitrate density (100 Gbps/m^2), low latency (below 10 μs) and very high service reliability for the UEs moving at speeds lower than 30 m/s [63]. A typical cell size is around 15-by-15 cm^2. The floor-facing antenna of the robot establishes a dedicated connection with the floor-integrated up-facing antenna of the closest cell. The cells are interconnected via the RF-over-fiber passive optical network (shown in red in Fig. 1.2, left). As the robot moves across the floor surface from one ATTO-cell to another, fast handover system assures an uninterrupted connection transceiver integrated into a common ATTO-gateway (red hexagon in Fig. 1.2). The target ATTO-floor realization will operate in the 60 GHz band to deliver the specified performance goals. In this thesis, the EMF exposure of a human to a proof-of-concept version of the ATTO-floor (see Fig. 1.2, right) operating at 3.5 GHz and designed to validate core ATTO principles, will be investigated.

Human workers standing on the ATTO-floor are exposed to radiation in the *near field* of multiple small cells simultaneously. This means that to correctly assess the human exposure in realistic ATTO-cell scenarios, the complete system of human body coupled with multiple ATTO-cells must be considered as a whole. Signals arriving from multiple antennas give rise to the (unintended) constructive interference phenomenon, which boosts local exposure. The effects of this will be investigated in Chapter 2.

1.1.2.2 Massive MIMO

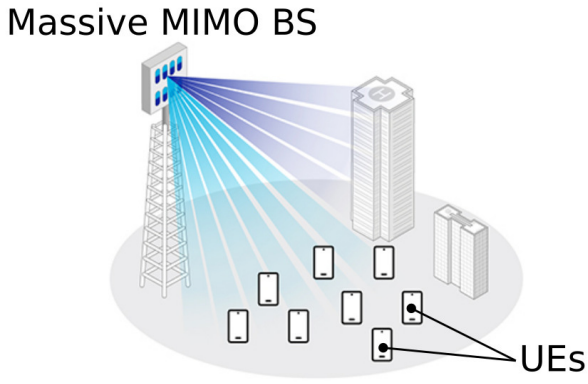

Figure 1.3: An example of an outdoor massive MIMO deployment. Beams in azimuth and elevation are shown. Adapted from [68].

The second studied technology is the use of large arrays with beamforming and massive MIMO precoding capabilities Fig. 1.3. The massive MIMO BS is equipped with a large antenna array that dynamically adjusts its transmission to maximize

the received signal strength of the active users, and, if desired, minimize the interference between them. The codebook-based beamforming [12] is a technique in which, the phases of the BS array elements are selected from a set of predefined configurations to maximize the signal received by the targeted UE. This alters the array radiation patter and forms a high-gain lobe directed to the UE, commonly referred to as a *beam*. If the BS has the real-time channel estimate (e.g., by analyzing part of the uplink traffic from the target UE), the reciprocity-based DL transmission pecoding schemes can be realized. The Equal Gain Transmission (EGT) [69] scheme sets the BS antenna elements' phases to maximize the receiver signal-to-noise (SNR) ratio. The Maximum Ratio Transmission (MRT) [70] also adjusts the elements' amplitudes at a cost of higher hardware complexity, and is known to closely approach the the theoretical maximum SNR when used in large antenna systems. In many practical scenarios, the EGT and MRT schemes produce beams precisely directed towards the target users. However, if the direct beam is obstructed, the BS radiation pattern is dynamically reconfigured to take advantage of the alternative propagation paths, e.g., reflections of and diffractions around the objects surrounding the user. The signals arriving from different directions combine constructively only around the user location, forming a compact region of an elevated EMF - a *hot-spot*.

The BS array can transmit narrow beams in the user direction, or if the direct path is obstructed, produce an EMF hot-spot centered around the user device by utilizing the reflections in the environment. Moreover, the performance of the system is tied to the complexity of the environment and diversity of the signal propagation in it. The user is not coupled to the BS directly, but through the channel state and propagation conditions within the environment. Therefore, predicting the exposure of the massive MIMO technology requires both modelling of the EMF propagation in the environment and the small-scale interaction of the human body with highly focused EMF produced by the BS in this environment. Additionally, if the inter-user interference is minimized by the BS, a significant portion of its power may be transmitted in the directions where no active users are present, elevating the exposure of non-users. The radiation pattern of such BSs is non-stationary, and their time-averaged array gain can be significantly lower than the theoretical maximum [71]. This poses new challenges when determining their *compliance boundary*, i.e. the distance at which the time-average EMF induced by such BSs does not exceed the reference levels of exposure protection.

The methodology of the massive MIMO exposure assessment is developed in Chapters 3 and 4 and applied to study an indoor deployment example. Chapter 5 reaches further into the future by comparing the 5G collocated massive MIMO design to a distributed massive antenna system, in which the antenna elements are evenly spread throughout the environment - a promising 6G candidate. An alternative approach is presented in Chapter 6 that studies an outdoor microcell

scenario in terms of the time-averaged gain produced by the massive MIMO and beamforming BSs. In Chapter 7 experimental data obtained with real massive MIMO hardware is presented to support the so far established numerical predictions.

1.1.3 Contributions

The main original contributions of this dissertation are the following:

- A stochastic method to assess the human exposure to a large number of interfering sources in the near-field was developed and applied to study the exposure of the ATTO-cell technology ([SS1], Chapter 2).
- A method to model the EMF distribution and hot-spots of downlink massive MIMO was developed and applied to study the hot-spots formed in realistic usage scenarios ([SS2], Chapter 3).
- A method to assess realistic downlink human RF-EMF exposure to massive MIMO technology was developed and applied to study the exposure in models of indoor industrial environments ([SS3], Chapters 4 and 5).
- A method to model a realistic time-averaged gain of the large array antennas was developed and applied to study the BSs in outdoor environment models ([SS4], Chapter 6).
- The RT approach for the massive MIMO channel modeling was validated with test-bed measurements ([SS5], Chapter 7).

1.2 Publications

1.2.1 A1 International Journals

(publications in journals listed in the ISI Web of Science)

1.2.1.1 As first author

[SS1] **S. Shikhantsov**, A. Thielens, G. Vermeeren, P. Demeester, L. Martens, G. Torfs, W. Joseph, "STATISTICAL APPROACH FOR HUMAN ELECTROMAGNETIC EXPOSURE ASSESSMENT IN FUTURE WIRELESS ATTO-CELL NETWORKS", *Radiation protection dosimetry*, 2018. (Impact Factor: 0.96, Q3, Rank: 317/350).

[SS2] **S. Shikhantsov**, A. Thielens, G. Vermeeren, E. Tanghe, P. Demeester, L. Martens, G. Torfs, W. Joseph, "Hybrid ray-tracing/FDTD method for human exposure evaluation of a massive MIMO technology in an industrial indoor environment", *IEEE Access*, 2019. (Impact Factor: 3.745, Q1).

[SS3] **S. Shikhantsov**, A. Thielens, G. Vermeeren, P. Demeester, L. Martens, G. Torfs, W. Joseph, "Massive MIMO Propagation Modeling With User-Induced Coupling Effects Using Ray-Tracing and FDTD", *IEEE Journal on Selected Areas in Communications*, 2020. (Impact Factor: 11.42, Q1, Rank: 2/307).

[SS4] **S. Shikhantsov**, A. Thielens, S. Aerts, L. Verloock, G. Torfs, L. Martens, P. Demeester, W. Joseph, "Ray-tracing-based numerical assessment of the spatiotemporal duty cycle of 5G massive MIMO in an outdoor urban environment", *Applied Sciences*, 2020 (Impact Factor: 2.474, Q2).

[SS5] **S. Shikhantsov**, A. Guevara, A. Thielens, G. Vermeeren, P. Demeester, L. Martens, G. Torfs, S. Pollin, W. Joseph, "Spatial Correlation in Indoor Massive MIMO: Measurements and Ray-Tracing", *IEEE Antennas and Wireless Propagation Letters*, 2021 (Impact Factor: 3.726, Q1).

1.2.1.2 As co-author

[SS6] M. Matalatala, M. Deruyck, **S. Shikhantsov**, E. Tanghe, D. Plets, S. Goudos, K. E. Psannis, L. Martens, W. Joseph, "Multi-objective optimization of massive MIMO 5G wireless networks towards power consumption, uplink and downlink exposure", *Applied Sciences*, 2019.

[SS7] M. Velghe, **S. Shikhantsov**, E. Tanghe, L. Martens, W. Joseph, A. Thielens, "Field Enhancement and Size of Radio-Frequency Hotspots Induced by Maximum Ratio Field Combining in Fifth Generation Network", *Radiation Protection Dosimetry*, 2020.

[SS8] M. Matalatala, **S. Shikhantsov**, M. Deruyck, E. Tanghe, D. Plets, S. Goudos, L. Martens, W. Joseph, "Combined Ray-Tracing/FDTD and Network Planner Methods for the Design of Massive MIMO Networks", *IEEE Access*, 2020.

1.2.2 C1 International conferences

1.2.2.1 As first author

[SS9] **S. Shikhantsov**, A. Thielens, G. Vermeeren, P. Demeester, L. Martens, W. Joseph, "Comparison of human EM-exposure in fifth generation wireless technologies: ATTO vs. massive MIMO", *Joint Annual Meeting of the Bioelectromagnetics Society and the European BioElectromagnetics Association (BioEM 2017)*, Hangzhou, China, 5 - 9 June 2017.

[SS10] **S. Shikhantsov**, A. Thielens, G. Vermeeren, P. Demeester, L. Martens, W. Joseph, "Industrial indoor massive MIMO human EM-exposure evaluation", *Joint Annual Meeting of the Bioelectromagnetics Society and the European*

BioElectromagnetics Association (BioEM 2018), Piran, Portorož, Slovenia, 24 - 29 June 2018.

[SS11] **S. Shikhantsov**, A. Thielens, G. Vermeeren, P. Demeester, G. Torfs, L. Martens, W. Joseph, "Hybrid Ray-Tracing/Finite-Difference Time-Domain method for human EMF-exposure assessment of a massive MIMO technology", *Joint Annual Meeting of the Bioelectromagnetics Society and the European BioElectromagnetics Association (BioEM 2019)*, Montpellier, France, 23 - 28 June 2019.

[SS12] **S. Shikhantsov**, A. Thielens, G. Vermeeren, E. Tanghe, P. Demeester, G. Torfs, L. Martens, W. Joseph, "User and non-user EMF-exposure assessment of massive MIMO in an outdoor urban environment using Ray-Tracing method with stochastic geometry", *Joint Annual Meeting of the Bioelectromagnetics Society and the European BioElectromagnetics Association (BioEM 2020)*, Oxford, UK, 21 - 26 June 2020.

[SS13] **S. Shikhantsov**, A. Thielens, G. Vermeeren, E. Tanghe, P. Demeester, G. Torfs, L. Martens, W. Joseph, "Numerical assessment of the spatiotemporal duty cycle of 5G massive MIMO in an outdoor urban environment using radio-frequency Ray-Tracing", *Joint Annual Meeting of the Bioelectromagnetics Society and the European BioElectromagnetics Association (BioEM 2021)*, Ghent, Belgium, 26 September - 1 October 2021.

[SS14] **S. Shikhantsov**, A. Thielens, G. Vermeeren, E. Tanghe, P. Demeester, G. Torfs, L. Martens, W. Joseph, "Collocated and distributed massive MIMO from the human EMF exposure perspective: a comparative study", *Joint Annual Meeting of the Bioelectromagnetics Society and the European BioElectromagnetics Association (BioEM 2021)*, Ghent, Belgium, 26 September - 1 October 2021.

1.2.2.2 As co-author

[SS15] M. Velghe, **S. Shikhantsov**, L. Martens, W. Joseph, A. Thielens, "Assessment of MaMIMO beamwidth using measurements and raytracing", *Future Networks: 5G and beyond (URSI-France 2020 Workshop)*,11 - 13 March 2020, Palaiseau, France.

[SS16] M. Velghe, **S. Shikhantsov**, E. Tanghe, L. Martens, W. Joseph, A. Thielens, "Exposure to RF-EMF hotspots induced by maximum ratio field combining in 5th generation networks", *Joint Annual Meeting of the Bioelectromagnetics Society and the European BioElectromagnetics Association (BioEM 2020)*, Oxford, UK, 21 - 26 June 2020.

[SS17] M. Velghe, **S. Shikhantsov**, L. Martens, W. Joseph, A. Thielens, "Beam width assessment of a Linear Array for MaMIMO applications at 3.5 GHz using measurements and raytracing", *2020 XXXIIIrd General Assembly and Scientific Symposium of the International Union of Radio Science*, 29 August - 5 September 2020, Rome, Italy.

1.2.3 Other

[SS18] **S. Shikhantsov**, A. Thielens, G. Vermeeren, P. Demeester, L. Martens, G. Torfs, W. Joseph, "Numerical assessment of human electromagnetic exposure in ATTO-cell wireless networks", *Workshop Uncertainty Modeling for Engineering Applications (UMEMA 2017)*, 23 – 24 November 2017, Torino, Italy.

[SS19] **S. Shikhantsov**, A. Thielens, G. Vermeeren, E. Tanghe, P. Demeester, L. Martens, G. Torfs, W. Joseph, "Ray-Tracing in stochastic environment models for massive MIMO propagation prediction", *RACON 9th MC meeting and 9th Technical Meeting, "Inclusive Radio Communication Networks for 5G and beyond" (COST Action CA15104)*, 16 – 18 January 2019, Dublin, Ireland.

1.2.4 Awards

[SS20] **BioEM2017 - 1st Place Poster Award**.

References

[1] DH Ring. *Mobile telephony-wide area coverage*. Bell Technical Laboratories technical memoranda, 1947.

[2] Harald Remmert. *2G, 3G, 4G LTE Network Shutdown Updates*.

[3] GSM Association. *2G-3G Sunset Guidelines*.

[4] Davide Colombi, Paramananda Joshi, Bo Xu, Fatemeh Ghasemifard, Vignesh Narasaraju, and Christer Törnevik. *Analysis of the actual power and EMF exposure from base stations in a commercial 5G network*. Applied Sciences, 10(15):5280, 2020.

[5] Arvind Narayanan, Xumiao Zhang, Ruiyang Zhu, Ahmad Hassan, Shuowei Jin, Xiao Zhu, Xiaoxuan Zhang, Denis Rybkin, Zhengxuan Yang, Zhuoqing Morley Mao, et al. *A variegated look at 5G in the wild: performance, power, and QoE implications*. In Proceedings of the 2021 ACM SIGCOMM 2021 Conference, pages 610–625, 2021.

[6] Kaiyue Zeng, Wei Deng, Rui Wang, Long Zhang, Jinxia Cheng, Tao Chen, and Na Yi. *5G Network Performance Evaluation and Deployment Recommendation Under Factory Environment*. In 2021 IEEE 32nd Annual International Symposium on Personal, Indoor and Mobile Radio Communications (PIMRC), pages 1370–1375, 2021.

[7] Simon R. Saunders. *Antennas and Propagation for Wireless Communication Systems*. John Wiley & Sons, Inc., New York, NY, USA, 1st edition, 1999.

[8] V. Nikolopoulos, M. Fiacco, S. Stavrou, and S.R. Saunders. *Narrowband fading analysis of indoor distributed antenna systems*. IEEE Antennas and Wireless Propagation Letters, 2:89–92, 2003.

[9] Hardy Halbauer, Stephan Saur, Johannes Koppenborg, and Cornelis Hoek. *3D beamforming: Performance improvement for cellular networks*. Bell Labs Technical Journal, 18(2):37–56, 2013.

[10] Bjoern Halvarsson, Arne Simonsson, Anders Elgcrona, Ranvir Chana, Paulo Machado, and Henrik Asplund. *5G NR testbed 3.5 GHz coverage results*. In 2018 IEEE 87th Vehicular Technology Conference (VTC Spring), pages 1–5. IEEE, 2018.

[11] Magnus Thurfjell, Arne Simonsson, Oscar Lundberg, and Olle Rosin. *Narrow Beam Channel Characteristics Measured on an 5G NR Grid-of-Beam Test-Bed*. In 2018 IEEE 87th Vehicular Technology Conference (VTC Spring), pages 1–4. IEEE, 2018.

[12] Shanzhi Chen, Shaohui Sun, Guixian Xu, Xin Su, and Yuemin Cai. *Beam-space multiplexing: Practice, theory, and trends, from 4G TD-LTE, 5G, to 6G and beyond*. IEEE Wireless Communications, 27(2):162–172, 2020.

[13] Thomas L Marzetta. *Noncooperative cellular wireless with unlimited numbers of base station antennas*. IEEE Transactions on Wireless Communications, 9(11):3590–3600, 2010.

[14] Emil Björnson, Jakob Hoydis, and Luca Sanguinetti. *Massive MIMO networks: Spectral, energy, and hardware efficiency*. Foundations and Trends in Signal Processing, 11(3-4):154–655, 2017.

[15] Emil Björnson, Erik G Larsson, and Thomas L Marzetta. *Massive MIMO: Ten myths and one critical question*. IEEE Communications Magazine, 54(2):114–123, 2016.

[16] Erik G Larsson, Ove Edfors, Fredrik Tufvesson, and Thomas L Marzetta. *Massive MIMO for next generation wireless systems*. IEEE Communications Magazine, 52(2):186–195, 2014.

[17] Leonard R Kahn. *Ratio squarer*. Proceedings of the Institute of Radio Engineers, 42(11):1704–1704, 1954.

[18] Thomas L Marzetta. *Massive MIMO: an introduction*. Bell Labs Technical Journal, 20:11–22, 2015.

[19] M. Fujimoto, A. Hirata, Jianqing Wang, O. Fujiwara, and T. Shiozawa. *FDTD-derived correlation of maximum temperature increase and peak SAR in child and adult head models due to dipole antenna*. IEEE Transactions on Electromagnetic Compatibility, 48(1):240–247, 2006.

[20] Paolo Bernardi, Marta Cavagnaro, Stefano Pisa, and Emanuele Piuzzi. *Specific absorption rate and temperature elevation in a subject exposed in the far-field of radio-frequency sources operating in the 10-900-MHz range*. IEEE Transactions on biomedical engineering, 50(3):295–304, 2003.

[21] RJ Spiegel, DM Deffenbaugh, and JE Mann. *A thermal model of the human body exposed to an electromagnetic field*. Bioelectromagnetics: Journal of the Bioelectromagnetics Society, The Society for Physical Regulation in Biology and Medicine, The European Bioelectromagnetics Association, 1(3):253–270, 1980.

[22] John A D'Andrea, John M Ziriax, and Eleanor R Adair. *Radio frequency electromagnetic fields: mild hyperthermia and safety standards*. Progress in brain research, 162:107–135, 2007.

[23] International Commission on Non-Ionizing Radiation Protection et al. *ICNIRP Guidelines for Limiting Exposure To Time-Varying Guidelines for Limiting Exposure To Time-Varying Electric, Magnetic and Electromagnetic fields*. Health Phys, 74:494–522, 1998.

[24] International Commission on Non-Ionizing Radiation Protection et al. *Guidelines for limiting exposure to Electromagnetic Fields (100 kHz to 300 GHz)*. Health Physics, 118(5):483–524, 2020.

[25] IEC, 62209-3. *Measurement Procedure for the Assessment of Specific Absorption Rate of Human Exposure to Radio Frequency Fields From Hand-Held and Body-Mounted Wireless Communication Devices—Part 3: Vector Measurement-Based Systems (Frequency Range of 600 MHz to 6 GHz)*.

[26] IEC/IEEE, 62209–1528 ED1. *Measurement Procedure for the Assessment of Specific Absorption Rate of Human Exposure to Radio Frequency Fields From Hand-Held and Body-Worn Wireless Communication Devices—Part 1528: Human Models, Instrumentation and Procedures (Frequency Range of 4 MHz to 10 GHz)*.

[27] Niels Kuster and Quirino Balzano. *Energy absorption mechanism by biological bodies in the near field of dipole antennas above 300 MHz*. IEEE Transactions on vehicular technology, 41(1):17–23, 1992.

[28] Achim Bahr, Sheng-Gen Pan, Thomas Beck, Ralf Kästle, Thomas Schmid, and Niels Kuster. *Comparison between numerical and experimental near-field evaluation of a DCS1800 mobile telephone*. Radio Science, 33(6):1553–1563, 1998.

[29] Justin Cooper, Bernd Marx, Johannes Buhl, and Volker Hombach. *Determination of safety distance limits for a human near a cellular base station antenna, adopting the IEEE standard or ICNIRP guidelines*. Bioelectromagnetics: Journal of the Bioelectromagnetics Society, The Society for Physical Regulation in Biology and Medicine, The European Bioelectromagnetics Association, 23(6):429–443, 2002.

[30] JF Bakker, MM Paulides, E Neufeld, A Christ, Niels Kuster, and GC Van Rhoon. *Children and adults exposed to electromagnetic fields at the ICNIRP reference levels: theoretical assessment of the induced peak temperature increase*. Physics in Medicine & Biology, 56(15):4967, 2011.

[31] T Uusitupa, I Laakso, S Ilvonen, and K Nikoskinen. *SAR variation study from 300 to 5000 MHz for 15 voxel models including different postures*. Physics in Medicine & Biology, 55(4):1157, 2010.

[32] Georg Neubauer, Patrick Preiner, Stefan Cecil, Niki Mitrevski, Johannes Gonter, and Heinrich Garn. *The relation between the specific absorption rate and electromagnetic field intensity for heterogeneous exposure conditions at mobile communications frequencies*. Bioelectromagnetics: Journal of the Bioelectromagnetics Society, The Society for Physical Regulation in Biology and Medicine, The European Bioelectromagnetics Association, 30(8):651–662, 2009.

[33] P Gajsek, TJ Walters, WD Hurt, JM Ziriax, DA Nelson, and Patrick A Mason. *Empirical validation of SAR values predicted by FDTD modeling*. Bioelectromagnetics: Journal of the Bioelectromagnetics Society, The Society for Physical Regulation in Biology and Medicine, The European Bioelectromagnetics Association, 23(1):37–48, 2002.

[34] Stefano Pisa, Marta Cavagnaro, Emanuele Piuzzi, and Vanni Lopresto. *Numerical experimental validation of a GM-FDTD code for the study of cellular phones*. Microwave and Optical Technology Letters, 47(4):396–400, 2005.

[35] T Voigt, H Homann, U Katscher, and O Doessel. *Patient-individual local SAR determination: in vivo measurements and numerical validation*. Magnetic resonance in medicine, 68(4):1117–1126, 2012.

[36] Ilkka Laakso, Tero Uusitupa, and Sami Ilvonen. *Comparison of SAR calculation algorithms for the finite-difference time-domain method*. Physics in Medicine & Biology, 55(15):N421, 2010.

[37] RP Findlay and PJ Dimbylow. *Effects of posture on FDTD calculations of specific absorption rate in a voxel model of the human body*. Physics in Medicine & Biology, 50(16):3825, 2005.

[38] Ilkka Laakso. *Assessment of the computational uncertainty of temperature rise and SAR in the eyes and brain under far-field exposure from 1 to 10 GHz*. Physics in Medicine & Biology, 54(11):3393, 2009.

[39] Ezequiel I. Espinosa R and Roberto Linares y M. *Analysis of SAR distribution in a heterogeneous and homogenous head model at 2.4 GH z using the FDTD method*. Microwave and Optical Technology Letters, 60(6):1323–1331, 2018.

[40] Jianqing Wang, N. Mukaide, and O. Fujiwara. *FDTD calculation of organ resonance characteristics in an anatomically based human model for plane-wave exposure*. In Asia-Pacific Conference on Environmental Electromagnetics, 2003. CEEM 2003. Proceedings., pages 126–129, 2003.

[41] JW Hand. *Modelling the interaction of electromagnetic fields (10 MHz–10 GHz) with the human body: methods and applications*. Physics in Medicine & Biology, 53(16):R243, 2008.

[42] Akimasa Hirata, Yinliang Diao, Teruo Onishi, Kensuke Sasaki, Seungyoung Ahn, Davide Colombi, Valerio De Santis, Ilkka Laakso, Luca Giaccone, Wout Joseph, Essam A. Rashed, Wolfgang Kainz, and Ji Chen. *Assessment of Human Exposure to Electromagnetic Fields: Review and Future Directions*. IEEE Transactions on Electromagnetic Compatibility, 63(5):1619–1630, 2021.

[43] L. Catarinucci, P. Palazzari, and L. Tarricone. *Human exposure to the near field of radiobase antennas - a full-wave solution using parallel FDTD*. IEEE Transactions on Microwave Theory and Techniques, 51(3):935–940, 2003.

[44] M Martínez-Búrdalo, A Martin, A Sanchis, and R Villar. *FDTD assessment of human exposure to electromagnetic fields from WiFi and bluetooth devices in some operating situations*. Bioelectromagnetics: Journal of the Bioelectromagnetics Society, The Society for Physical Regulation in Biology and Medicine, The European Bioelectromagnetics Association, 30(2):142–151, 2009.

[45] Yenny Pinto and Joe Wiart. *Statistical analysis and surrogate modeling of indoor exposure induced from a WLAN source*. In 2017 11th European Conference on Antennas and Propagation (EUCAP), pages 806–810, 2017.

[46] Emma Chiaramello, Marta Parazzini, Serena Fiocchi, Paolo Ravazzani, and Joe Wiart. *Stochastic Dosimetry Based on Low Rank Tensor Approximations for the Assessment of Children Exposure to WLAN Source*. IEEE Journal of Electromagnetics, RF and Microwaves in Medicine and Biology, 2(2):131–137, 2018.

[47] Marie-Christine Gosselin, Günter Vermeeren, Sven Kuhn, Valpré Kellerman, Stefan Benkler, Tero M. I. Uusitupa, Wout Joseph, Azeddine Gati, Joe Wiart, Frans J. C. Meyer, Luc Martens, Toshio Nojima, Takashi Hikage, Quirino Balzano, Andreas Christ, and Niels Kuster. *Estimation Formulas for the Specific Absorption Rate in Humans Exposed to Base-Station Antennas*. IEEE Transactions on Electromagnetic Compatibility, 53(4):909–922, 2011.

[48] Ilaria Liorni, Myles Capstick, Luuk Van Wel, Joe Wiart, Wout Joseph, Elisabeth Cardis, Mònica Guxens, Roel Vermeulen, and Arno Thielens. *Evaluation of specific absorption rate in the far-field, near-to-far field and near-field regions for integrative radiofrequency exposure assessment*. Radiation Protection Dosimetry, 190(4):459–472, 2020.

[49] Marta Bonato, Laura Dossi, Emma Chiaramello, Serena Fiocchi, Silvia Gallucci, Gabriella Tognola, Paolo Ravazzani, and Marta Parazzini. *Human RF-EMF Exposure Assessment Due to Access Point in Incoming 5G Indoor Scenario*. IEEE Journal of Electromagnetics, RF and Microwaves in Medicine and Biology, 5(3):269–276, 2021.

[50] Congsheng Li, Chunying Xu, Ruixin Wang, Lei Yang, and Tongning Wu. *Numerical evaluation of human exposure to 3.5-GHz electromagnetic field by considering the 3GPP-like channel features*. Annals of Telecommunications, 74(1):25–33, 2019.

[51] Yinliang Diao and Akimasa Hirata. *Exposure Assessment of Array Antennas at 28 GHz Using Hybrid Spherical Near-Field Transformation and FDTD Method*. IEEE Transactions on Electromagnetic Compatibility, 63(5):1690–1698, 2021.

[52] Maria Sole Morelli, Silvia Gallucci, Beatrice Siervo, and Valentina Hartwig. *Numerical analysis of electromagnetic field exposure from 5G mobile communications at 28 GHZ in adults and children users for real-world exposure scenarios*. International Journal of Environmental Research and Public Health, 18(3):1073, 2021.

[53] Björn Thors, Anders Furuskär, Davide Colombi, and Christer Törnevik. *Time-averaged realistic maximum power levels for the assessment of radio frequency exposure for 5G radio base stations using massive MIMO*. IEEE Access, 5:19, 2017.

[54] Paolo Baracca, Andreas Weber, Thorsten Wild, and Christophe Grangeat. *A Statistical Approach for RF Exposure Compliance Boundary Assessment in Massive MIMO Systems*. In WSA 2018; 22nd International ITG Workshop on Smart Antennas, pages 1–6. VDE, 2018.

[55] Bo Xu, Davide Colombi, Christer Törnevik, Fatemeh Ghasemifard, and Jiajia Chen. *On Actual Maximum Exposure From 5G Multi-Column Radio Base Station Antennas*. 2020.

[56] Bo Xu, David Anguiano Sanjurjo, Davide Colombi, and Christer Törnevik. *A Monte Carlo Analysis of Actual Maximum Exposure From a 5G Millimeter-Wave Base Station Antenna for EMF Compliance Assessments*. Frontiers in Public Health, 9, 2021.

[57] Xiang Gao, Jose Flordelis, Ghassan Dahman, Fredrik Tufvesson, and Ove Edfors. *Massive MIMO channel modeling-extension of the COST 2100 model*. In Joint NEWCOM/COST Workshop on Wireless Communications (JNCW), 2015.

[58] Emma Chiaramello, Marta Bonato, Serena Fiocchi, Gabriella Tognola, Marta Parazzini, Paolo Ravazzani, and Joe Wiart. *Radio frequency electromagnetic fields exposure assessment in indoor environments: a review*. International journal of environmental research and public health, 16(6):955, 2019.

[59] Emma Chiaramello, Marta Parazzini, Serena Fiocchi, Paolo Ravazzani, and Joe Wiart. *Assessment of Fetal Exposure to 4G LTE Tablet in Realistic Scenarios: Effect of Position, Gestational Age, and Frequency*. IEEE Journal of Electromagnetics, RF and Microwaves in Medicine and Biology, 1(1):26–33, 2017.

[60] Sven Kuehn, Serge Pfeifer, Beyhan Kochali, Niels Kuster, and C Bern. *Modelling of total exposure in hypothetical 5G mobile networks for varied topologies and user scenarios*. Final Report of Project CRR, 816, 2019.

[61] Seungmo Kim and Imtiaz Nasim. *Human Electromagnetic Field Exposure in 5G at 28 GHz*. IEEE Consumer Electronics Magazine, 9(6):41–48, 2020.

[62] Marius Nedelcu, Victor Niţu, and Teodor Petrescu. *Uplink power levels of user equipment in commercial 4G and 5G networks*. In 2021 13th International Conference on Electronics, Computers and Artificial Intelligence (ECAI), pages 1–4, 2021.

[63] Guy Torfs, Haolin Li, Sam Agneessens, Johan Bauwelinck, Laurens Breyne, Olivier Caytan, Wout Joseph, Sam Lemey, Hendrik Rogier, Arno Thielens, Dries Vande Ginste, Joris Van Kerrebrouck, Günter Vermeeren, Xin Yin, and Piet Demeester. *ATTO: Wireless Networking at Fiber Speed*. IEEE Journal of Lightwave Technology, 2017.

[64] Osama Zwaid Alsulami, Mohamed OI Musa, Mohammed T Alresheedi, and Jaafar MH Elmirghani. *Co-existence of micro, pico and atto cells in optical wireless communication*. In 2019 IEEE Conference on Standards for Communications and Networking (CSCN), pages 1–5. IEEE, 2019.

[65] Stefano Pergoloni, Mauro Biagi, Stefania Colonnese, Roberto Cusani, and Gaetano Scarano. *Coverage optimization of 5G atto-cells for visible light communications access*. In 2015 IEEE International Workshop on Measurements & Networking (M&N), pages 1–5. IEEE, 2015.

[66] Ha-Vu Tran, Georges Kaddoum, Panagiotis D Diamantoulakis, Chadi Abou-Rjeily, and George K Karagiannidis. *Ultra-small cell networks with collaborative RF and lightwave power transfer*. IEEE Transactions on Communications, 67(9):6243–6255, 2019.

[67] Bart Lannoo, Abhishek Dixit, Didier Colle, Johan Bauwelinck, Bart Dhoedt, Bart Jooris, Ingrid Moerman, Mario Pickavet, Hendrik Rogier, Pieter Simoens, et al. *Radio-over-fibre for ultra-small 5G cells*. In Transparent Optical Networks (ICTON), 2015 17th International Conference on, pages 1–4. IEEE, 2015.

[68] Samsung. *Massive MIMO for New Radio*. Technical report, Samsung Electronics Co., Ltd., 2020.

[69] D. J. Love and R. W. Heath. *Equal gain transmission in multiple-input multiple-output wireless systems*. IEEE Transactions on Communications, 51(7):1102–1110, July 2003.

[70] Thomas L. Marzetta, Erik G. Larsson, Hong Yang, and Hien Quoc Ngo. *Fundamentals of massive MIMO*. Cambridge University Press, 2016.

[71] Elif Degirmenci, Björn Thors, and Christer Törnevik. *Assessment of compliance with RF EMF exposure limits: Approximate methods for radio base station products utilizing array antennas with beam-forming capabilities*. IEEE Transactions on Electromagnetic Compatibility, 58(4):1110–1117, 2016.

Part I

ATTO-cell technology

2

Exposure to the ATTO-cell Technology

2.1 Introduction

In this chapter we are looking at the first technology introduced in chapter 1 - ATTO-floor. From the human exposure perspective, the main distinctive feature of this technology is that the human body is located in the near field at least of some ATTO-cells. As shown schematically in Fig. 1.2 (left), ATTO-cells are integrated into the floor and cover its entire area. According to the current design [1], operating at a center frequency of 3.5 GHz, (Fig. 2.2 in this section) an ATTO-cell has dimensions of 15 cm-by-15 cm, and an antenna is supplied with a maximum power of 1 mW. Possible applications of the ATTO technology include industrial warehouses or factories of the future, where multitudes of mobile robots and human workers operate simultaneously. Robots, being equipped with an antenna featuring downward-pointing pattern, are the target users, see Fig. 1.2 (right). Due to the provisioned fast handover system, at any time instance a robot is only connected to the antenna right underneath it. Thus it is unlikely for humans to be exposed by the ATTO-floor directly. In other words, most of the time humans will be exposed to the scattered fields of antennas serving surrounding robots.

Exposure from a *single* ATTO-cell at 3.5 GHz was studied both numerically and experimentally in [2, 3]. Peak spatial specific absorption rate averaged over a 10 g cube ($\mathrm{psSAR}_{10\mathrm{g}}$) was found to be lower than 2.8 mW/kg, which is far below the International Commission on Non-Ionizing Radiation Protection (ICNIRP) guidelines for the general public in limbs (4 W/kg). Though the power radiated

by the ATTO-cell is not enough to violate the ICNIRP guidelines, the ATTO-floor network represents a valuable study-case of exposure to phased antenna-arrays. Moreover, appropriately scaled obtained exposure levels remain valid for an arbitrary antenna radiated power.

In this chapter, we address, for the first time, the worst-case exposure scenario for an ATTO-*floor network*: a human standing on the entire ATTO-floor network with all antennas radiating simultaneously and constantly. To assert the highest exposure we need to account for the fields induced by the antennas in proximity of the studied subject. As it will be shown further, the number of antennas that give significant contribution to the total exposure is sufficiently small. Another novel contribution presented in this chapter is the development of a statistical approach for exposure estimation in a system with multiple interfering nodes. By applying this approach, we evaluate the psSAR_{10g} that could hypothetically be produced by ATTO networks under very conservative assumptions.

In a multi-antenna system the powers and the relative phases with which the antennas are supplied define the resulting EMF distribution [4, 5]. This affects the power dissipated in the regions occupied by human body tissues. To find such a combination of powers and phases that yields the highest exposure means finding the *worst-case* exposure in a given scenario. A method that addresses this problem in the case of the exposure to multi-coil MRI-scanners is known [6, 7]. It can be shown that, if the total power shared by all the antennas is limited, then the problem is equivalent to finding the largest eigenvalue of a matrix. However, if the maximum power is limited *per antenna*, a general optimization method is needed [8]. In the following sections we propose a statistical approach that not only allows to find the worst-case, but also gives an estimate of the average exposure and field distribution over the ATTO-floor.

2.2 Materials and Methods

In the first part of this section the numerical setup is presented. In the second part we give an overview of the conducted simulations. The third part describes the post-processing methods and explains the method of exposure assessment.

2.2.1 Numerical setup

For electromagnetic simulations we use the Finite-Difference Time-Domain (FDTD) method implemented in Sim4Life v3.2 (ZMT, Zürich, Switzerland). The simulation domain is depicted in Figure 2.2. We use the Virtual Population v.3.1 posable heterogeneous Duke phantom [9], which represents an average adult male human (height = 1.77 m, mass = 70.2 kg, BMI = 22.4 kg/m^2). Its feet are rotated by 10° in the sagittal plane to be parallel to the floor, as it usually is in a normal

standing posture. The shortest distance between the feet and the surface of the floor is 10 mm, which is aimed at representing the height of a shoe sole. The floor surface is a sheet of 6 mm Acrylic glass ($\sigma = 2.5 \cdot 10^{-3}$ S/m, $\varepsilon_r = 2.6$). Each ATTO-cell is equipped with a single linearly polarized planar, substrate-integrated-waveguide cavity-backed slot antenna, constructed from of foam material substrate and copper plated nylon conducting elements. A model of the antenna used in simulations further in this chapter is shown in Fig. 2.1 together with its normalized radiation pattern. The antenna dimensions are 55 mm and 80 mm along x and y, respectively. A 4-by-4 array of equidistantly separated antennas is placed on a plastic ($\sigma = 5 \cdot 10^{-4}$ S/m, $\varepsilon_r = 2.25$) substrate 58 mm below the floor to form 16 ATTO-cells. The sensitivity of the exposure values to the antenna array size is studied quantitatively in the next section and the choice of 4-by-4 array is justified.

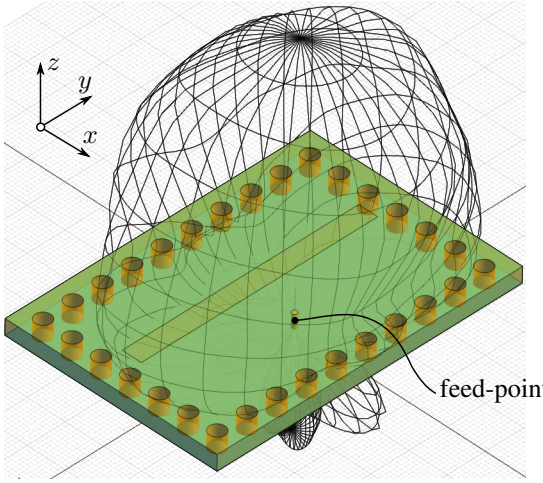

Figure 2.1: ATTO-floor patch-antenna. The radiation pattern is shown with black grid-lines and the feed-point location is indicated. The depicted coordinate system is used through the rest of the chapter.

In order to optimize computational resources, only the legs of the phantom are included into the simulation domain. This change has a negligible effect on the field distribution inside the phantom due to its fast decrease in amplitude with distance from the floor (more than 50 dB at 1 m height, see [2]). The domain boundary box dimensions are set to be 750 mm-by-750 mm-by-1200 mm and absorbing boundary conditions with the Perfectly Matched Layer (PML) are applied. With the maximum of 1.2 mm discretization resolution in lossy regions, it resulted in approximately 150 million voxels in total.

In the given setup, the phantom penetrates the *near-field* region of at least some of the antennas in the array ($2L^2/\lambda \approx 220$ mm, where $L \approx 100$ mm is the largest

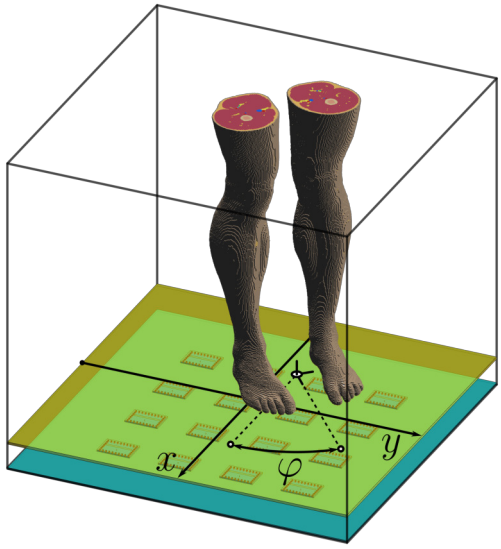

Figure 2.2: Simulation domain. 16 patch-antennas and voxeled part of the phantom included into the domain are shown. x and y are Cartesian coordinates the phantom's pivot point in horizontal plane and angle φ defines the phantom's rotation normal to the plane. Black wireframe box shows the boundaries of the domain.

antenna dimension, and $\lambda \approx 86$ mm is the wavelength at 3.5 GHz). Therefore, the exposure is highly affected by its location with respect to the array. To study this effect we allow the phantom translation in the horizontal plane (parallel to the floor) and rotation around an axis orthogonal to the floor. Such transformation can be defined by three scalar parameters: two Cartesian coordinates x, y and the angle of rotation φ. Any fixed set of $\{x, y, \varphi\}$ we will further refer to as *configuration*, see Figure 2.2. Exposure variation due to the phantom's movement in the direction perpendicular to the floor was covered in [2], and is not considered in the current study.

2.2.2 Simulations

We assume that all positions and orientations of a human on the floor have equal probability. Utilizing the periodical structure of the antenna array, we restrict translations of the phantom to a central rectangle of size 150-by-150 mm, which is the size of one ATTO-cell. The rectangle is covered with a 7-by-7 rectangular grid of nodes which are equidistantly separated, see Figure 2.3. Taking into account reflec-

tion symmetries of individual patch antennas relative to x and y axis and matching symmetries of the antenna array structure, for each node of this translational grid we consider three angles of phantom's rotation: 0°, 45°, and 90°. In total, we obtain 147 configurations in which the phantom is translated to one of the nodes on the grid and rotated to one of the angles.

For every configuration we perform a multi-port FDTD simulation, which consists of 16 single-port simulations. In each of them only a single antenna is excited with a 3.5 GHz sinusoidal signal of normalized input power. After the simulation reaches a stationary state, electric fields in a subregion that encloses only the phantom's feet are saved for post-processing.

2.2.3 Post-processing

The post-processing is done in several steps.

First, we assume that antennas driven with maximum power lead to the highest exposure. This allows to normalize the field distributions obtained from simulations to the radiated power of 1 mW.

Second, we independently sample 16 numbers from a uniform random distribution in $[0, 2\pi)$. These are set as phases for antennas in a multi-port simulation. By doing so we assume that the phases of antenna signals are uncorrelated.

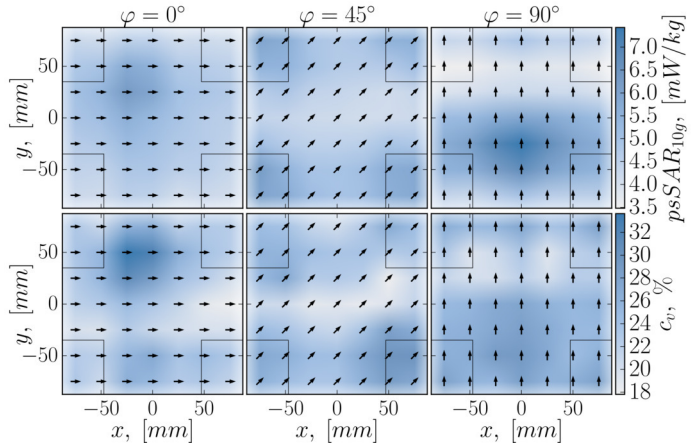

Figure 2.3: Average value (top) and relative standard deviation c_v (bottom) of exposure samples distribution for all configurations. Arrows denote the rotation of the phantom. The outlines of the antennas are shown with thin black lines. The color-bars on the right show psSAR_{10g} in mW/kg (top) and its relative standard deviation c_v in % (bottom).

Third, we calculate a field distribution inside the domain with amplitudes and phases of all 16 antennas set. Using standardized numerical routines (IEC/IEEE

P62704-1) we obtain a psSAR_{10g} value, which is further referred to as an *exposure sample*.

Fourth, we generate 10^3 exposure samples for each configuration. This yields $147 \cdot 10^3$ exposure samples in total, which cover variations of phantom positions on the floor and antennas relative phases. This sample set allows to estimate the statistical properties of exposure in the given EM-environment.

The procedure of exposure samples generation can also be viewed as a Monte-Carlo random point method for finding a global minimum of a function. The numerical error of this method decreases with the number of samples N as $1/\sqrt{N}$ [10]. To further decrease the numerical error, we use phases of the highest exposure sample as a starting point for an optimization. The complete numerical procedure is integrated into the Sim4Life scripting environment, which allows to utilize its internal algorithms for psSAR_{10g} evaluation at every iteration. The resulting solution is deemed to approach closely the upper bound of the psSAR_{10g} in a given configuration.

Finally, we examine the effect of human body morphology on peak SAR in the worst-case configuration. For this, we perform additional FDTD simulations with three heterogeneous Virtual Family V1.0 phantoms [11], Ella, an adult woman, Billie, an 11-year-old girl and Thelonious, a 6-year-old boy. Each of these phantoms is simulated in the configuration, in which the worst-case exposure is found for the Duke phantom (adult male). Using this configuration aims at providing an approximation for the worst-case exposure avoiding a computationally expensive process of determining it more accurately, as it has been done previously for Duke. Each phantom's feet are rotated to be parallel to the ground and the simulation domain dimensions are preserved. Such approach allows detecting phantom-related factors influencing the exposure (e.g., size of the feet), the magnitude of which is greater than the variation of the exposure across the ATTO-floor.

2.3 Results

2.3.1 Spatial distributions of psSAR_{10g}

Figure 2.3 shows spatial distribution of exposure for the simulated configurations. The color of a square corresponds to the mean value (top row) and relative standard deviation c_v expressed in % (bottom row) of 1000 exposure samples. Its coordinates in the xy-plane match the coordinates of the phantom's pivot point in a configuration. Columns represent the angle of the phantom's rotation. These exposure maps give a high-level summary of exposure variation inside the ATTO-cell.

In general, the highest mean psSAR_{10g} is observed when the toes of one of the feet are placed directly above the feed-point of an antenna, e.g., $\{0, -25 \text{ mm}, 90°\}$, see Figure 2.3. Higher maximum mean values are observed when the feet are

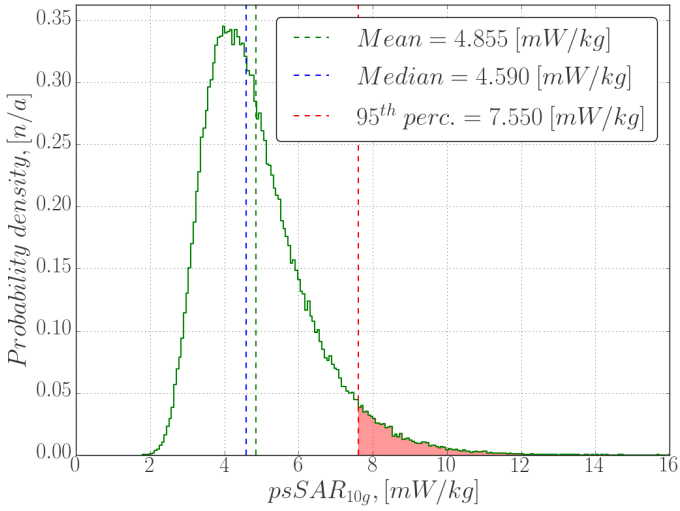

Figure 2.4: Histogram of all generated exposure samples pooled together. Emitted power per antenna is 1 mW and 16 mW in total. Mean and median of the distribution are shown in dashed blue and green lines respectively and values exceeding the 95$^{\text{th}}$ percentile are shown in red.

perpendicular to the polarization direction of the antennas (90°), whereas their parallel mutual placement (0°) results in lower mean psSAR$_{10g}$ values, which are more evenly distributed over the xy plane. One possible reason for that is the occurrence of a resonance in the toes in the former case [12].

To obtain general characteristics of the ATTO-floor exposure, all samples from all configurations are plotted as a histogram in Figure 2.4. It is a bell-shaped skewed distribution. Its nonparametric skew, defined as $S = (\mu - \nu)/\sigma$, where μ - its arithmetic mean, ν - median and σ - standard deviation, equals approximately 0.19. Its arithmetic mean can be interpreted as an average exposure of ATTO-floor and equals 4.9 mW/kg. This is almost twice the upper limit found in [2] for a *single* ATTO-cell but still three orders of magnitude lower than ICNIRP general public guidelines (4 W/kg). The 95$^{\text{th}}$ percentile, indicating the level of exposure that is exceeded with a 5% chance, equals around 7.6 mW/kg.

2.3.2 Worst case ATTO-floor exposure

To establish the upper bound on the exposure of the ATTO-floor we perform an optimization procedure. We use the configuration yielding the highest sample mean psSAR$_{10g}$ (7.4 mW/kg) and, at the same time, contains a sample with highest exposure value (14.9 mW/kg). This configuration is defined by the set $\{0$ mm, -25 mm, $90°\}$. In this case, the toes of the phantom are located directly

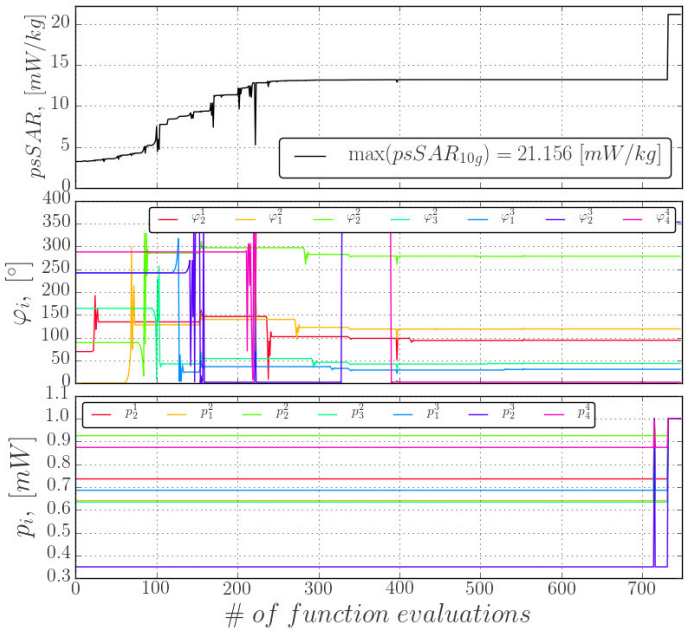

(a) The evolution of optimization procedure with coupled modified Hybrid Powell and L-BFGS-B methods implemented in SciPy Python library. Changes of psSAR_{10g} are shown (top) along with the relative phases of selected antennas (middle) and their powers (bottom).

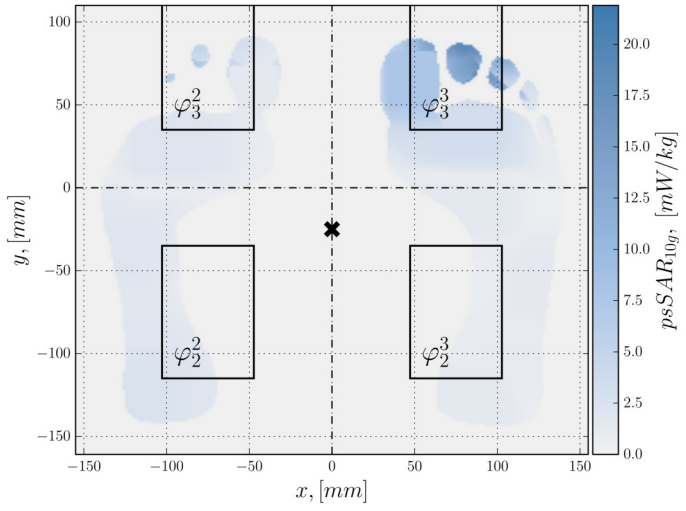

(b) Top view of the worst-case SAR_{10g} distribution in the horizontal slice coincident with the peak location. Antenna outlines are shown as black rectangles with their indices indicated at the lower left corner. A black cross depicts the phantom's pivot point.

Figure 2.5: The worst case exposure search procedure.

above two central antenna tiles. Phases and powers of all 16 antennas act as minimization parameters of the objective function $-\log(\text{psSAR}_{10g})$, therefore maximizing psSAR_{10g}. Two optimization algorithms are coupled: first phases are optimized using Hybrid Powell method [13], then powers of antennas bounded between 0 and 1 mW are optimized with the L-BFGS-B algorithm [14]. The procedure is performed 100 times; each time the parameters to initialize the optimization are independently sampled from the uniform random distribution: in $[0, 2\pi]$ for phases (in radians) and in $[0, 1]$ for powers (in mW). An example of the evolution of a successful optimization procedure is depicted in Figure 2.5a.

The antennas are numbered using two indices: the lower index indicates antenna number along the y-axis, the upper index indicates antenna number along the x-axis. Phase φ_3^3 has the highest impact on the psSAR_{10g}, with corresponding antenna being located directly under the peak-SAR cube (see Figure 2.5b). Phase φ_3^3 is set as a reference and phases of antennas relative to it are computed as $\varphi_i^j = \tilde{\varphi}_i^j - \varphi_3^3$, where $\tilde{\varphi}_i^j$ are absolute phases. Phases of antennas that have a significant impact on the exposure are shown at the bottom of the Figure 2.5a. Antennas from four central tiles ($\varphi_3^2,\ \varphi_2^3,\ \varphi_2^2$) tend to have higher impact on psSAR_{10g} than those from periphery.

In all optimization runs, the antenna powers converged to their upper bound (1 mW). In fact, the optimal antenna phases guarantees, that all the antennas signals interfere constructively in the region of interest (peak-10g-cube). Therefore, increasing the antenna powers necessarily leads to the increase of exposure.

After approximately 1000 function evaluations the optimization terminates, reaching a flat plateau (see Figure 2.5a). The resulting exposure value is considered to be the worst-case exposure in the worst-case scenario and equals to around 21.2 mW/kg. This value is almost 50% higher than the value of the highest exposure sample observed previously and more than four times the average exposure of the ATTO-floor. It places an upper bound on the exposure of the 4-by-4 ATTO-cell array. It is worth pointing out that the established upper bound constitutes only slightly over 0.5% of the ICNIRP basic restrictions for general public (4 W/kg), and around 0.1% - for workers (20 W/kg). In other words, the output power of an ATTO-cell of up to around 1 W would still satisfy the ICNIRP guidelines for workers. To put this into perspective, an average psSAR_{10g} of a generic mobile phone induced in the head at 1900 MHz is around 5 W/kg for the total output power of 1 W [15]. This is nearly the same as the average psSAR_{10g} found for the ATTO-floor with 1 W radiated *per antenna*.

Figure 2.5b depicts the worst-case psSAR_{10g} distribution in a 2D slice, coincident with the highest exposure voxel. The voxel is located at the very edge of the right foot toe. The 10 gram cube assigned to it has the volume of nearly 48 cm^3 and only one fifth of it is occupied with a lossy media.

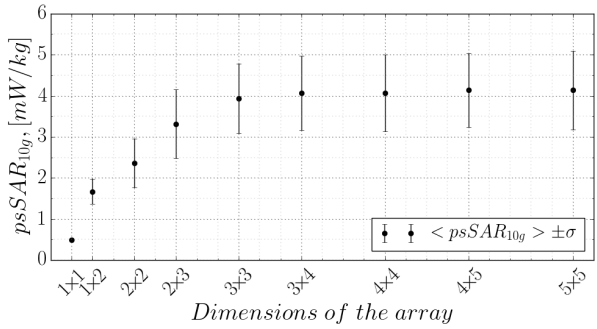

Figure 2.6: Parameters of exposure samples distributions as a function of antenna array size. Each point and error-bar represents mean value and standard deviation of exposure samples distribution.

2.3.3 Array size impact

In addition, influence of the array size on the total exposure is studied. The setup of Figure 2.2 is used with the antenna array extended to 5-by-5 size. The phantom position is fixed at the center of the floor with 0° rotation. After a single multi-port simulation is done, nine post-processing runs are performed and the results are shown in Figure 2.6. The horizontal axis indicates the size of a rectangular sub-array that is excited, gradually expanding from the central tile to the full 5-by-5 floor. Position of points and error-bars along the vertical axis indicates the average and standard deviation of 1000 random exposure samples respectively.

The rate at which exposure grows decreases drastically after the array size becomes larger than 3-by-3 tiles. Relative exposure increase of 5-by-5 compared to 3-by-3 array is only around 2.5%. Such a small relative change of exposure justifies the use of 4-by-4 array setup with phantom movements, as in any configuration the phantom is kept enclosed inside one of four 3-by-3 sub-arrays of the initial array. At the same time, a 2-by-2 array, though covering the phantom's footprint, is not sufficient for exposure estimation.

2.3.4 Influence of body morphology

Finally, the effect of body morphology is investigated. Three additional simulations with different phantoms are done: Thelonious (a 6-year-old boy), Ella (an adult woman) and Billie (an 11-year-old girl). All phantoms are simulated in a worst-case configuration found for Duke (Fig. 2.5b). Figure 2.7 depicts the parameters of distribution for 1000 random exposure samples, generated for each phantom (including Duke). The average exposure for Thelonious, Ella and Billie phantoms is approximately 5.2 mW/kg, which is nearly equal to the average exposure over the whole ATTO-floor, found for Duke (4.9 mW/kg). In addition no significant

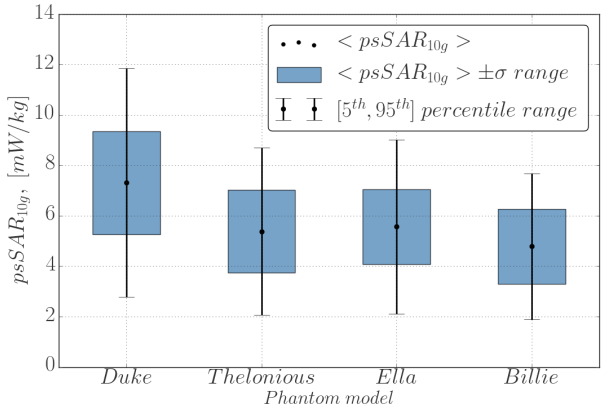

Figure 2.7: Bar-plot of psSAR$_{10g}$ for Duke v.3.1, Thelonious v.1.0, Ella v.1.0 and Billie v.1.0 phantom models, evaluated in the worst-case configuration. Solid dots indicate mean psSAR$_{10g}$, blue bars and caped solid lines cover $\langle$psSAR$_{10g}\rangle\pm\sigma$ band and range from 5th to 95th percentile respectively.

variation of exposure mean among three newly simulated phantoms is present; their relative differences are 2%, 6% and 9% for Thelonious, Ella and Billie phantoms, respectively. At the same time the average exposure for Duke in the identical configuration (7.4 mW/kg) is nearly 30% higher. These observations suggest that the worst-case configuration found for Duke does not guarantee the worst-case for other phantom models, i.e. worst-case configuration is model-specific and possible effects of body morphology (e.g. the size of the feet) are suppressed by exposure alteration due to phantom positioning.

2.4 Conclusions

In this chapter, the exposure of the ultra-small cell ATTO-floor technology in terms of peak spatial psSAR$_{10g}$ was studied. We showed the significance of the effect that a multi-antenna interference has on the psSAR$_{10g}$ value and used a statistical approach to obtain the average exposure level of 4.9 mW/kg and a 95th value of 7.6 mW/kg on the ATTO-floor as well as draw a theoretical maximum for 4-by-4 floor (21.9 mW/kg). Peaks of SAR were found to occur always in feet, being well below the corresponding ICNIRP guidelines for the general public, with input power of 1 mW per one ATTO-floor node. The relation between the ATTO-floor size and psSAR$_{10g}$ it induces was established. It was shown that due to a fast decay of the EMF radiated by the ATTO-floor nodes in the lateral direction, a only a limited number of the nodes (4-by-4 sub-array) induced the largest portion of the phantom's exposure. Finally, the effect of body morphology was investigated,

showing moderate variation of the average exposure that the ATTO-floor induces in phantoms of different gender and age.

In Part II we are going to turn our focus to the exposure of humans in the far field of large antenna arrays. As we will see, the radiation from every element of such array contributes significantly to the total exposure of a phantom. Additionally, a propagation prediction model will be needed to correctly estimate the incident EMF properties in proximity of the user.

References

[1] Guy Torfs, Haolin Li, Sam Agneessens, Johan Bauwelinck, Laurens Breyne, Olivier Caytan, Wout Joseph, Sam Lemey, Hendrik Rogier, Arno Thielens, Dries Vande Ginste, Joris Van Kerrebrouck, Günter Vermeeren, Xin Yin, and Piet Demeester. *ATTO: Wireless Networking at Fiber Speed*. IEEE Journal of Lightwave Technology, 2017.

[2] Arno Thielens, Günter Vermeeren, Olivier Caytan, Guy Torfs, Piet Demeester, Johan Bauwelinck, Hendrik Rogier, Luc Martens, and Wout Joseph. *Radiofrequency exposure near an attocell as part of an ultra-high density access network*. Bioelectromagnetics, 38(4):295–306, 2017.

[3] Günter Vermeeren, Guy Torfs, Arno Thielens, H Regier, Piet Demeester, Luc Martens, and Wout Joseph. *Signal-to-interference ratio between atto cells in an ultra-high density wireless access network*. In 2017 IEEE-APS Topical Conference on Antennas and Propagation in Wireless Communications (APWC), pages 270–273. IEEE, 2017.

[4] Björn Thors, Arno Thielens, Jonas Fridén, Davide Colombi, Christer Törnevik, Günter Vermeeren, Luc Martens, and Wout Joseph. *Radio frequency electromagnetic field compliance assessment of multi-band and MIMO equipped radio base stations*. Bioelectromagnetics, 35(4):296–308, 2014.

[5] Elif Degirmenci, Björn Thors, and Christer Törnevik. *Assessment of compliance with RF EMF exposure limits: Approximate methods for radio base station products utilizing array antennas with beam-forming capabilities*. IEEE Transactions on Electromagnetic Compatibility, 58(4):1110–1117, 2016.

[6] Torsten Köhler, Peter Maass, Peter Wust, and Martin Seebass. *A fast algorithm to find optimal controls of multiantenna applicators in regional hyperthermia*. Physics in medicine and biology, 46(9):2503, 2001.

[7] DO Brunner, J Paska, J Froehlich, and KP Pruessmann. *SAR assessment of transmit arrays: deterministic calculation of worst-and best-case performance*. Quadrature, 30:40, 2009.

[8] Esra Neufeld, Marie-Christine Gosselin, Manuel Murbach, Andreas Christ, Eugenia Cabot, and Niels Kuster. *Analysis of the local worst-case SAR exposure caused by an MRI multi-transmit body coil in anatomical models of the human body*. Physics in medicine and biology, 56(15):4649, 2011.

[9] Marie-Christine Gosselin, Esra Neufeld, Heidi Moser, Eveline Huber, Silvia Farcito, Livia Gerber, Maria Jedensjö, Isabel Hilber, Fabienne Di Gennaro, Bryn Lloyd, et al. *Development of a new generation of high-resolution*

anatomical models for medical device evaluation: the Virtual Population 3.0. Physics in medicine and biology, 59(18):5287, 2014.

[10] Russel E Caflisch. *Monte carlo and quasi-monte carlo methods*. Acta numerica, 7:1–49, 1998.

[11] Andreas Christ, Wolfgang Kainz, Eckhart G Hahn, Katharina Honegger, Marcel Zefferer, Esra Neufeld, Wolfgang Rascher, Rolf Janka, Werner Bautz, Ji Chen, et al. *The Virtual Family—development of surface-based anatomical models of two adults and two children for dosimetric simulations*. Physics in Medicine & Biology, 55(2):N23, 2009.

[12] Sven Kühn, Wayne Jennings, Andreas Christ, and Niels Kuster. *Assessment of induced radio-frequency electromagnetic fields in various anatomical human body models*. Physics in Medicine and Biology, 54(4):875, 2009.

[13] Jorge J Moré, Burton S Garbow, and Kenneth E Hillstrom. *User guide for MINPACK-1*. Technical report, CM-P00068642, 1980.

[14] Richard H. Byrd, Peihuang Lu, and Jorge Nocedal. *A Limited-Memory Algorithm for Bound Constrained Optimization*. SIAM Journal on Scientific Computing, 1994.

[15] B.B. Beard, W. Kainz, T. Onishi, T. Iyama, S. Watanabe, O. Fujiwara, Jianqing Wang, G. Bit-Babik, A. Faraone, J. Wiart, A. Christ, N. Kuster, Ae-Kyoung Lee, H. Kroeze, M. Siegbahn, J. Keshvari, H. Abrishamkar, W. Simon, D. Manteuffel, and N. Nikoloski. *Comparisons of computed mobile phone induced SAR in the SAM phantom to that in anatomically correct models of the human head*. IEEE Transactions on Electromagnetic Compatibility, 48(2):397–407, 2006.

Part II

Massive MIMO

3

Massive MIMO Exposure in Indoor Industrial Environment

3.1 Introduction

Having studied the ATTO-floor exposure in Chapter 2, in this chapter we introduce the second technology outlined in Chapter 1 - massive MIMO. Massive MIMO is one of the most promising candidates as a 5G communication technology. First introduced in [1], it offers an unprecedented increase in spectral efficiency of a wireless link. It is achieved by equipping the base station (BS) with a large number of antennas compared to the number of simultaneously served users. The user equipment (UE) is a single antenna device. As mentioned in Chapter 1, the BS estimates the propagation channel through receiving uplink pilots. This channel-state information (CSI) is used at the BS to precode the signal it transmits, maximizing the desired signal strength at the receivers while minimizing interference. This is achieved by selecting the phases and amplitudes at the BS antennas (*precoding* them) such that their signals are combined constructively at the intended receivers and undergo a destructive interference at the other receivers. Various precoding strategies were devised and analyzed in literature [2]. The propagation environment and the precoding scheme used at the BS are the major factors influencing the electromagnetic field (EMF) distribution (Poynting vector) in vicinity of the receivers during the operation of a massive MIMO system.

Recently conducted theoretical studies were focused on the assessment of the realistic maximum power density levels and compliance boundary size. In [3]

analytical expressions were used to describe the statistical properties of the massive MIMO operation and in [4] the 3GPP stochastic channel model was involved. In both works the line-of-sight (LOS) scenario was studied as yielding worst-case human exposure and operation of the massive MIMO system was reduced to *beamforming*.

However, in a non-line-of-sight (NLOS) scenario such approach might no longer be feasible. As there is no direct path between the BS and UE, forming conventional 'beams' is not beneficial as the signal gets attenuated by obstacles. Instead, the BS exploits the knowledge of the channel and allocates its power to multi-path components. High spatial multiplexing gain, typical for a massive MIMO transmission, results in sharp power density peaks confined to a narrow spatial region in proximity of the UE's terminal.

This chapter presents a numerical approach for the evaluation of realistic EMF exposure to a massive MIMO BS downlink transmission in terms of the localized specific absorption rate (SAR). This has never been done before, to the best of the author's knowledge. It combines Ray-Tracing (RT) for deterministic geometry-based propagation calculation and the Finite-Difference Time-Domain (FDTD) method to assess exposure of a realistic human phantom.

Comparing LOS and NLOS modes of operation of a massive MIMO system could give insights into realistic exposure conditions.

In this chapter, models of an indoor industrial environment are studied. It is envisioned that factories of the future will be equipped with multitudes of autonomous robots and human workers, all of which will require fast and reliable wireless connection. A single massive MIMO BS could potentially provide the needed service due to a low Path Loss (PL) exponent and rich scattering in such scenarios [5].

Recent measurement campaigns performed with massive MIMO test-beds [6] in indoor environments report its distinctive features: multi-user consistency, spherical wavefronts, and non-stationarity across the BS array. Current stochastic MIMO channel modeling frameworks, e.g. COST 2010 [7] and QuaDRiGa [8], do not account for these effects. Although possible extensions were proposed [9, 10], they are yet to be experimentally validated [11]. On the other hand, geometry-based massive MIMO channel modeling using the RT method complemented with the Uniform Theory of Diffraction (UTD) has been reported to reproduce the aforementioned effects in both indoor [12] and outdoor environments [13].

The chapter is organized as follows. In Section 3.2, we explain the proposed numerical approach in detail, estimate the algorithmic complexity of the methods involved and the limits of their applicability. We also estimate the numerical error of the proposed method. Section 3.3 presents the results obtained in a model case of industrial indoor environment. Time-averaged free-space Poynting vector magnitude and SAR in a heterogeneous human phantom are assessed. It also contains the

discussion of the results with respect to the existing exposure guidelines.

3.2 Materials and methods

In this section, we explain the numerical approach. First, a high-level overview is given, where all steps involved are shown, and their connections are explained. Then, for each step, we elaborate the details. An example of its application is given for a model environment.

3.2.1 Numerical pipeline

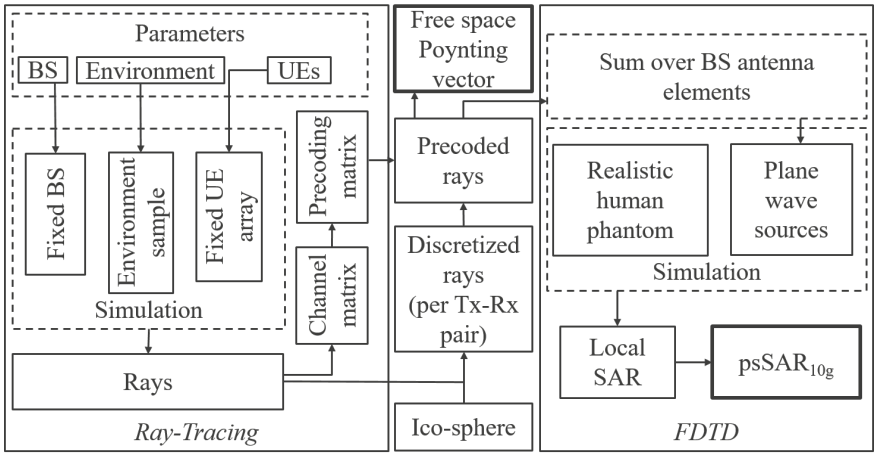

Figure 3.1: Numerical pipeline scheme. Ray-tracing, FDTD and the interface between them are shown.

A block-diagram of the proposed method is depicted in Fig. 3.1. It can be conveniently viewed as consisting of two components: RT and FDTD. The hybridization of these two methods was first introduced in [14], where it was used for indoor wireless propagation prediction; the results were compared to the measured data, showing 2 to 10 times lower relative error in predicting the E-field magnitude compared to pure RT. The same approach was also applied to the human exposure assessment to conventional single-antenna BS in an urban macrocell in [15]. The results demonstrated the significance of the "accurate modeling of the environment in which the exposure takes place". Peak-spatial SAR averaged over 10g (psSAR_{10g}) was reported to increase around two times with reflections from a nearby wall taken into account. Inclusion of the propagation environment in the simulation is expected to have even stronger effect on exposure produced by a massive MIMO BS.

An extensive study [16] based on sets of single-plane wave FDTD simulations with adult heterogeneous human phantoms reported psSAR_{10g} relative variation of around 300% with respect to the direction-of-arrival (DoA) of a plane wave. Therefore, a realistic modeling of the EMF-exposure should account for the expected DoA relative to the exposed subject. One way to achieve this is to utilize known DoA distribution for a particular type of environment when assessing the exposure statistically [17].

However, for a massive MIMO system directional information at the receiver side per BS antenna and inter-antenna correlation should as well be accounted for. These are often characterized via the notion of a *cluster* of scatterers, which is associated with a group of closely spaced DoAs [18]. A cluster can be described with its DoA and relative power distributions. In proposed stochastic models of the massive MIMO channel, a widely accepted approach is to generate cluster parameters according to appropriately chosen distributions. Whether a cluster is shared between two BS antennas is given by a probability function.

As the input of a RT simulation is a geometrical model of an environment (see Fig. 3.1), the RT approach has the following advantage over stochastic models: all the channel information is extracted from the environment model, rather than being sampled stochastically.

The choice of distributions in a stochastic model is equivalent to the definition of the RT simulation domain. We further discuss this in the analysis of the RT results.

We generate the geometry for RT simulations stochastically, described with a set of geometry parameters.

The directional information of the incidence at the UE is *spatially consistent*. Scatterer clusters emerge naturally as the strongest propagation paths, between the BS and a UE. Importantly, RT calculates DoA per individual BS antenna element based on the shape of the antenna array, its orientation in space, etc. Power distribution, phase, and time-delay of the incident rays are calculated from the length of the propagation paths (path loss), possible reflections, transmissions (Fresnel equations) and diffractions a ray undergoes during its propagation (Fig. 3.1, left).

Antenna radiation patterns are easy to incorporate into RT simulations, as it only requires scaling of the incident power with respect to direction of departure (DoD) at the transmitter and DoA at the receiver; it can be done as a postprocessing step of simulation results. This will be leveraged in Chapter 4 to evaluate the effect that coupling of the UE antenna with the user body has on the massive MIMO channel, the hot-spot, and the user exposure.

3.2.2 Ray-Tracing Simulation

The wireless channel modeling is performed using a ray-launching [19] variant of the RT method [20]. The commercially available REMCOM Wireless InSite 3.2 software package is used [21]. A general RT procedure relies on a ray-optics approximation of the Maxwell equations. A transmitter is modeled by launching rays from its center in a finite set of directions, distributed over the complete unit sphere. A ray is propagated through the environment predefined with its geometry and material properties, undergoing reflections, refractions, and diffractions, until its power reaches a predefined threshold. If a ray passes in the vicinity of a receiver (within the *ray reception sphere* [19]), it contributes to the total field at that receiver's location.

Given that the BS terminals are excited with a sinusoidal signal at frequency f_c, the ray-tracer calculates the channel transfer function between n^{th} BS antenna (Tx) and k^{th} UE (Rx) as

$$h_k^n = \sum_{r=1}^{s(k,n)} p_r \exp(-2\pi i f_c \tau_r), \tag{3.1}$$

where $s(k,n)$ is the total number of paths found between n^{th} Tx and k^{th} Rx points, p_r is the complex-valued impulse response through the r^{th} path and τ_r is the time-delay of the r^{th} path. Evaluating (3.1) for each Tx-Rx pair yields the frequency-specific channel matrix $\mathbf{H}(f_c)$ (Fig. 3.1). Obtaining full channel matrix requires calculation of $\mathbf{H}(f)$ at every sub-carrier frequency utilized by a massive MIMO system. Further in this chapter we carry out simulations at a single carrier frequency of 3.5 GHz, and $\mathbf{H}(f_c) \equiv \mathbf{H} \in \mathbb{C}^{K \times N}$, where K and N is the overall number of simultaneously served UEs and active BS elements, respectively.

The channel Gram matrix is commonly used for analysis of a massive MIMO system performance and given by

$$\mathbf{G} = \mathbf{H}\mathbf{H}^H, \tag{3.2}$$

where $(\cdot)^H$ denotes the conjugate transpose of a matrix. It is a positive-semidefinite matrix of dimensions $K \times K$. Its k^{th} diagonal element is proportional to the power received by the k$^{\text{th}}$ UE, and the magnitude of its element with indices ij is proportional to the interference between i$^{\text{th}}$ and j$^{\text{th}}$ UEs in downlink.

3.2.2.1 Model of the environment

The ray-tracing simulations were done the in the indoor environment shown in Fig. 3.2. The floor-plan is a 40 m×20 m×5 m rectangular room. A dielectric material with parameters $\varepsilon_r = 7,\ \sigma = 1.5 \cdot 10^{-2}$ S/m [22, 23] is assigned to its walls, floor and ceiling (concrete material model).

Scatterers are placed along the perimeter of the room, no more than 3 m away from the walls, distributed in the xy-plane with the Poisson Disc sampling algorithm [24]. The Poisson Disc sampling algorithm assures that the scatterers do not intersect and distributes them evenly inside the bounded region. The scatterers are cuboids of fixed width and length (2 m×0.5 m) and height sampled uniformly in the range from 2 m to 3 m. Each scatterer is independently rotated around the vertical axis, through the object's center, at an angle sampled uniformly in $[0, 2\pi)$.

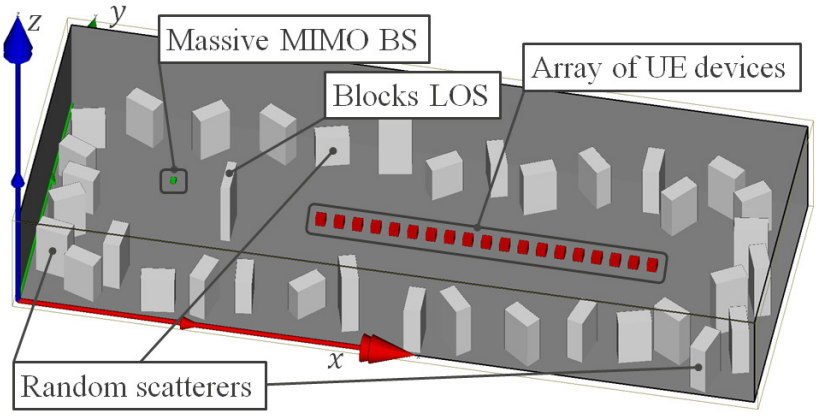

Figure 3.2: A sample of the environment in a ray-tracing simulation. Floorplan has the dimensions of 40 m×20 m×5 m. The floorplan and Tx-Rx arrangement is fixed, while cuboid scatterers are generated independently for each sample.

Fig. 3.2 shows the location of the massive MIMO BS (green) and a linear array of receivers (red). The center of the BS array is located at $x = 7$ m, $y = 10$ m, $z = 4$ m in the coordinate system depicted in Fig. 3.2. The BS consists of 36 vertically polarized isotropic radiators arranged in a planar 6-by-6 array in yz-plane with a uniform 1λ (approx. 86 mm) spacing between the elements. All elements of the array are fed with equal power, such that the total radiated power of the BS is 1 W. In this study, we do not assign individual antenna patterns to the BS elements in order to simplify the analysis of the results.

19 UEs are arranged in a linear array with equal 1 m spacing spanning from 15 to 33 m along the x-axis. All UEs are elevated at equal height of 1.5 m (along the z-axis). A receiver is modeled with a single vertically polarized isotropic antenna.

In addition, one cuboid of size 2 m×0.2 m×4 m can be placed at the fixed location (x =10 m, y =10 m), blocking the direct path between the BS and the array of receivers (see Fig. 3.2). We further refer to the setup where the cuboid is present as the *NLOS* scenario and the setup without the cuboid as the *LOS* scenario. This model generates realistic industrial environments of a fixed layout (e.g. a

warehouse, assembly line) [25].

A 0.02° ray-spacing is set for the ray-launching at the Tx. Each antenna element had vertical polarization and used an isotropic radiation pattern. THe isotropic radiation patterns at both Tx and Rx are aimed to model the most generic wireless channels. Additionally, this will also aid isolating the effect that the coupling of the UE with the human body has on the channel (see Chapter 4). Other RT solver parameters are summarized in Table 3.1 and were chosen as suggested in [23].

Parameter	Reflections	Refractions	Diffractions	Threshold
Value	6	2	2	-80 dB(V/m)

Table 3.1: Parameters of the RT solver.

3.2.2.2 Discretization of incident rays

A ray $r_{n,k} = \{f_c, \mathbf{n}, \mathbf{E}, \mathbf{H}\}$ in the RT method is described by the frequency f_c, DoA vector $\mathbf{n}$ of the plane wave it represents (a unit vector *opposite* to the direction of the plane wave propagation), complex amplitudes of its electric and magnetic fields $\mathbf{E}, \mathbf{H}$, and indices of a Tx-Rx pair (n, k) it is calculated for.

Many modern FDTD software tools feature a functionality to create plane wave sources. We use this feature available in EM-FDTD solver of Sim4Life v4.0 (ZMT, Zürich, Switzerland) and model an incident ray as a plane wave source propagating in the entire domain.

The simulation time is nearly linearly proportional to the total number of plane wave sources in it. Moreover, the number of rays incident at the specific point is also proportional to the number of the antennas at the BS, as each antenna is traced independently.

The overall number of rays that reach a particular UE depends on the environment, Tx-Rx positions, and attenuation threshold, after which a ray is discarded; e.g., in the studied environment with the power threshold of -50 dB and source ray spacing of 0.02°, on average around 220 rays per Tx-Rx pair were observed, resulting in approximately $8 \cdot 10^3$ rays per UE.

Such large number of plane waves in a simulation results in a long run time and renders it impractical to conduct the simulations in extensive sets of environment samples. It is computationally beneficial to combine rays with closely aligned propagation directions before introducing them into the FDTD domain.

To reduce the number of plane waves in an FDTD simulation, hence, decreasing simulation time, we perform DoA discretization of the incident rays at each UE. We define a grid on a unit sphere and use the normal vectors of its elements to approximate DoA of the rays calculated with the RT method. If the set is sufficiently large and covers all DoA space in a uniform manner, the error introduced by this

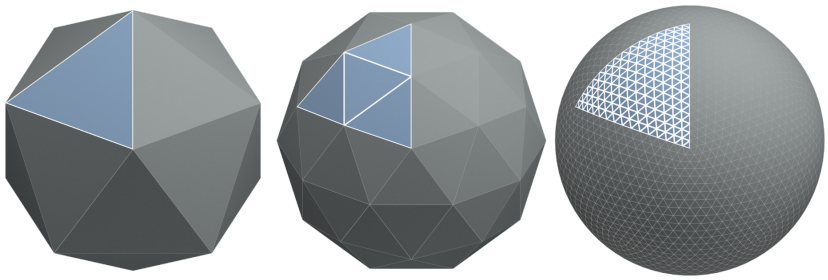

Figure 3.3: Icosahedral triangulation of a sphere of frequency a) 1 (Icosahedron, 20 faces), b) 2 (80 faces) and c) 16 (5120 faces).

procedure is expected to be small for any distribution of DoA of the incident rays. This procedure allows adding up the complex amplitudes of the discretized rays having equal DoAs, decreasing the total number of plane waves in the FDTD simulation (and proportionally decreasing CPU time).

We use a geodesic spherical grid based on subdivision of an icosahedron. By subdividing every edge of the icosahedron into i segments, triangulating its faces and projecting newly created vertices into the unit sphere, an icosahedral triangulation of a sphere (icosahedral sphere, ico-sphere) of frequency i is generated. The angle between any two adjacent triangles (a dihedral angle) of an ico-sphere is nearly constant, which makes its surface a largely isotropic spherical grid.

For each ray the calculated DoA vector $\mathbf{n}$ is replaced by $\tilde{\mathbf{n}}$, being the outer normal of the ico-sphere face $\mathbf{n}_i$ with the maximal orthogonal projection onto $\mathbf{n}$,

$$\tilde{\mathbf{n}} = \arg\max_{\mathbf{n}_i}\{(\mathbf{n}, \mathbf{n}_i)\}. \tag{3.3}$$

i	Face count	$\angle(\mathbf{k}_1, \mathbf{k}_2),\ [^\circ]$	$d_i,\ [\lambda]$	$d_i,\ [m]$
1	20	41.81	1.5	0.12
2	80	18.02	3.23	0.26
4	320	7.8	7.37	0.59
8	1280	3.19	17.96	1.44
16	5120	1.41	40.73	3.26

Table 3.2: Distance between interference peaks for different ico-sphere frequencies.

To estimate the error introduced by the discretization procedure, lets consider two plane waves with wave-vectors $\mathbf{k}_1$ and $\mathbf{k}_2$, such that $|\mathbf{k}_1| = |\mathbf{k}_2|$ and $\angle(\mathbf{k}_1, \mathbf{k}_2) \leq \beta_i$, where β_i is the largest dihedral angle of an ico-sphere of frequency

i. Then the shortest distance between two neighboring interference pattern maximas (*fringe spacing*) is given by $d_i = \lambda / \sin \beta_i$ [26]. Table 3.2 presents values of d_i calculated for $i \leq 16$. Starting from $i = 4$, the fringe spacing becomes larger than the expected domain size. We use this as a starting value in the following numerical evaluation of the associated error.

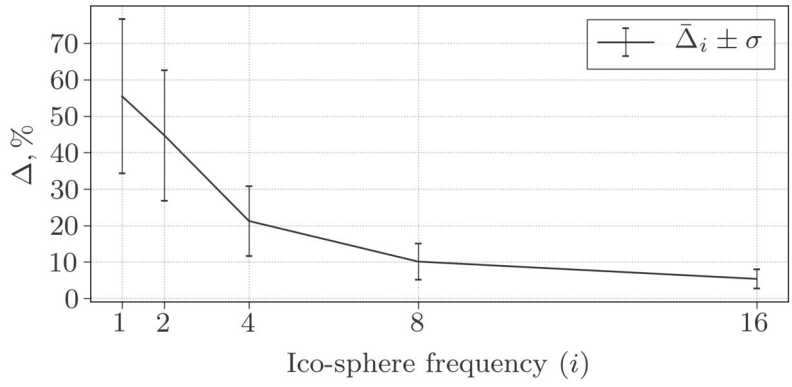

Figure 3.4: Relative error of the total power incident along the x-axis. Sample average and standard deviation over 100 RT simulations are shown.

To numerically estimate the error introduced by DoA discretization in the simulated environments, we compare the time-average power flux density $\mathbf{S}$ calculated from the full set of rays obtained with the RT method and their discretized approximations $\mathbf{S}_i$ for icosahedral sphere frequencies i listed in the Table 3.2. We integrate the absolute difference between x-components of $\mathbf{S}$ and $\mathbf{S}_i$ and their mean value over a 190 mm $\times$ 240 mm rectangle A in the yz plane and use the ratio of two as a measure of the error

$$\Delta_i = \frac{\int_A |S_x - S_{x,i}|}{\int_A |S_x|}. \tag{3.4}$$

The area of integration is the projection of the phantom's head bounding box on the yz plane (wich is the phantom's coronal plane). As such, Δ_i approximates the relative error of the total power incident at the phantom's head along the x-axis when discretizing the rays using the ico-sphere of frequency i (see Fig. 3.5). The x-axis is selected, as this is the dominant propagation direction connecting the BS and the Rx array. We calculated Δ_i for 100 samples of the environment in Fig. 3.2 with the NLOS scenario; its value averaged over all samples and all UE locations along with its standard deviation σ as a function of i are shown at Fig. 3.4.

Mean Δ_4 approximately equals 20% and for some samples exceeds 30%. However, Δ_i falls rapidly as i increases. Mean Δ_{16} is found to be around 5.5%

with its value staying below 12% for all samples. Numerical uncertainty of exposure assessment caused by the finite FDTD grid resolution is reported to be around 10% for the grid step of 2 mm and frequencies below 5 GHz [27]. Thus ico-sphere of frequency 16 is considered to provide a sufficiently accurate approximation for the incident field.

In the studied environment, the overall number of the discretized rays for a given UE rarely exceeded 250, which reduced the FDTD simulation run-time by a factor of 30. This approximation is further used in FDTD simulations with a realistic human phantom.

3.2.3 FDTD Simulations

Sim4Life FDTD software is used for the simulations described in this section. The simulation domain is shown in Fig. 3.5. The EMF-exposure is assessed using the ViP v.3.1 Duke heterogeneous human phantom [28] (a different section of this phantom is used in Chapter 2). Further throughout the thesis we simply refer to it as *the phantom*. $\mathrm{psSAR}_{10\mathrm{g}}$ is used to measure the exposure as highly focused energy distributions are expected (hotspots).

The center of the domain is coincident with the position of the UE, where the exposure is being assessed. The UE is assumed to be a mobile phone in a typical usage scenario close to the head. Accurate modeling of the usage scenario requires positioning the phantom inside the domain preserving its arrangement relative to the UE. Here we use a simplified approach by centering the phantom's head at the position of the UE (center of the domain).

In addition, we only include the phantom's head into the FDTD domain to reduce the computational demand. The domain dimensions were set to 300 mm $\times$ 300 mm $\times$ 250 mm to fully enclose the phantom's head.

The discretization step did not exceed 2 mm which resulted in more than 40 grid steps per wavelength at 3.5 GHz. The total number of voxels is around 3.3×10^6.

3.3 Results

3.3.1 Massive MIMO channels

To evaluate the massive MIMO performance in the proposed environment we investigate the channel matrices and compare their properties with those of the theoretical i.i.d. Rayleigh channels.

Fig. 3.6a depicts a channel Gram matrix, in which the channel coefficients are modeled with independent sampling from a circularly symmetric Standard Normal distribution, according to the Rayleigh fading model. The dominance of its diagonal elements is conditioned by the law of large numbers, as any off-diagonal element is the average of a large number (number of the BS antennas N) of random

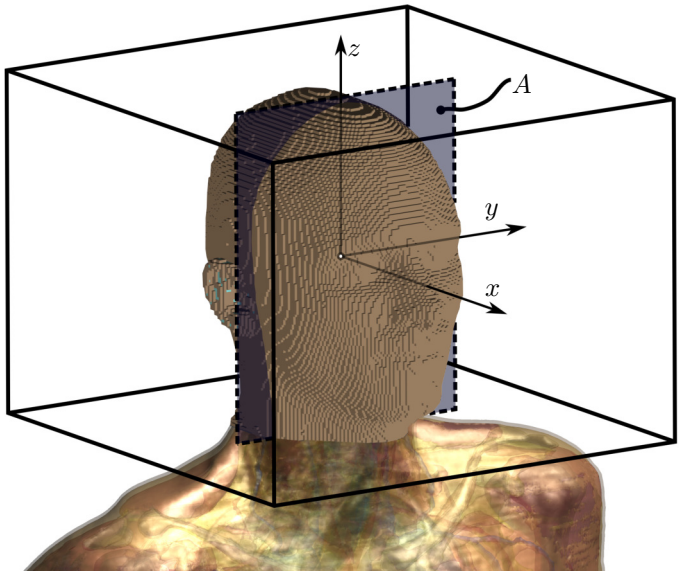

Figure 3.5: A computational domain of the FDTD simulation. Domain boundaries are shown with solid black lines. Voxels of the ViP v.3.1 Duke phantom's head, included into the domain, are shown. Dashed line depicts to boundary of the integration surface A (shaded area) in (3.4).

variables with zero-mean. At the same time, any diagonal element is the square of the absolute channel impulse response, and proportional to the power received by the corresponding UE.

Fig. 3.6b shows an example of a channel Gram matrix calculated with the RT method in the NLOS scenario. Relative magnitude of a diagonal element decreases with increasing UE index. This is the result of the PL, as the distance from the BS to the corresponding UE increases.

The arithmetic mean of the channel Gram matrices obtained in 100 NLOS environment samples are depicted in Fig. 3.6e. Comparing Fig. 3.6b and Fig. 3.6e, one can see that the channel impulse response is indeed uncorrelated between independently generated environment samples. The correlation between channels (off-diagonal elements at Fig. 3.6b) occasionally reaches the order of magnitude of the signal (diagonal elements), but vanishes on average.

LOS channels exhibit much higher correlation (Figs. 3.6c and 3.6f) between farther spaced receivers compared with NLOS, which is explained by the shared direct path component. The correlation further increases when strong scatterers are shared between UEs, as illustrated at Fig. 3.6c for UE#2 and UE#3, in which case the channels become nearly identical up to a constant phase shift. On average the diagonal elements dominate, though the observed correlation is higher than the one

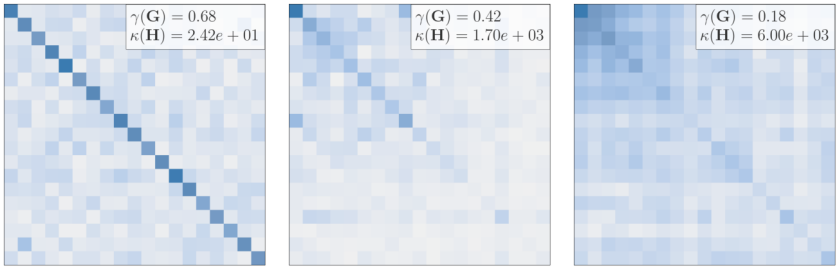

(a) i.i.d. Raleigh channels. ***(b)*** NLOS. ***(c)*** LOS.

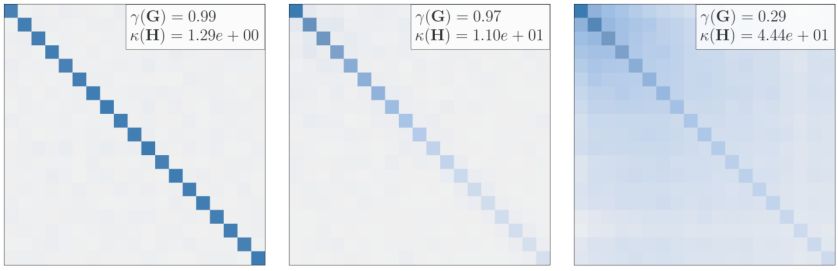

(d) Avg. i.i.d. Raleigh. ***(e)*** Average NLOS. ***(f)*** Average LOS.

Figure 3.6: A comparison of normalized channel Gram matrices ($K = 19$, $N = 36$). (a): An example of i.i.d. Rayleigh channel model with $h_n^k \sim \mathcal{CN}(0,1)$. (b): An example of NLOS scenario (see Fig. 3.2). (c): An example of LOS scenario. (d): Average of 100 i.i.d. Rayleigh samples. (e): Average over 100 NLOS environment samples. (f): Average over 100 LOS environment samples.

of NLOS or i.i.d. Rayleigh channels.

The quantitative analysis of the channel is often performed using the channel matrix Singular Value Spread (SVS) $\kappa(\mathbf{H})$ [29] and channel correlation Matrix Power Ratio $\gamma(\mathbf{G})$ (MPR) [13].

$\kappa(\mathbf{H})$ is the ratio between the maximum and the minimum singular values of $\mathbf{H}$. SVS is the measure of correlation between the channel vectors: it equals to 1 for perfectly orthogonal channels (all singular values equal 1) and larger than one for non-orthogonal channels. $\kappa(\mathbf{H})$ close to 1 indicates that the channel exhibits *favorable propagation conditions* for the operation of a massive MIMO system.

$\gamma(\mathbf{G})$ is the ratio between the sum of squared absolute values of the diagonal elements of $\mathbf{G}$ and the sum of all its elements absolute values squared

$$\gamma(\mathbf{G}) = \frac{\sum_{i=1}^{K} |g_{i,i}|^2}{\sum_{i=1}^{K}\sum_{j=1}^{K} |g_{i,j}|^2}. \tag{3.5}$$

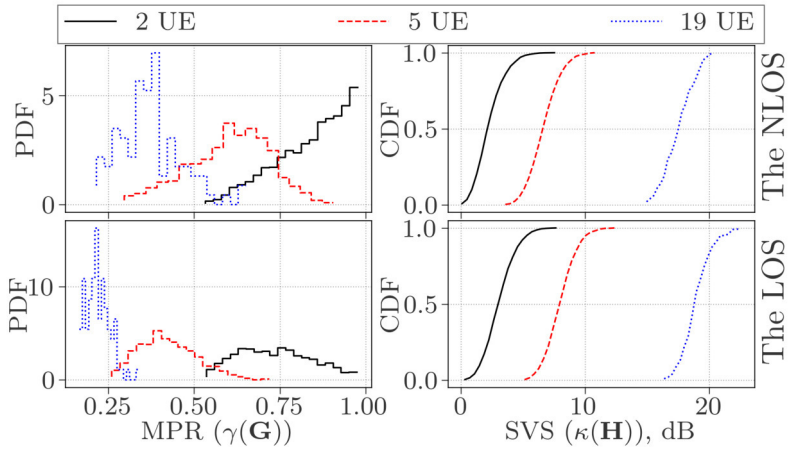

Figure 3.7: Probability Density Function of $\gamma(\mathbf{G})$ (left column) and Cumulative Distribution Function of $\kappa(\mathbf{H})$ (right column) for 2, 5 and 19 active adjacent UEs. Results for the NLOS (top row) and LOS (bottom row) scenarios are shown.

$\gamma(\mathbf{G})$ is the portion of the electromagnetic energy that is focused at the intended receivers instead of interfering with other receivers. In i.i.d. Rayleigh channels $\gamma(\mathbf{G})$ tends to 1 and goes to 0 when a significant inter-channel correlation is present.

To evaluate the variation of $\kappa(\mathbf{H})$ and $\gamma(\mathbf{G})$ in the studied environment model (and quantify its suitability for the deployment of a massive MIMO system) we select all sub-arrays of n consecutive UEs from the original UE array and calculate the above quantities for 100 environment samples. Fig. 3.7 depicts the sample Probability Density Function (PDF) of $\gamma(\mathbf{G})$ and Cumulative Distribution Function (CDF) of $\kappa(\mathbf{H})$ for $n = 2, 5$ and 19 (whole UE array) in LOS and NLOS scenarios. For larger n always a larger SVS is observed, in agreement with measurement results in [30] and the results of RT simulations in [13].

The NLOS scenario offers better propagation conditions compared with LOS, which agrees with [31]. This is expected, as in the LOS scenario all UEs are positioned along one straight line, which is also the strongest propagation path, i.e. the phase of the signal is correlated with its DoA for all receivers. However, the SVS rarely exceeds 10 dB in both scenarios for $n \leq 5$, which means that the BS is capable at providing a good service to up to 5 closely spaced UEs. Channels to more sparsely distributed users tend to be less correlated. This allows to conclude that the proposed environment model is well-suited for the deployment of massive MIMO and the average EM-field incident at the UEs can be treated as realistic.

3.3.2 Power flux density focusing in free space

In this section we examine the behavior of the time-averaged power density flux in free space in the neighborhood of the UE to which the transmission occurs. A simple case when the BS transmits to a single-user only is studied. This is a potential worst case exposure-wise, as the BS attempts to focus all the available power at a single user position rather than spreading it between multiple locations in a multi-user case.

Strictly speaking, the results of the RT simulation are only valid in the point in space that is coincident with the position of the assessed UE. However, spatial distribution of the EM-field in proximity of the point is determined by the phase-amplitude relation of the incident plane waves if their DoA variation close to that point is sufficiently small.

To examine to which extent this assumption holds, we performed 100 RT simulations in the NLOS scenario (Fig. 3.2) with a linear array of densely spaced (10 mm separation) receivers spanning for 0.5 m along the x-axis at 20 m distance from the BS. On average, correlation of the incident rays power as a function of DoA is found to be above 60% for the UE separation distance less than 200 mm. Therefore, we further examine EM-field distributions in a finite space region.

In this and following sections we apply Equal Gain Transmission (EGT) scheme [32] to precode the discretized rays. The EGT is realized by setting the phase of the signal at every BS antenna element opposite to the phase of the received signal at the terminal of the UE to which the transmission is intended, while maintaining the amplitude of the signal equal at all BS antennas. The EGT scheme is less demanding to the BS hardware complexity, compared to e.g., Maximum Ratio Transmission scheme (see Chapter 4), and is considered as a candidate for practical massive MIMO implementations [33, 34]. Using the definition of the channel matrix element (3.1), we obtain EGT-precoded complex E-field amplitude of the j^{th} ray incident at the k^{th} UE from the n^{th} BS antenna as

$$\hat{\mathbf{E}}^{j}_{n,k} = \mathbf{E}^{j}_{n,k} \exp(-i \arg(h^{n}_{k})). \tag{3.6}$$

Then the E-field at the point $\mathbf{r}$ in proximity of the k^{th} user is found taking the sum over all rays and BS antennas

$$\mathbf{E}^{EGT}_{k}(\mathbf{r}) = \sum_{n=0}^{N} \sum_{j} \hat{\mathbf{E}}^{j}_{n,k} \exp\left(-i \mathbf{k}_{j} \mathbf{r}\right), \tag{3.7}$$

where $\mathbf{k}_j$ is the wave-vector of the j^{th} ray. Equations for the magnetic field are obtained by substituting $\mathbf{H}$ for $\mathbf{E}$ in (3.6) and (3.7).

Time-average power density flux is the real part of the EM-field Poynting vector [26]

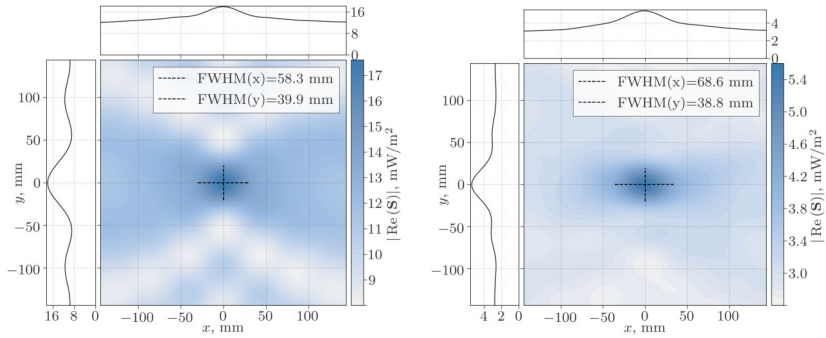

(a) The LOS scenario.

(b) The NLOS scenario.

Figure 3.8: Spatial distribution of the time-average power flux density in the xy-slice through the location of the UE, averaged over all UEs in 100 environment samples. Total BS transmitted power is normalized to 1 W. (a): The LOS scenario; (b): The NLOS scenario.

$$\mathbf{S}_k^{EGT}(\mathbf{r}) = \mathrm{Re}\left(\frac{\mathbf{E}_k^{EGT} \times \mathbf{H}^{*}{}_k^{EGT}}{2}\right). \tag{3.8}$$

We evaluated (3.8) on a uniform rectilinear two-dimensional grid in the xy plane at $z = 0$ constructed for all UEs in the LOS and NLOS scenarios for 100 environment samples.

Fig. 3.8a and 3.8b show spatial distributions of $\mathbf{S}_k^{EGT}(x, y)$ averaged over UE locations and environment samples for LOS and NLOS scenarios respectively. They illustrate the average power flux density gain in the studied environment model that the BS delivers. The BS is located in the negative x-axis direction at $y = 0$. In both cases, the maximum power density is observed in the center of the domain (UE antenna terminal). This is the effect of focusing achieved by precoding of the transmission by (3.6): on average the signal arrives at the receiver having zero-phase and adds-up coherently. It is important to emphasize that not all the propagation paths combine coherently at the center. A channel coefficient (one for each BS antenna) is an algebraic sum of the receiver voltages induced by signals arriving from multiple propagation paths, with their amplitudes and phases determined by the propagation environment. It is by coherently combining instantaneous field distributions produced by multiple antennas, that the focusing is achieved. The less correlated the signal response between the antennas is (that is the less alike these individual field distributions are) the sharper the field enhancement at the receiver can be produced.

In this regard the difference between LOS and NLOS scenarios is evident. In the LOS scenario the strongest propagation paths, being nearly collinear with the

positive x-axis direction, have narrow angular spread, which results in interference patterns with wide maxima. In contrast, when direct paths are obstructed, incident power has a more uniform and wide angular spread; this results in higher angular diversity in the incident rays (larger "aperture") and sharper focusing along y-axis, as can be seen at Fig. 3.8b.

On the other hand, in the NLOS scenario the strongest propagation paths are blocked, which results in more than 3 times lower absolute average of $\mathbf{S}^{EGT}(0,0)$.

To compare the focusing effect in both scenarios we calculate full width at half maximum (FWHM) of the spatial distribution relative to the background, along x and y axes, as shown at the top and left side of Fig. 3.8a and 3.8b.

For LOS and NLOS we found FWHM(y)$\simeq$39 mm or 0.45λ and FWHM(x)$\simeq$63 mm or 0.74λ respectively. We use the average of two values as the focusing performance indicator, which in this case approximately equals 51 mm or 0.59λ.

Another measure of focusing performance is the power density gain reached with the EGT precoding relative to power density of non-precoded BS transmission. This aspect and spatial variation of the power density at a larger scale is discussed in more details in the following sections.

3.3.3 Spatial distribution of SAR

We use psSAR$_{10g}$ to study localized exposure in the head of the heterogeneous phantom model as described above. Due to a highly focused EM-field distribution in proximity of the head, peak-spatial SAR averaged over 10-gram cube is a suitable quantity for the EMF-exposure estimation. 10-gram averaging cube and the maximum permissible psSAR$_{10g}$ are standardized by the International Commission on Non-Ionizing Radiation Protection (ICNIRP) in [35].

The FDTD simulations are performed for two rotation angles of the phantom (0° and 90°) relative to the BS were conducted for each environment sample. As discussed in Section 3.2, psSAR$_{10g}$ varies significantly with the incidence direction; exposure from the back of the head (0° rotation) and exposure from the side (90° rotation) are examined to study this effect.

Fig. 3.9a and 3.9b depict the distributions of SAR$_{10g}$ in a horizontal slice of the phantom's head, averaged over 19 UEs in the LOS scenario, exposed from the back and from the side respectively. When exposed from the back the maximum psSAR$_{10g}$ value is almost two times lower compared to the one found with exposure from the side setup. This is largely explained by the irregular structure of the ear, where the peak-cube is a almost always found in the side-exposure case, which agrees with a single-plane wave exposure studied in [16]. More generally, this effect can be attributed to the fact that in the LOS scenario most of the radiation is incident from the half-space where the BS resides. Location of the peak-cubes are on average aligned with the direction to the BS in LOS for both angles of rotation,

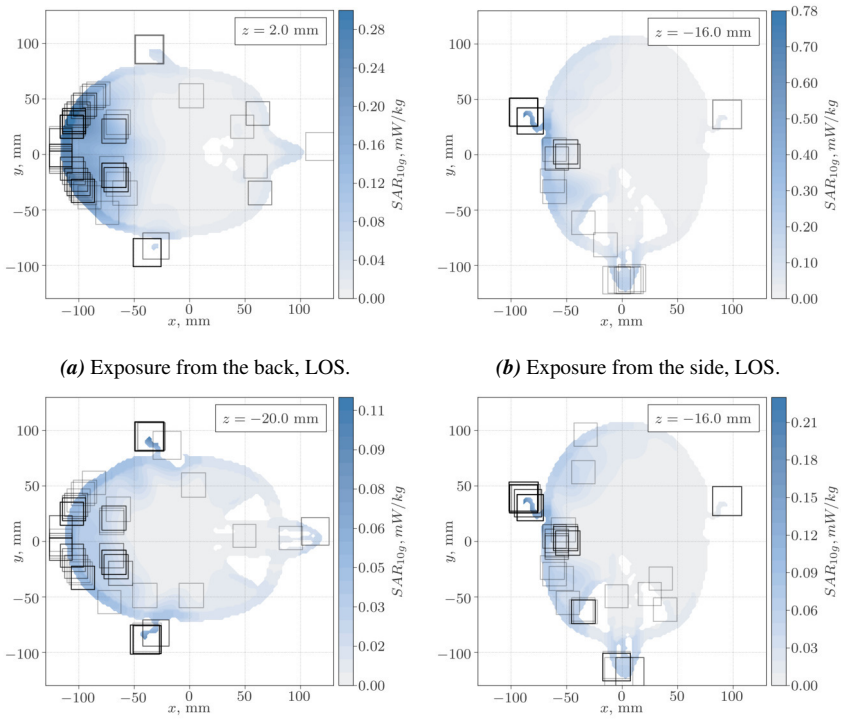

(a) Exposure from the back, LOS.

(b) Exposure from the side, LOS.

(c) Exposure from the back, NLOS.

(d) Exposure from the side, NLOS.

Figure 3.9: Color shows SAR_{10g} distribution, normalized to 1 W BS power and averaged over all 19 UEs in 10 environment samples; z coordinate of the slice is coincident with the maximum average SAR_{10g} and indicated in the top-right corner; black squares depict peak-$psSAR_{10g}$ cubes in each exposure sample projected onto the slice. (a): Exposure from the back in the LOS scenario; (b): Exposure from the side, LOS; (c): Exposure from the back, NLOS; (d): Exposure from the side, NLOS.

which also supports the argument above. Most of the $psSAR_{10g}$ cubes are found in the top of the head when the phantom is exposed from the back, which is why the slice depicted on Fig. 3.9a is located higher than on the others of Fig. 3.9.

Distributions of SAR_{10g} for two angles of the phantom's head rotation averaged over 10 environment samples and all UE positions in NLOS scenario are shown on Fig. 3.9c and 3.9d. As mentioned in Section 3.3.2, NLOS scenario results in a broader distribution of DoA in the incident rays. Thus the location of the peak-cube in the phantom's head is less correlated with the direction to the BS (or the angle of rotation of the head) compared with the LOS scenario. For both the 0° and 90° degrees rotation in Fig. 3.9c and 3.9d, most of the peak-cubes were located in the

ears.

3.3.4 Large-scale variation of the localized SAR

In this section we evaluate the power density in free space and psSAR_{10g} in the phantom's head as a function of the UE distance from the BS.

3.3.4.1 LOS

Results for the LOS scenario are given in Fig. 3.10a. The graph at the top depicts the sample average of the free-space power flux density, calculated for 100 environment samples.

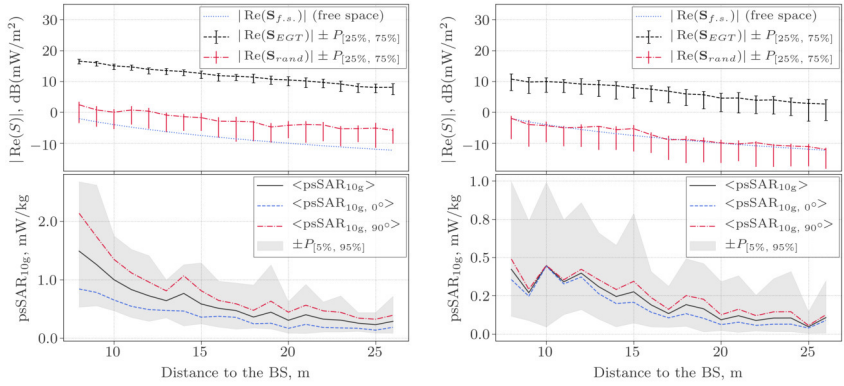

(a) The LOS scenario.

(b) The NLOS scenario.

Figure 3.10: As a function of distance to the BS. Top row: time-averaged power flux density at the locations of the UE. Black dashed line shows EGT-precoded sample average and error-bars denote 25$^{\text{th}}$ - 75$^{\text{th}}$ percentile range; red dash-dotted line shows average power density with no precoding applied; blue dotted line gives a free-space path-loss reference. Bottom row: psSAR_{10g} in the phantom's head. Black solid line shows average over 100 environment samples and 2 phantom rotation angles; blue dashed and red dash-dotted graphs show rotation-specific average values, for 0° and 90° rotation angles respectively; grey shaded area marks 5$^{\text{th}}$ - 95$^{\text{th}}$ percentile range. All values are normalized to 1 W BS total transmitted power. (a) The LOS scenario. (b) The NLOS scenario.

$\mathbf{S}_{EGT}$ and $\mathbf{S}_{rand}$ are the free-space time-averaged Poynting vectors evaluated at the location of the UE when the BS antennas transmit with EGT-precoded and with independent random (in $[0, 2\pi)$) phases respectively. The ratio $|\mathbf{S}_{EGT}|/|\mathbf{S}_{rand}|$ is the EGT-precoding gain in terms of the time-averaged power density. It is fairly stable over the distance; varying between 13.2 and 15.5 dB, its average approximately equals 14.4 dB. It is also interesting to compare these values with

the power density calculated with the free-space path loss model $\mathbf{S}_{f.s.}$, shown with a dashed blue line. It is calculated using Friis free-space transmission formula [32] for a single isotropic radiator with the total power of 1 W as the BS. Everywhere $\mathbf{S}_{rand}$ is larger than $\mathbf{S}_{f.s.}$ with their ratio increasing from around 3.9 to 6.9 dB as the distance to the BS increases. This can be explained by the presence of the PEC scatterers which reflect EM-energy and channel it through the environment, instead of absorbing it. This is confirmed by extensive measurement campaigns [36] carried out in industrial indoor environments, which report PL exponent less than 2 in the studied frequency range.

The graph at the bottom of Fig. 3.10a depicts the maximum $\text{psSAR}_{10\text{g}}$ averaged over 10 LOS environment samples with the phantom exposed from the back (0° rotation, blue line), side (90° rotation, red line) and 5$^{\text{th}}$ - 95$^{\text{th}}$ percentile range taken from the distribution of all 20 exposure values (shaded region). At all UE locations exposure from the side is found to be higher than from the back by a factor of 2.6 on average. Overall, the average maximum $\text{psSAR}_{10\text{g}}$ value is closely proportional to $\mathbf{S}_{EGT}$ in the hotspot with the proportionality factor varying from around $2.7 \cdot 10^{-2}$ m^2/kg to $4.4 \cdot 10^{-2}$ m^2/kg.

3.3.4.2 NLOS

Power flux density magnitude in the NLOS scenario is shown at Fig. 3.10b (top) (100 samples). The precoding gain in the NLOS scenario varies slightly more with distance and has a nearly equal absolute average value of around 14.3 dB, compared with LOS. The former is the result of a more rich scattering environment which NLOS provides, as mentioned in the previous section.

Another interesting effect is the increased relative variation of EGT-precoded power density $\mathbf{S}_{EGT}$ for all UE positions. This is expected: the signal variation is related to the geometry variation across the environment samples. Randomly generated scatterers play a less significant role in the non-obstructed propagation (LOS), as the direct component is constant and shared among all samples.

The comparison of the large-scale fading with the free-space model shows a larger PL in the NLOS. This is the effect of shadowing by the LOS-blocking scatterer (see Fig. 3.2). It is interesting that UEs at an intermediate distance from the BS experience less shadowing; it might indicate that the signal is more likely to reach those UE locations through less interactions with the environment (e.g. with only 1 reflection).

At the bottom of Fig. 3.10b, the $\text{psSAR}_{10\text{g}}$ variation with distance in 10 NLOS environment samples is depicted. It is found to be around 3.5 times lower than that of the LOS scenario. The relative difference between exposure from the back and from the side is found to be lower in NLOS than in LOS as a result of a less directive incidence. Exposure from the back is as well lower than from the side, though for some UE their average values are very close (e.g. at 10 and 25 m distance).

Another effect of the wider DoA spread in the NLOS scenario, mentioned in Section 3.3.3, is that the EMF power is deposited and distributed more evenly over multiple regions of the head, as can be seen comparing the top and bottom plots of Fig. 3.9. As a result, the maximum psSAR_{10g} normalized to the power density in the free-space hotspot (obtained in the same exposure conditions) is lower on average in the NLOS compared to that in the LOS case.

3.3.5 Comparison with the guidelines

From the evaluated normalized exposure, we now determine the power that the BS would need to transmit in order to violate the ICNIRP basic restrictions for the general population (2 W/kg [35]) at a given distance in the LOS and NLOS scenario, denoted as P_{LOS} and P_{NLOS} respectively.

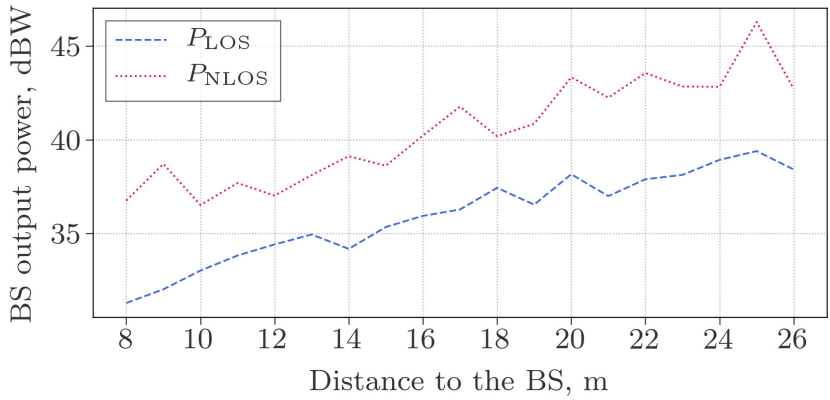

Figure 3.11: BS output power violating ICNIRP guidelines. Blue dashed line - the LOS scenario; red dotted line - NLOS.

Fig. 3.11 presents P_{LOS} and P_{NLOS} as functions of distance to the BS. P_{LOS} increases from around 31 to 39 dBW nearly linearly with distance. P_{NLOS} has a slightly steeper trend line and on average exceeds P_{LOS} by 5 dB. As an example, at the shortest studied distance (8 m) this results in the BS transmitted power per antenna limits of around 1.3 kW in the LOS scenario and around 5 kW in the NLOS scenario, which by a large margin exceeds potential transmit power of indoor wireless communication systems.

3.4 Conclusions

This chapter presented a numerical framework that for the first time allows to estimate the human EMF-exposure and localized absorption caused by a massive MIMO system. We applied the method to a generic model of an indoor industrial environment with a single massive MIMO BS. The calculated wireless channels were analyzed, and the results were compared to the data available in the literature, showing good agreement. The gain of the system in terms of the time-average power flux density at the receiver antenna terminal was obtained when using EGT precoding at the BS. In the assumption of single-user transmission, exposure in terms of psSAR_{10g} was assessed for users in LOS and NLOS propagation conditions at distances to the BS ranging from 8 to 26 m. Detailed results presenting psSAR_{10g} distributions and peak-cube locations are discussed with respect to the exposure conditions. psSAR_{10g} variation with distance to the BS was analyzed and compared to the power density observed in free space at the same location. Finally, maximum allowed powers of the massive MIMO BS were obtained in LOS and NLOS scenarios.

The main limitation of the presented method is that the channels of the UE was obtained directly from the RT simulations. Though the RT method outputs physically accurate and spatially consistent DoAs of the incident EMF, it implies that the UE is located sufficiently far from any reflecting or absorbing objects. However, in realistic scenarios, such as the one studied in this chapter, the UE is positioned in a close proximity to the phantom. This alters the UE's free space radiation pattern (in receive), mainly through absorption by the user body. In turn, this alters the channel matrix seen by the BS, and therefore its transmit weights. Propagation paths blocked by the user body would contribute less to the channel matrix, compared to the ones that reach the UE unobstructed. It is reasonable to assume that precoding schemes that maximize the received signal would then allocate a larger portion of the transmit power to the paths that result in less absorption. Moreover, the increase in the UE antenna pattern directivity should be expected to improve the system performance in scenarios with multiple UEs by acting as a spatial filter to select the UE-specific propagation paths (assuming the high-gain directions are not shared by the UEs).

The next chapter extends the approach introduced here to account for the coupling effects of the UEs and the user body. The effect of the perturbed UEs' radiation patterns on the channel matrix is investigated. In addition, more advanced precoding techniques and multi-user scenarios are explored from the exposure point of view.

References

[1] Thomas L Marzetta. *Noncooperative cellular wireless with unlimited numbers of base station antennas*. IEEE Transactions on Wireless Communications, 9(11):3590–3600, 2010.

[2] Fredrik Rusek, Daniel Persson, Buon Kiong Lau, Erik G Larsson, Thomas L Marzetta, Ove Edfors, and Fredrik Tufvesson. *Scaling up MIMO: Opportunities and challenges with very large arrays*. IEEE signal processing magazine, 30(1):40–60, 2013.

[3] Björn Thors, Anders Furuskär, Davide Colombi, and Christer Törnevik. *Time-averaged realistic maximum power levels for the assessment of radio frequency exposure for 5G radio base stations using massive MIMO*. IEEE Access, 5:19, 2017.

[4] Paolo Baracca, Andreas Weber, Thorsten Wild, and Christophe Grangeat. *A Statistical Approach for RF Exposure Compliance Boundary Assessment in Massive MIMO Systems*. In WSA 2018; 22nd International ITG Workshop on Smart Antennas, pages 1–6. VDE, 2018.

[5] Javier Ferrer Coll, Jose Dolz Martin de Ojeda, Peter Stenumgaard, S Marzal Romeu, and José Chilo. *Industrial indoor environment characterization-Propagation models*. In EMC Europe 2011 York, pages 245–249. IEEE, 2011.

[6] Anders Karstensen, Jesper Ø Nielsen, Patrick Eggers, Elisabeth De Carvalho, Martin Alm, and Gerhard Steinböck. *Dual-User Massive MIMO Measurements at 3.5 GHz with Bi-Directional Angular Discrimination*. In 2018 12th European Conference on Antennas and Propagation (eucap), 2018.

[7] L. Liu, C. Oestges, J. Poutanen, K. Haneda, P. Vainikainen, F. Quitin, F. Tufvesson, and P. D. Doncker. *The COST 2100 MIMO channel model*. IEEE Wireless Communications, 19(6):92–99, December 2012.

[8] Stephan Jaeckel, Leszek Raschkowski, Kai Börner, and Lars Thiele. *QuaDRiGa: A 3-D multi-cell channel model with time evolution for enabling virtual field trials*. IEEE Transactions on Antennas and Propagation, 62(6):3242–3256, 2014.

[9] Xiang Gao, Jose Flordelis, Ghassan Dahman, Fredrik Tufvesson, and Ove Edfors. *Massive MIMO channel modeling-extension of the COST 2100 model*. In Joint NEWCOM/COST Workshop on Wireless Communications (JNCW), 2015.

[10] Alex Oliveras Martinez, Patrick Eggers, and Elisabeth De Carvalho. *Geometry-based stochastic channel models for 5G: Extending key features for massive MIMO*. In Personal, Indoor, and Mobile Radio Communications (PIMRC), 2016 IEEE 27th Annual International Symposium on, pages 1–6. IEEE, 2016.

[11] Kan Zheng, Suling Ou, and Xuefeng Yin. *Massive MIMO channel models: A survey*. International Journal of Antennas and Propagation, 2014, 2014.

[12] Jialai Weng, Xiaoming Tu, Zhihua Lai, Sana Salous, and Jie Zhang. *Indoor massive MIMO channel modelling using ray-launching simulation*. International Journal of Antennas and Propagation, 2014, 2014.

[13] David Loschenbrand, Markus Hofer, and Thomas Zemen. *Ray-Tracer Based Channel Characteristics for Distributed Massive MIMO*. 2017.

[14] Ying Wang, Safieddin Safavi-Naeini, and Sujeet K Chaudhuri. *A hybrid technique based on combining ray tracing and FDTD methods for site-specific modeling of indoor radio wave propagation*. IEEE Transactions on antennas and propagation, 48(5):743–754, 2000.

[15] Paolo Bernardi, Marta Cavagnaro, Stefano Pisa, and Emanuele Piuzzi. *Human exposure to radio base-station antennas in urban environment*. IEEE transactions on microwave theory and techniques, 48(11):1996–2002, 2000.

[16] T Uusitupa, I Laakso, S Ilvonen, and K Nikoskinen. *SAR variation study from 300 to 5000 MHz for 15 voxel models including different postures*. Physics in Medicine & Biology, 55(4):1157, 2010.

[17] Günter Vermeeren, Wout Joseph, and Luc Martens. *Statistical multi-path exposure method for assessing the whole-body SAR in a heterogeneous human body model in a realistic environment*. Bioelectromagnetics, 34(3):240–251, 2013.

[18] Cheng-Xiang Wang, Ji Bian, Jian Sun, Wensheng Zhang, and Minggao Zhang. *A Survey of 5G Channel Measurements and Models*. IEEE Communications Surveys Tutorials, 20(4):3142–3168, 2018.

[19] Greg Durgin, Neal Patwari, and Theodore S Rappaport. *An advanced 3D ray launching method for wireless propagation prediction*. In Vehicular Technology Conference, 1997, IEEE 47th, volume 2, pages 785–789. IEEE, 1997.

[20] GH Spencer and MVRK Murty. *General ray-tracing procedure*. JOSA, 52(6):672–678, 1962.

[21] REMCOM. *Wireless InSite 3.2.0 Reference Manual*. 2017.

[22] J.T. Zhang and Y. Huang. *Investigation of building dielectric properties and the effects on indoor radio channel*. In Twelfth International Conference on Antennas and Propagation, 2003 (ICAP 2003). (Conf. Publ. No. 491), volume 1, pages 207–210 vol.1, 2003.

[23] Georgia E Athanasiadou and Andrew R Nix. *Investigation into the sensitivity of the power predictions of a microcellular ray tracing propagation model*. IEEE transactions on Vehicular Technology, 49(4):1140–1151, 2000.

[24] Daniel Dunbar and Greg Humphreys. *A spatial data structure for fast Poisson-disk sample generation*. ACM Transactions on Graphics (TOG), 25(3):503–508, 2006.

[25] Sergei Shikhantsov, Arno Thielens, Günter Vermeeren, Emmeric Tanghe, Piet Demeester, Luc Martens, Guy Torfs, and Wout Joseph. *Hybrid ray-tracing/FDTD method for human exposure evaluation of a massive MIMO technology in an industrial indoor environment*. IEEE Access, 7:21020–21031, 2019.

[26] Max Born and Emil Wolf. *Principles of optics: electromagnetic theory of propagation, interference and diffraction of light*. Elsevier, 2013.

[27] Ilkka Laakso. *Assessment of the computational uncertainty of temperature rise and SAR in the eyes and brain under far-field exposure from 1 to 10 GHz*. Physics in Medicine & Biology, 54(11):3393, 2009.

[28] Marie-Christine Gosselin, Esra Neufeld, Heidi Moser, Eveline Huber, Silvia Farcito, Livia Gerber, Maria Jedensjö, Isabel Hilber, Fabienne Di Gennaro, Bryn Lloyd, et al. *Development of a new generation of high-resolution anatomical models for medical device evaluation: the Virtual Population 3.0*. Physics in medicine and biology, 59(18):5287, 2014.

[29] Thomas L. Marzetta, Erik G. Larsson, Hong Yang, and Hien Quoc Ngo. *Fundamentals of massive MIMO*. Cambridge University Press, 2016.

[30] Alex Oliveras Martinez, Elisabeth De Carvalho, Jesper Odum Nielsen, and Lishuai Jing. *Frequency dependence of measured massive MIMO channel properties*. In Vehicular Technology Conference (VTC Spring), 2016 IEEE 83rd, pages 1–5. IEEE, 2016.

[31] Xiang Gao, Ove Edfors, Fredrik Rusek, and Fredrik Tufvesson. *Massive MIMO Performance Evaluation Based on Measured Propagation Data.* IEEE Trans. Wireless Communications, 14(7):3899–3911, 2015.

[32] Simon R. Saunders. *Antennas and Propagation for Wireless Communication Systems*. John Wiley & Sons, Inc., New York, NY, USA, 1st edition, 1999.

[33] D. J. Love and R. W. Heath. *Equal gain transmission in multiple-input multiple-output wireless systems*. IEEE Transactions on Communications, 51(7):1102–1110, July 2003.

[34] Si-Nian Jin, Dian-Wu Yue, and Ha H. Nguyen. *Equal-Gain Transmission in Massive MIMO Systems Under Ricean Fading*. IEEE Transactions on Vehicular Technology, 67(10):9656–9668, 2018.

[35] International Commission on Non-Ionizing Radiation Protection et al. *ICNIRP Guidelines for Limiting Exposure To Time-Varying Guidelines for Limiting Exposure To Time-Varying Electric, Magnetic and Electromagnetic fields*. Health Phys, 74:494–522, 1998.

[36] Emmeric Tanghe, Wout Joseph, Leen Verloock, Luc Martens, Henk Capoen, Kobe Van Herwegen, and Wim Vantomme. *The industrial indoor channel: large-scale and temporal fading at 900, 2400, and 5200 MHz*. IEEE Transactions on Wireless Communications, 7(7), 2008.

4 User Body Coupling Effects

4.1 Introduction

Chapter 3 introduced the methodology of estimating human EMF exposure to a large antenna array BS, implementing the massive MIMO equal gain transmission scheme. However, the effect that the variability of the receiver's radiation pattern due to its orientation in space and the effects of the near-field coupling with the user body remained unaccounted for. In this chapter we propose an extension to the established framework that allows to include the aforementioned effect and quantify the impact that it has on the massive MIMO channel and the resulting human exposure.

To the best of the author's knowledge, this chapter for the first time describes the numerical approach that takes both the well-known effects of cluster non-stationarity [1] and user body coupling into account. These effects will be utilized by the Massive MIMO downlink precoding schemes to produce compact space regions of an elevated Electromagnetic field (EMF) around the receiver antennas (hot-spots). Therefore, we apply the proposed approach to calculate the EMF distribution in proximity of a user on a small scale, and use it to estimate the human EMF-exposure. The same method can also be adapted for a 5G near-user antenna design.

4.2 Methods

The proposed approach is based on a hybrid Ray-Tracing (RT) method that is used to model large-scale propagation and the Finite-Difference Time-Domain (FDTD) method, used for refinement of the RT results. In the following sections each step of the approach is discussed in detail and the connection between them is explained.

4.2.1 Ray-Tracing

The RT procedure is described in section 3.2.2 of Chapter 3. In this chapter the same environment model, BS and UEs' parameters as described in section 3.2.2.1 (as shown in Fig. 3.2). Only the NLOS environment configuration, in which the direct path is blocked by a PEC cuboid, will be studied further in this chapter.

For each Tx-Rx pair (n, k) in the simulation, the RT solver returns a collection of rays $\{\mathbf{r}\}_{n,k}$. A ray holds properties of the propagation path it models, such as direction-of-arrival (DoA), time-of-flight (ToF), Path Loss (PL), EMF strength, etc. We use these properties to calculate the wireless channel in Section 4.2.3.

4.2.2 EMF Coupling Effects

This section explains how the radiation pattern of the UE close to a phantom's head is calculated using FDTD simulations.

In realistic scenarios, such as a mobile phone call, a user penetrates the near-field of his UE. This results in EM-coupling which affects the radiation pattern of the UE. We account for this by simulating the UE antenna in a usage mode together with a realistic human body model using FDTD method.

To model the UE antenna, we use a generic half-wavelength dipole antenna model, designed for the central frequency of 3.5 GHz. The overall dipole antenna length is 37 mm, arm diameter and the feed gap are 2 mm. The dipole arms are modeled as perfect electric conductors.

In this chapter we use the same section of the ViP v.3.1 heterogeneous Duke human phantom [2] as in Chapter 3.

The Sim4Life v4.4 (Zürich, Switzerland) software package is used for FDTD simulations throughout this chapter. Fig. 4.1 shows the FDTD computational domain. The antenna is positioned at the center of the global coordinate system and oriented vertically. The phantom's head is positioned near the dipole, such that its bounding box center is coincident with the y-axis and the distance from the left ear to the dipole center is 20 mm. This setup aims to reproduce the effects observed in a real-life phone call scenario, such as signal blockage by the user's head.

The dipole is fed with a sinusoidal signal at 3.5 GHz and 1 W of total input power. The output of the simulation is a complex amplitude of the vertically polarized far-field E-field $\hat{A}(\theta, \phi)$. $\hat{A}(\theta, \phi)$ is sampled on a surface of a 1 m radius

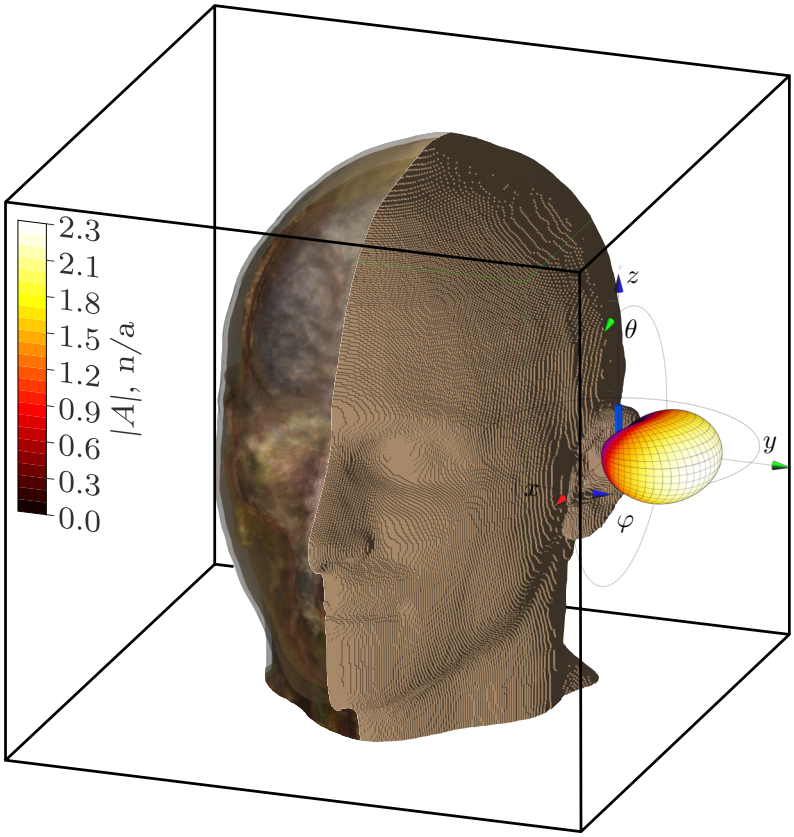

Figure 4.1: The FDTD simulation setup. Solid black lines show the domain boundaries. The original model of ViP v.3.1 Duke phantom's head is presented alongside with its voxelized approximation. The dipole near the phantom's left ear is shown in blue together with its radiation pattern. Global Cartesian and spherical coordinate systems used throughout this chapter are given. The $|A|$ color-bar indicates the magnitude of the normalized radiation pattern $A(\theta, \phi)$ of the dipole coupled with the phantom's head.

sphere for elevation angle θ in range $[0, \pi]$ and azimuth angle φ in range $[0, 2\pi)$ with a 2° step. Its ratio to the far-field E-field strength of an isotropic radiator fed the same input power ($\simeq$7.74 V/m) is the normalized far-field $A(\theta, \phi)$, which will be used throughout the following sections.

The computational domain center is coincident with the center of the phantom's head bounding box and its dimensions are set to 256 mm$\times$256 mm$\times$250 mm. It fully enclosed the head and the antenna, at the same time significantly reducing

the computational demands needed for simulations described in the next section. A maximum discrepancy of around 8% is observed in the antenna directivity if compared to the full-body simulation, which is considered acceptable, taking into account a simplified model of the UE.

4.2.3 Channel Matrix

This section explains how the channel matrix is calculated using rays at the Rx and the radiation pattern from the FDTD simulations.

First, a free-space channel matrix $\mathbf{H}^{fs}$ is constructed from the collection of all rays $\{\mathbf{r}\} = \cup\{\mathbf{r}\}_{n,k}$. A channel between the Tx antenna with index n and the Rx antenna with index k is found as

$$h_{k,n}^{fs} = \sum_{r \in s_{n,k}} \tilde{E}_r^{\theta}, \tag{4.1}$$

and

$$\tilde{E}_r^{\theta} = E_r^{\theta} \exp(-2\pi i f_c \tau_r). \tag{4.2}$$

Here $s_{n,k}$ are the indices of the rays in $\{\mathbf{r}\}_{n,k}$, E_r^{θ} and τ_r are the vertical polarization component of the E-field and the ToF of the r^{th} ray respectively.

Second, a reciprocity of an antenna in transmit-receive is utilized to introduce the DoA dependence into (4.1). As a ray holds the information about its DoA (θ_r, φ_r), by weighting its contribution to the channel in (4.1) with the corresponding radiation pattern value $A(\theta_r, \varphi_r)$, coupling effects are introduced into the channel matrix elements

$$h_{k,n}^{nf} = \sum_{r \in s_{n,k}} A(\theta_r, \varphi_r) \tilde{E}_r^{\theta}. \tag{4.3}$$

For an arbitrary incident direction (θ_r, φ_r), $A(\theta_r, \varphi_r)$ is calculated by the bilinear interpolation of $A(\theta, \varphi)$. Evaluating (4.3) for every Tx-Rx pair, we obtain a full massive MIMO channel matrix $\mathbf{H}^{nf}$.

We calculate the Singular Value Spread (SVS) $\kappa(\mathbf{H})$ of the channel matrix and Matrix Power Ratio (MPR) $\gamma(\mathbf{G})$, given by (3.5), of the channel correlation matrix $\mathbf{G}$ (given by (3.2)) to quantify how the inclusion of the UE radiation pattern into the model affects the channel.

4.2.4 EMF distribution

To determine the EMF distribution in proximity of the user and the UE, FDTD simulation based on the RT results are performed. A ray with index r is modelled as a plane-wave source $\mathbf{p}_r = (\mathbf{k}_r, a_r, \phi_r)$ that spans across the complete computational

domain. It is described by its wave-vector $\mathbf{k}_r$, amplitude a_r and phase delay at the domain center ϕ_r.

To reduce the required computational resources, DoAs of the rays in $\mathbf{r}$ are substituted by the outer normal vectors of the faces of an icosahedral sphere (ico-sphere) $\{\mathbf{n}_{ico}(m)\}$ [3], with m being the ico-sphere frequency. The wave-vector of a plane wave that corresponds to the i^{th} face of the ico-sphere is then the inner normal of that face

$$\mathbf{k}_i = -\mathbf{n}_{ico,i}. \tag{4.4}$$

The amplitude and phase of the plane wave with index i are obtained by taking a sum of the complex amplitudes of the rays, DoAs of which have the smallest angular distance to the i^{th} ico-sphere outer normal. Each ray's amplitude is weighted with the *precoding matrix* element $w_{n,k}$, where (n, k) is the Tx-Rx pair indices for which the ray is calculated.

In this chapter we investigate the Maximum Ratio Transmission (MRT) precoding scheme [4]. MRT matrix $\mathbf{W}$ is proportional to the complex conjugate transpose of the channel matrix and its elements are given by

$$w_{n,k} = \alpha h^*_{k,n}, \tag{4.5}$$

where the normalization coefficient α is chosen such that $\mathbf{W}$ has unit Frobenius norm.

The amplitude and phase of the plane wave with index i at the Rx with index k is then given by the magnitude and argument respectively of

$$p_{i,k} = \sum_{n=1}^{N} w_{n,k} \sum_{r \in s_{n,k}} \tilde{E}^{\theta}_r. \tag{4.6}$$

Here the outer sum is taken over the BS elements, with N being their overall number.

Using (4.5) to calculate the precoding with (4.3) as the channel matrix, we obtain a set of the plane wave sources that models the EMF incidence at a massive MIMO user

$$p^{nf}_{i,k} = \alpha \sum_{n=1}^{N} \sum_{r \in s_{n,k}} (h^{nf}_{k,n})^* \tilde{E}^{\theta}_r. \tag{4.7}$$

4.2.5 FDTD setup

One FDTD simulation is required for each user in the environment. The result of a simulation is a 3-dimensional distribution of the electromagnetic field in free-space around the phantom and inside its tissues. Knowing the dielectric properties of

the phantom's tissues we are able to calculate its EMF-exposure in terms of the Specific Absorption Rate (SAR). We use the peak-spatial SAR averaged over a 10-g cube (psSAR_{10g}), calculated according to the IEEE/IEC 62704-1 standard [5]. psSAR_{10g} captures local exposure peaks, that highly-focused fields distinctive to the massive MIMO technology, are expected to produce.

As explained in Chapter 1, the International Comission on Non-Ionizing Radiation (ICNIRP) specifies basic restrictions for psSAR_{10g} below 6 GHz [6] in the head for the general public (2 W/kg) and workers (10 W/kg). Based on these limits, reference levels on time-averaged power density are established using FDTD simulations with a single incident plane wave (10 W/m^2 and 50 W/m^2 for the general public and workers respectively). We will compare massive MIMO exposure and free-space power density with the ICNIRP guidelines in the following section.

A more detailed description of the FDTD simulation setup, its sensitivity and error analysis are given in Chapter 3 (see also [7]).

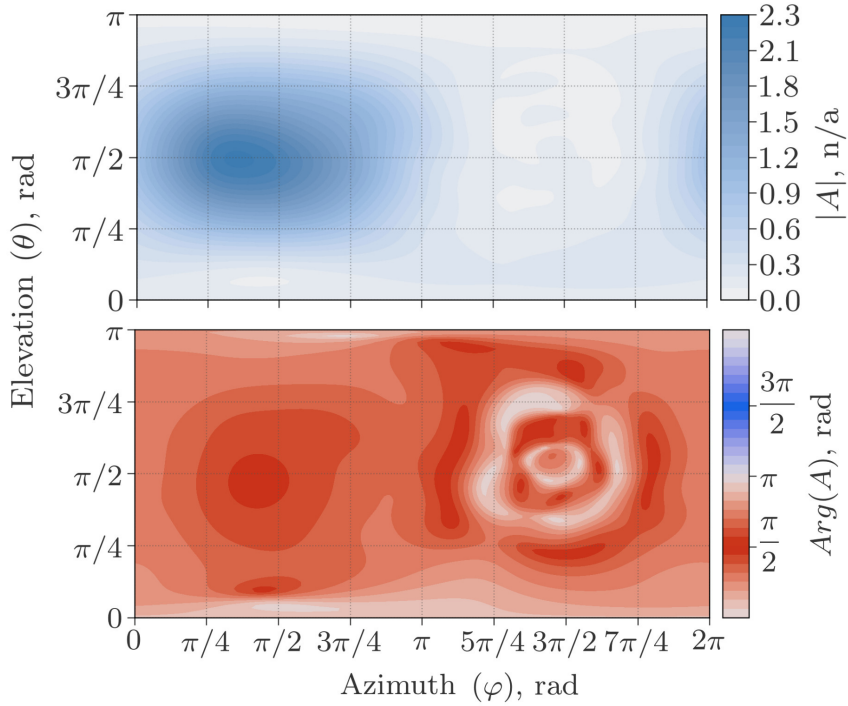

Figure 4.2: Radiation pattern of the dipole antenna coupled with the phantom's head. Top: Amplitude. Bottom: Phase.

4.3 Results

In this section, the results are given in the order of the subsections of the previous section.

4.3.1 Far-Field Pattern

The normalized radiation pattern $A(\theta, \varphi)$ is calculated as described in Section 4.2.2. Fig. 4.2 shows its magnitude and phase in spherical coordinates. Azimuth angle $\varphi = \pi/2$ corresponds to the incident radiation that is not obstructed by the user's head (see the coordinate system at Fig. 4.1).

A global maximum of $|A|$ is observed around this azimuth angle in the horizontal plane ($\theta = \pi/2$). This is expected, as the UE dipole is vertically oriented, it favours propagation in the horizontal plane. The phase response shown at the bottom of Fig. 4.2 is relatively flat around the magnitude maximum, varying for no more than $\pi/4$ in the $\pi/2$ neighbourhood of $(\theta = \pi/2, \varphi = \pi/2)$.

A global minimum of A magnitude is found near $\phi = 3\pi/2$. This is also expected, as at these angles the incident radiation is attenuated by the user's head. The amount of attenuation is significant; it reaches around -18 dB (a factor of 63) if compared to the global maximum.

The phase of A oscillates rapidly around $\phi = 3\pi/2$. This can be explained by a superposition of multiple diffraction paths that become dominant when the LOS is blocked by the head. However, this rapid phase variation does not make any noticeable contribution to the channel due to a low relative power of the propagation paths associated with it.

4.3.2 Channel correlation matrix

100 environment samples are simulated using the RT as described in Section 3.2.2.1.

First, a free-space channel correlation matrix $\mathbf{G}^{fs}$ is calculated. This is done by evaluating (3.2) with $\mathbf{H}$ given by (4.1) for rays traced in each environment sample. At the top of Fig. 4.3 the magnitude of a sample average of $\mathbf{G}^{fs}$ is shown.

Second, the channel correlation matrix $\mathbf{G}^{nf}$, that accounts for the UE radiation pattern is calculated. For each UE in the environment, the radiation pattern $A(\theta, \varphi)$ (Section 4.2.2) is rotated around the z-axis to an angle sampled randomly in $[0, 2\pi)$. This models a random positioning of users with respect to the BS, when all user orientation directions are equally probable. The average $\mathbf{G}^{nf}$ taken over all 100 environment samples is shown at the bottom of Fig. 4.3.

The diagonal elements of $\mathbf{G}$ are proportional to the power received in the downlink (DL) by users, if the MRT precoding is applied. Both $\mathbf{G}^{fs}$ and $\mathbf{G}^{nf}$ are diagonally dominant. This means that a significant portion of the DL transmitted power reaches the intended receiver. However, in case of $\mathbf{G}^{fs}$ there is an apparent

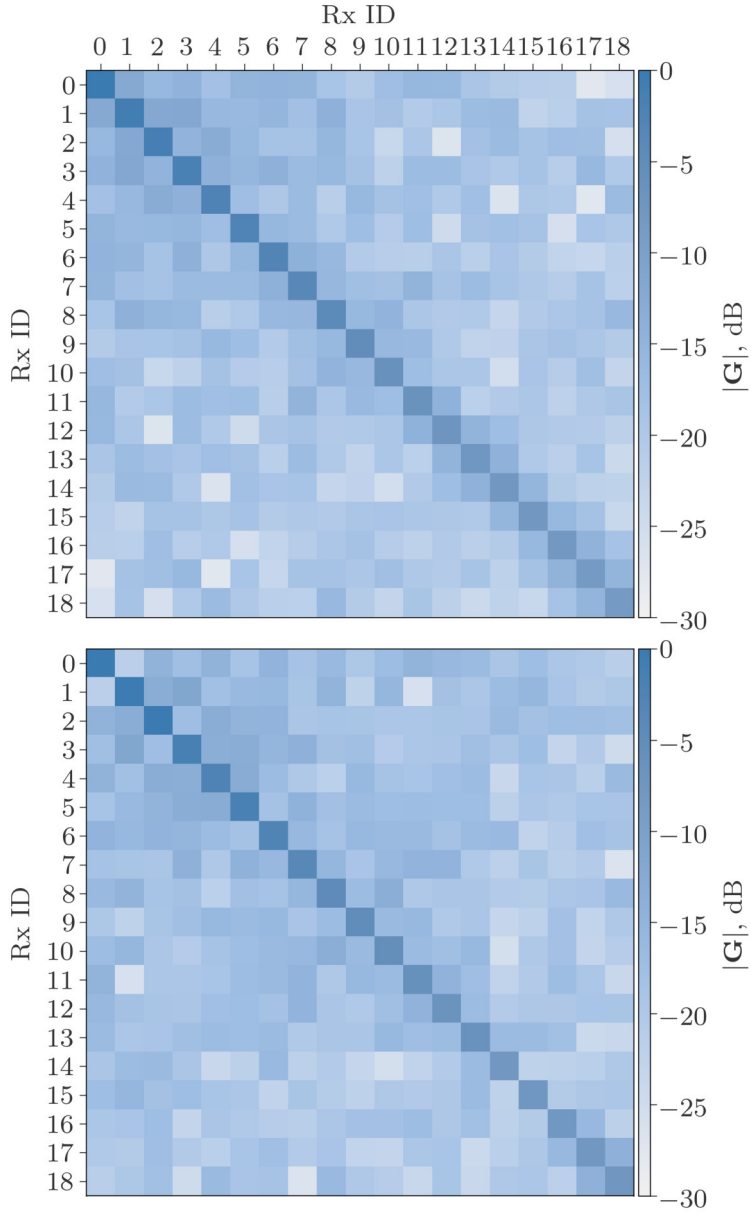

Figure 4.3: Normalized channel correlation matrix averaged over 100 environment samples (logarithmic scale). Top: Free space channel $\mathbf{H}^{fs}$. Bottom: Channel with the coupling effects $\mathbf{H}^{nf}$.

increase in a relative magnitude of the super- and sub-diagonal elements. This corresponds to the increased interference of users with their closest neighbors in the simulated environment. Such effect is not observed in $\mathbf{G}^{nf}$. An average ratio between the elements on the sub-diagonal (or super-diagonal) and the diagonal elements is around 12% for $\mathbf{G}^{fs}$ and less that 8% for $\mathbf{G}^{nf}$.

This difference in the channel correlation (around 30% decrease) can be explained by a highly correlated incident field, viewed as a function of DoA between closely separated locations. Presence of a highly-directional individual radiation patterns helps to resolve users that do not have enough spatial separation, which will have a positive effect on a massive MIMO system performance. For instance, it is likely that the propagation paths are similar for the adjacent UEs due to the presence of shared reflection and diffraction clusters. Therefore, any two adjacent UEs with omnidirectional antennas receive to a high degree correlated total signal, as seen from a relatively high magnitude of the sub-diagonal elements in Fig. 4.3 (Top). At the same time, the propagation paths in either half of the environment (with respect to the y-axis) are statistically independent (by construction). This property can be beneficial for UEs with directional antennas, as the one shown in Fig. 4.1. Considering an extreme case, if any two adjacent UEs patterns are pointing in the opposite y-axis directions, they on average receive less correlated signal, compared to the UEs with omnidirectional antennas, by effectively "filtering out" shared propagation paths.

To study statistical properties of the channels, we calculate the MPR and SVS for different numbers of active UEs in the environment and Tx elements used at the BS. First, two and five UEs are selected randomly from the full simulated set and channel matrices (4.1) and (4.3) are calculated with only those UEs (index k) and a full 36-element array at the BS. Second, the same calculation is performed with five and ten randomly selected BS antenna elements and five randomly selected UEs. This is repeated 100 times in 100 environment samples, resulting in 10^4 samples per dataset. Additionally, $\kappa(\mathbf{H})$ and $\gamma(\mathbf{G})$ of the full channel (19 UEs) are calculated.

Fig. 4.4a depicts histograms of $\kappa(\mathbf{H})$ and $\gamma(\mathbf{G})$ for 2, 5 and 19 (all) UEs (as shown in Fig. 3.2) in black, blue and red, respectively. As the number of users in the channel increases, MPR (left column) decreases for both $\mathbf{G}^{fs}$ (top) and $\mathbf{G}^{nf}$ (bottom). This is in line with definition (3.5), as the number of the off-diagonal elements of a square matrix is roughly proportional to the square of the number of its diagonal elements. However, $\gamma(\mathbf{G}^{nf})$ has a larger positive skew and average values compared to $\gamma(\mathbf{G}^{fs})$. Higher $\gamma(\mathbf{G})$ corresponds to channels with less correlation between UEs, being unity for purely orthogonal channels (with the correlation matrix $\mathbf{G}$ being diagonal). This means that the near-field user-UE coupling decreases (on average) correlation between massive MIMO users.

The right column in Fig. 4.4a shows $\kappa(\mathbf{H})$ (in dB) for $\mathbf{G}^{fs}$ (top) and $\mathbf{G}^{nf}$ (bottom). For both $\mathbf{G}^{fs}$ (top) and $\mathbf{G}^{nf}$ larger user count yields larger SVS values.

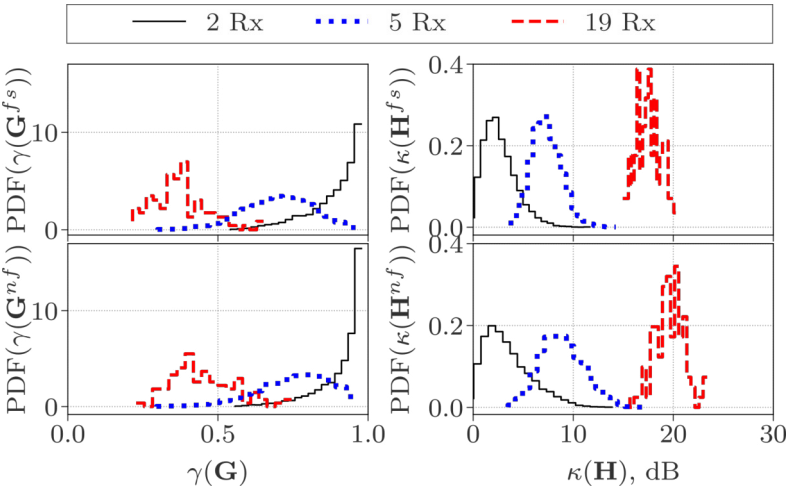

(a) Distributions for 2 and 5 randomly selected UEs, and all 19 UEs are shown with black, blue, and red respectively. All 36 Tx elements are used.

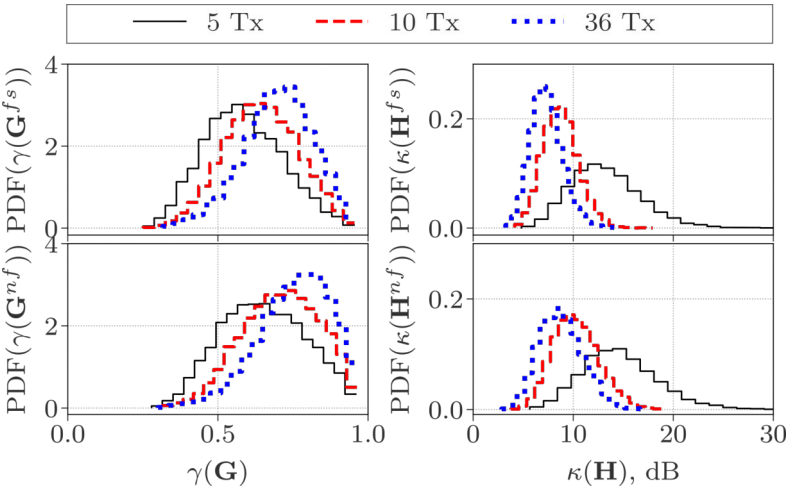

(b) Distributions for 4 and 9 randomly selected Tx elements, and all 36 Tx elements are shown with black, red, and blue respectively. 5 UEs are randomly selected in each channel evaluation.

Figure 4.4: Matrix Power Ratio $\gamma(\mathbf{G})$ (left column) and Singular Value Spread $\kappa(\mathbf{H})$ (right column) empirical distributions of 100 environment sample channels. In each sub-figure free-space channels (top rows) and channels with the coupling effects (bottom rows) are shown.

This is expected, as $\kappa(\mathbf{H})$ is determined by only two most correlated rows of $\mathbf{G}$. The more UEs are included in the channel (the greater $\dim(\mathbf{G})$ is), the higher chance there is for any two users to have correlated channels.

Fig. 4.4b presents histograms of $\kappa(\mathbf{H})$ and $\gamma(\mathbf{G})$ for a fixed number of 5 UEs and a varying number of the BS antenna elements. With an increase of the element count, the mean of $\gamma(\mathbf{G})$ monotonically grows for both $\mathbf{G}^{fs}$ and $\mathbf{G}^{nf}$. The mean of $\gamma(\mathbf{G}^{nf})$ remains larger than $\gamma(\mathbf{G}^{fs})$ for all (equal) studies BS antenna counts.

Increasing the number of the BS antennas leads to a decrease of $\kappa(\mathbf{H})$, as shown in the right column of Fig. 4.4b. Moreover, the amount of $\kappa(\mathbf{H})$ variation strongly depends on the ratio N/K between the number of the BS antennas and the UEs. Increasing N from 5 to 10 (N/K from 1 to 2) leads to around 6 dB (4 times) decrease of mean values of both $\kappa(\mathbf{H}^{nf})$ and $\kappa(\mathbf{H}^{fs})$. Increasing N from 10 to 36 (N/K from 2 to 6.2) decreases the mean value of $\kappa(\mathbf{H}^{fs})$ around 1 dB. This observation agrees well with the results of measurements in NLOS conditions [8].

Mean values of the histograms shown at Fig. 4.4 are compiled in Table 4.1. In summary, the near-field coupling leads to the increase in the average of both $\gamma(\mathbf{G})$ and $\kappa\mathbf{H}$.

#Tx/#Rx	$\gamma(\mathbf{G}^{fs})$	$\gamma(\mathbf{G}^{nf})$	$\kappa(\mathbf{H}^{fs})$	$\kappa(\mathbf{H}^{nf})$
36/2	0.92	0.97	3.3 dB	3.8 dB
36/5	0.73	0.79	7.1 dB	9.8 dB
36/19	0.33	0.45	18.1 dB	20.7 dB
5/5	0.62	0.68	14.5 dB	16.1 dB
10/5	0.68	0.74	9.5 dB	9.6 dB

Table 4.1: Mean values of $\kappa(\mathbf{H})$ and $\gamma(\mathbf{G})$ for different combinations of active Tx and Rx antenna counts.

4.3.3 Hot-spot

In this section we present the results of the FDTD simulations described in Section 4.2.4.

We perform FDTD simulations for all UEs in 10 environment samples. To evaluate the focusing of the EMF in proximity of the UE antenna we calculate the time-averaged Poynting vector at the receiver k as

$$\mathbf{S}_k = \mathrm{Re}(\frac{\mathbf{E}_k \times \mathbf{H}_k^*}{2}), \tag{4.8}$$

where electric and magnetic field vectors $\mathbf{E}_k$ and $\mathbf{H}_k$ are interpolated on a rectilinear grid. A horizontal slice coincident with the phantom's head center ($z = 0$) of $\|\mathbf{S}_k\|$, averaged over all 19 UEs in 10 environment samples is shown at Fig. 4.5.

A strong focusing of $\|\mathbf{S}_k\|$ is present near the dipole center, shown with a black circle in Fig. 4.5. This is the compound effect of the MRT precoding and the propagation environment. The precoding forces the signals from different BS

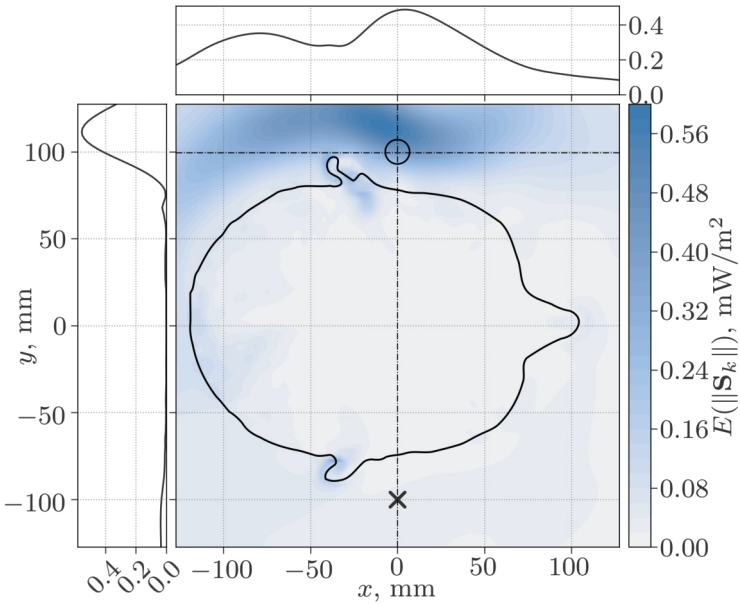

Figure 4.5: Magnitude of the time-averaged Poynting vector distribution. Slice in the horizontal plane ($z = 0$) shows the average of 19 user locations in 10 environment samples.

elements to arrive coherently at the antenna terminal and a sufficiently diverse environment makes it very unlikely for them to be in-phase at any other point in space.

To quantify the focusing effect we calculate the ratio between time-averaged power density at the antenna center $\mathbf{r}_{Rx} = (0, 100, 0)$ (shown with a circle) and $\mathbf{r}_{sym} = (0, -100, 0)$ that is symmetric to it with respect to the xz-plane (marked with a black cross at Fig. 4.5)

$$S_k = \frac{\|\mathbf{S}_k(\mathbf{r}_{Rx})\|}{\|\mathbf{S}_k(\mathbf{r}_{sym})\|}. \tag{4.9}$$

As both the environment model and the phantom body are symmetric with respect to the xz-plane, it is reasonable to assume that for DL transmission with no precoding, the average of S_k would be 1.

Fig. 4.6 shows a histogram of S_k (dB scale). Average S_k is around 10 dB, and 5^{th} - 95^{th} percentile range spans from just above 3 to slightly over 16 dB. This means that that the average hot-spot values of the power flux density are 10 times higher than in the surrounding space.

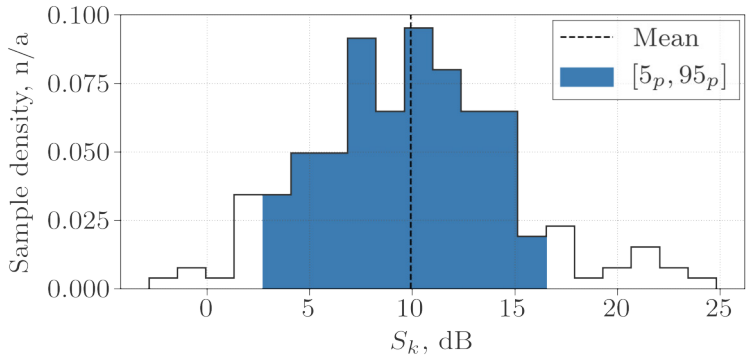

Figure 4.6: Sample density of left/right time-averaged Poynting vector gain.

4.3.4 Specific Absorption Rate

The psSAR_{10g} is calculated in the phantom's head using built-in algorithms available in the Sim4Life software. We evaluate SAR_{10g} in the same environment samples and UE locations as were analyzed in Section 4.3.3, resulting in 190 overall number of exposure samples. Fig. 4.7 depicts SAR_{10g} distribution in the horizontal slice at $z = 0$ and projections of the peak-cubes on that plane.

The largest portion of the peak-cubes ($\simeq$78%) is found near the left ear (see Fig. 4.7, red circle). These exposure peaks are produced by the EMF hot-spot at the UE antenna, located close to the ear.

In contrast to that, only around 9% of all peak-cubes is found at the right ear (indicated with the green circle at Fig. 4.7). These peak-cubes are spatially more concentrated than the cubes at the left ear, which suggests that they are mainly caused by the ear geometry. High curvature of the ear tends to concentrate EMF in the surrounding tissues even if exposed to a plane-wave [9]. This effect can be observed in Fig. 4.5 by noting the in-tissue local maximas of the power flux density. The most of the remaining peak-cubes are located at the back of the head, in the direction to the BS. In three samples the psSAR_{10g} is found in the eyes. This allows to conclude that most of the Massive MIMO DL exposure is produced in the vicinity of the UE.

To perform the exposure analysis, we introduce η - the psSAR_{10g} normalized to the time-averaged Poynting vector magnitude

$$\eta = \frac{\text{psSAR}_{10g}}{\mathbf{S}}. \tag{4.10}$$

The normalized exposure aids the analysis in two aspects. First, the influence of the BS transmit power and the PL is eliminated. Thus, values that are assessed

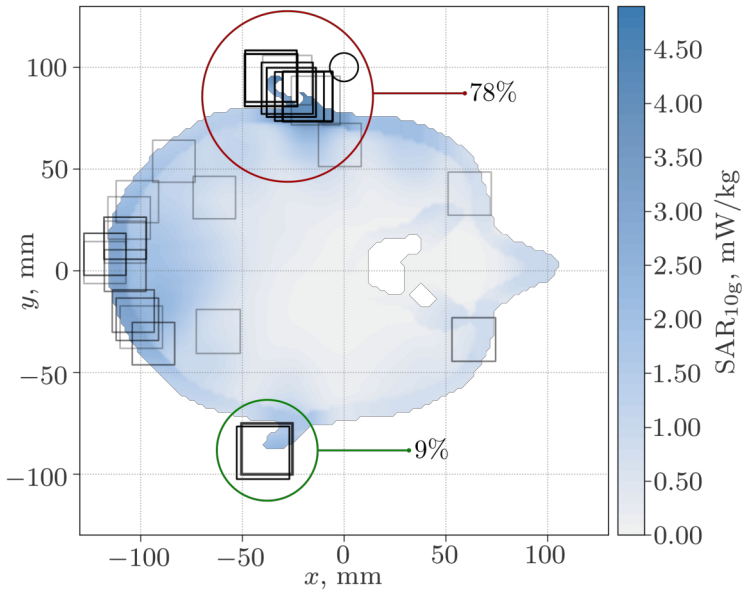

1

Figure 4.7: psSAR$_{10g}$ and peak-cubes in the phantom's head. Slice in the horizontal plane ($z = 0$) shows the average of 19 user locations in 10 environment samples.

at the UEs located at different distances to the BS can be correctly compared. Second, η indicates how adequate the existing safety regulatory limits are. Current regulations require the EMF measured in free-space to comply with a predefined threshold (reference levels). The threshold value is established based on the results of extensive direct measurements, simulations and additional safety factors, in which conventional single-antenna transmitters are used.

The definition of η depends on the location and conditions at which the EMF is assessed for normalization. Two normalization strategies are compared. First, η_{hs} is calculated as psSAR$_{10g}$ normalized to the maximum $\|\mathbf{S}_k\|$ in the domain (hot-spot normalization). This is the time-averaged power flux density, that would occur close to the UE in operation.

Second, η_{pw} is calculated by normalizing psSAR$_{10g}$ to the average of the power flux densities in the incident plane-wave sources defined in (4.6). This is the value that would be observed in free-space when no user is present, as currently followed by the ICNIRP exposure guidelines [6].

As a reference we use $\eta_{ref} = 0.2$ m^2/kg, calculated from the ICNIRP general public restrictions (psSAR$_{10g}^{ICNIRP} = 2$ W/kg, $\|\mathbf{S}\|^{ICNIRP} = 10$ W/m^2).

Fig. 4.8 depicts mean values and 5$^{\text{th}}$ - 95$^{\text{th}}$ percentiles of η_{hs} and η_{pw} calculated for 190 exposure samples, plotted versus the distance to the BS. For all studied

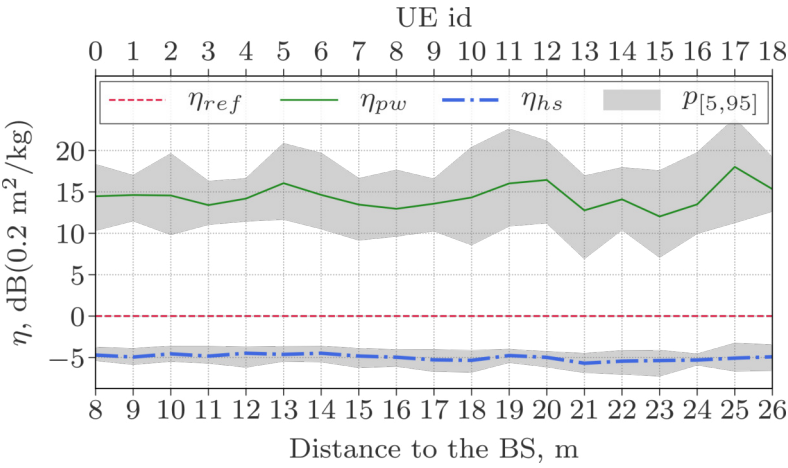

Figure 4.8: psSAR$_{10g}$ normalized to the time-averaged Poynting vector (dB scale). η_{hs} (blue) - normalization using values at the hot-spot. η_{pw} (green) - normalization with the average of the incident plane waves. For all UE locations η_{hs} is lower and η_{pw} is higher than the value calculated from the ICNIRP basic restrictions (used for the dB reference).

distances η_{hs} is nearly constant and around 3 times lower than η_{ref}. It also had a relatively low variance: 90% of all samples fell between -3 and -7 dB. Additionally, psSAR$_{10g}$ is highly correlated with the hot-spot power flux density (Pearson correlation coefficient $\rho = 0.96$). This is in agreement with the analysis of the peak-cube locations: most of the exposure is observed near the hot-spot. Hence, power flux density close to the receiver could be used to estimate the EMF-exposure. In addition, applying existing reference levels would overestimate psSAR$_{10g}$ at least by a factor of 2.

In contrast, the average η_{pw} is about 15 dB higher than η_{ref} and has larger sample variation compared to η_{hs}. This indicates that free space EMF measurements cannot reliably estimate the massive MIMO exposure. The existing free-space reference levels underestimate psSAR$_{10g}$ by a factor ranging from 10 to 100.

Finally, a comparison with the results obtained in Chapter 3 can be made. The average psSAR$_{10g}$ normalized to the free space hot-spot power flux density η_{fs} (see Fig. 3.8) is calculated by evaluating (4.10) with the psSAR$_{10g}$ and $\mathbf{S}$ values show in Fig. 3.10b (the NLOS scenario), for the head rotated at 0° and 90°. In Fig. 4.9, $\eta_{fs}(0^\circ)$ and $\eta_{fs}(90^\circ)$ sample-average values are shown with solid blue and green lines, respectively, while their 5$^{\text{th}}$to 95$^{\text{th}}$percentile ranges are marked with shaded regions of matching colors. For all BS to UE separation distances $\eta_{fs}(0^\circ)$ is (up to 3dB) lower than $\eta_{fs}(90^\circ)$, which results from the lower psSAR$_{10g}$ levels in the head exposed predominantly from the back, as can be seen in Fig. 3.10b

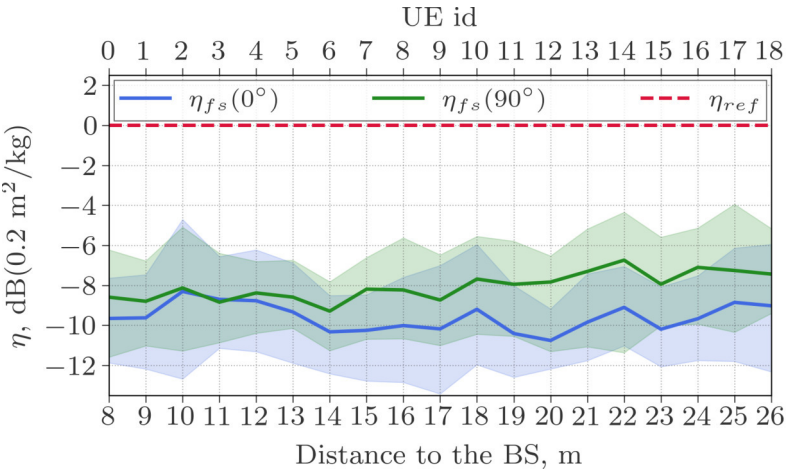

Figure 4.9: psSAR$_{10g}$ normalized to the time-averaged Poynting vector assessed in free space (Chapter 3). $\eta_{fs}(0°)$ (blue) - incidence from the back of the head; $\eta_{fs}(90°)$ (green) - incidence from the side.

(bottom). On average, η_{fs} is below η_{hs} (Fig. 4.8) by around 3 dB to 5 dB. This means that failing to account for the UE-to-head coupling effects when estimating the massive MIMO channel and forming the transmit vector underestimates the induced psSAR$_{10g}$ by at leas a factor of 2. Such noticeable discrepancy can be explained by the disruption of the EMF focused in free space by the head, which is apparent when comparing the peak-cube distributions in Fig. 3.9 and Fig. 4.7. This result, once again, underlines the importance of accounting for the antenna coupling with the human body when assessing the downlink massive MIMO exposure.

4.4 Conclusions

A novel numerical approach to massive MIMO channel modeling based on the RT and the FDTD methods was presented. For the first time, to the authors' knowledge, massive MIMO channels were simulated with the effects of near-field coupling between the receiver antenna and the user body. The importance of this effect was studied with models of a generic dipole antenna, a realistic human phantom and an industrial indoor environment. It was shown that including the coupling effects decreases correlation between closely spaced UEs by around 30%. The time-averaged Poynting vector magnitude enhancement at the UE was around 10 dB. The psSAR$_{10g}$ in the phantom's head was found to be directly proportional to the hot-spot power flux density. Normalized psSAR$_{10g}$ complies with the ICNIRP guidelines, but assessing the reference levels in free space (with no active receiver) would lead to its underestimation by at least a factor of 10.

Although the presented study was carried out at a sub-6 GHz frequency, the same approach can be applied to a mm-Wave system analysis. The RT method is more accurate at higher frequencies with no performance loss. The FDTD memory grows as the third power, and time as the first power of frequency, which can limit the overall performance.

In Chapter 5 we will study the exposure to a distributed massive MIMO BS in a larger indoor industrial environment. The influence of the UE position relative to the phantom's head on the hot-spot size, position, and the exposure it induces, will be investigated. Comparison with the ATTO-cell technology studied in Chapter 2 will be made.

References

[1] Jose Flordelis, Xuhong Li, Ove Edfors, and Fredrik Tufvesson. *Massive MIMO Extensions to the COST 2100 Channel Model: Modeling and Validation*. arXiv preprint arXiv:1905.04931, 2019.

[2] Marie-Christine Gosselin, Esra Neufeld, Heidi Moser, Eveline Huber, Silvia Farcito, Livia Gerber, Maria Jedensjö, Isabel Hilber, Fabienne Di Gennaro, Bryn Lloyd, et al. *Development of a new generation of high-resolution anatomical models for medical device evaluation: the Virtual Population 3.0*. Physics in medicine and biology, 59(18):5287, 2014.

[3] John R Baumgardner and Paul O Frederickson. *Icosahedral discretization of the two-sphere*. SIAM Journal on Numerical Analysis, 22(6):1107–1115, 1985.

[4] Thomas L. Marzetta, Erik G. Larsson, Hong Yang, and Hien Quoc Ngo. *Fundamentals of massive MIMO*. Cambridge University Press, 2016.

[5] *IEC/IEEE P62704-1/D2, October 2013: IEC/IEEE Draft Standard for Determining the Peak Spatial Average Specific Absorption Rate (SAR) in the Human Body from Wireless Communications Devices, 30 MHz - 6 GHz. Part 1: General Requirements for Using the Finite Di*. IEEE, 2013.

[6] International Commission on Non-Ionizing Radiation Protection et al. *ICNIRP Guidelines for Limiting Exposure To Time-Varying Guidelines for Limiting Exposure To Time-Varying Electric, Magnetic and Electromagnetic fields*. Health Phys, 74:494–522, 1998.

[7] Sergei Shikhantsov, Arno Thielens, Günter Vermeeren, Emmeric Tanghe, Piet Demeester, Luc Martens, Guy Torfs, and Wout Joseph. *Hybrid ray-tracing/FDTD method for human exposure evaluation of a massive MIMO technology in an industrial indoor environment*. IEEE Access, 7:21020–21031, 2019.

[8] Xiang Gao, Ove Edfors, Fredrik Rusek, and Fredrik Tufvesson. *Massive MIMO Performance Evaluation Based on Measured Propagation Data.* IEEE Trans. Wireless Communications, 14(7):3899–3911, 2015.

[9] T Uusitupa, I Laakso, S Ilvonen, and K Nikoskinen. *SAR variation study from 300 to 5000 MHz for 15 voxel models including different postures*. Physics in Medicine & Biology, 55(4):1157, 2010.

5

RF-EMF Downlink Distributed Massive MIMO

5.1 Introduction

Chapters 3 and 4 introduced a method to assess the human exposure in a massive MIMO hot-spot and applied it to an indoor environment with a compact ($\lambda/2$ inter-element distance) BS array. As mentioned in Chapter 1, such 5G New Radio (NR) BSs are already being deployed across the world. In addition, as of the latest release of the 3rd Generation Partnership Project (3GPP), it is planned to augment the existing cellular cites with large array 5G-NR BSs [1] to facilitate a gradual transition of the cellular traffic towards 5G. We also stressed in Sections 3.3.1 and 4.3.2 the importance of having strong reflections in the environment for the massive MIMO performance. *Favorable propagation conditions*, resulting from e.g., rich multipath propagation, are assumed and relied upon to multiplex UEs with no need for computationally-intensive interference cancellation techniques [2]. Under these assumptions, a massive number of the BS antennas transmit to multiple UEs through uncorrelated spatially separated streams.

However, it was shown that in some cases, e.g., strong line-of-sight (LOS) components in channels of closely-spaced UEs, favorable propagation does not occur [2, 3], if the BS is sufficiently compact in size. Indeed, by comparing Fig. 3.6b and Fig. 3.6c in Section 3.3.1, it is clear that the latter (LOS scenario) results in a significantly more correlated channel vectors. In addition, intra- and inter-cell channel correlation of the UEs that share pilot signals, causes *pilot*

contamination [4] which hinders the system performance, and eventually limits the theoretically achievable data-rates [5].

Several architectural improvements to massive MIMO were proposed to solve these problems. In Distributed massive MIMO [6, 7] (DMaMIMO), a distributed collection of neighboring remote radio nodes cooperatively and coherently serves the receiver nodes in an opportunistic manner. The radio nodes dynamically form arrays to optimize their beam-forming capacity. A similar concept of cell-free massive MIMO was independently proposed in [8, 9]. It was shown theoretically that access points (APs) spread out randomly in the environment and transmitting coherently deliver an almost 20 times higher per-user throughput compared to a 'small-cell' system in which UEs are connected only to a single AP. In [10, 11], Radio Stripes - a concept hardware implementation enabling massive distributed antenna systems was presented and discussed.

These concepts, are unified in [12] under the Extremely Large Aperture Arrays (ELAA) paradigm. The ELAA encompasses any massive antenna array (structured or unstructured) distributed over a much larger area, compared to the size of a traditional BS, e.g., a building facade outdoors or a ceiling surface indoors. The large physical size of such arrays increases their spatial focusing resolution, compared to a compact array with equal antenna element count, and effectively puts served UEs in its near field region, if the entire array is treated as one electrically coherent structure.

This common feature of distributed networks is also expected to have an immense impact on the interaction of the user's body with the electromagnetic field (EMF) radiated in the down-link (DL). In scenarios involving a collocated BS, signals reaching a UE in far-field often have a dominant direction of arrival (DoA), determined by the relative location of the BS. This may result in the UE being largely shadowed by the user body from the incident EMF. In such situations, the BS array capable of dynamically adjusting its transmission, is either forced to utilize the reflected paths in the environment, or increase its transmit power to ensure a sufficient signal-to-noise ratio (SNR). The latter inevitably leads to the increase of the EMF power dissipated in the user body blocking the UE device.

A distributed massive MIMO system has higher chance of having multiple unobstructed paths to diverse scenarios of user-UE mutual placement, allowing for a more optimal resource allocation in the DL inducing lower exposure of the users. In this chapter, for the first time to our best knowledge, we present a numerical study of the human EMF exposure to the DL transmission of a distributed massive antenna array BS. The numerical approach developed in Chapters 3 and 4, which combines the propagation modeling with the RT method with the FDTD-based exposure evaluation of a realistic human phantom, is applied in new industrial environments. Scenarios with distributed and collocated BSs are directly compared in cases with and without the UE device blockage by the phantom's head. The

reported insights are valuable for exposure-aware next generation wireless network planning, optimization and standardization of the experimental exposure assessment procedures in such networks.

5.2 Methods

In this chapter we apply the method described in Chapters 3 and 4, with modifications improving its computational performance, but not altering the general structure. This section describes the new modeling aspects and gives references to the previous chapters whenever possible. A new environment model is studied, as described in the following section.

5.2.1 Environment model

The parameters of the RT solver are given in Table 3.1. The geometry of the new floorplan is structurally similar to the one described in Chapters 3 and 4, but has a larger size to allow for a more diverse BS-UE mutual positioning. Fig. 5.1 shows the new model of an indoor industrial environment consists of a cuboid floorplan with smaller cuboid scatterers distributed within it. The floorplan has dimensions of 100 m×100 m×10 m. Dielectric properties of a concrete material at 3.5 GHz ($\varepsilon_r = 7,\ \sigma = 1.5 \cdot 10^{-2}$ S/m) were assigned to its floor, ceiling and walls [13]. The scatterers have a fixed dimensions of 2.5 m×1.25 m in x and y directions, respectively, and each scatterer height is selected independently from a uniform random distribution from 3 m to 7 m. The scatterers are positioned on a uniform rectilinear grid with a step of 5 m in both x and y, and after that 30% of them is removed via random selection, resulting in 87.5% of the free floor surface. Each of the remaining scatterers is then rotated at a random angle around the z-axis and assigned perfect electric conductor (PEC) material properties. The cuboid scatterers can be viewed as simplified models of a heavy industrial machinery or mobile robotic equipment (factories of the future setting), or metal storage racks (warehouse setting), that were placed without the knowledge of the potential APs locations.

All transmitter (Tx) antenna elements were assigned isotropic vertically-polarized (parallel to the z-axis) radiation patterns at $f_c = 3.5$ GHz central frequency ($\lambda \simeq 86$ mm) Two BS configurations were considered. The collocated BS is modeled with a 10-by-10 planar rectangular array of uniform half-wavelength (λ) inter-element spacing. The array surface is normal to the z-axis and its center was set at the center of the floorplan at $z = 9$ m, as indicated in Fig. 5.1. The distributed BS has identical parameters, except for the inter-element spacing, which was set to 10 m to uniformly cover the floorplan ceiling leaving a 5 m distance from any side-wall.

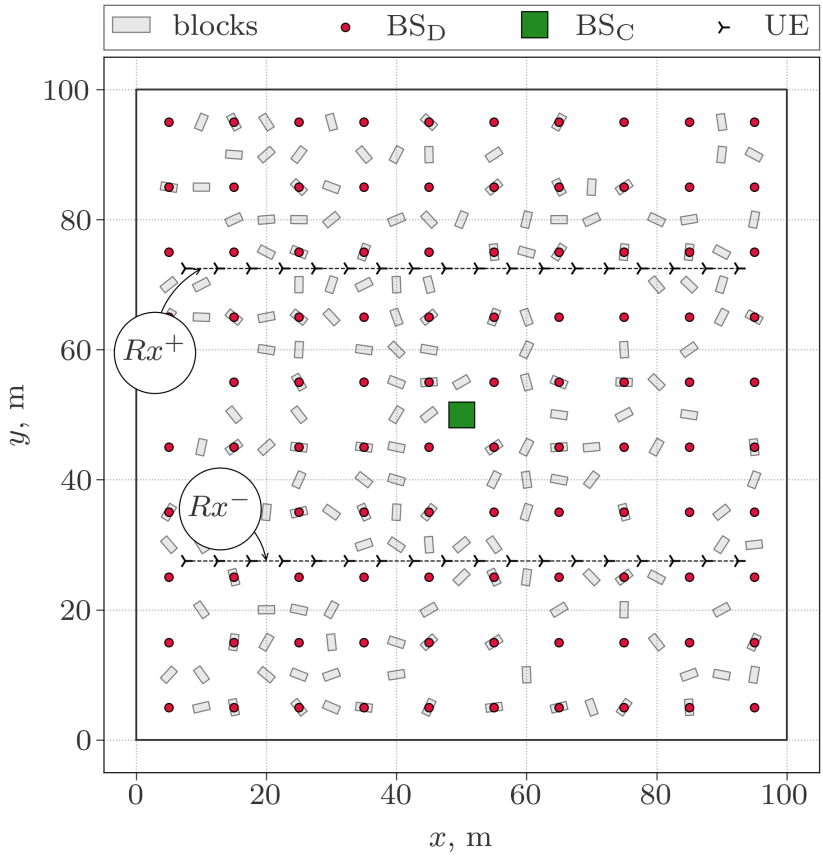

Figure 5.1: The top view of the RT environment sample. The collocated (BS_C) and distributed (BS_D) Tx elements are drawn with the green square and red circles, respectively. The grey rectangles show the outlines of the cuboid scatterers. The UE tracks $Rx^{+,-}$ are shown with black dashed lines, upon which the UE locations are marked with arrowheads, indicating the positive direction of the x-axis in the FDTD domain.

The receiver (Rx) positions form straight lines (tracks), crossing the floorplan parallel to the y-axis at the height of 1.65 m. The first Rx track Rx^+ is located at $y = 72.5$ m and consists of 18 Rx locations with the x-coordinate spanning from 7.5 m to 92.5 m with a uniform 5 m step. The coordinates of the second Rx track (Rx^- in Fig. 5.1) are symmetric to Rx^+ with respect to the yz-plane at $x = 50$ m (center of the floorplan).

5.2.2 Finite-Difference Time-Domain

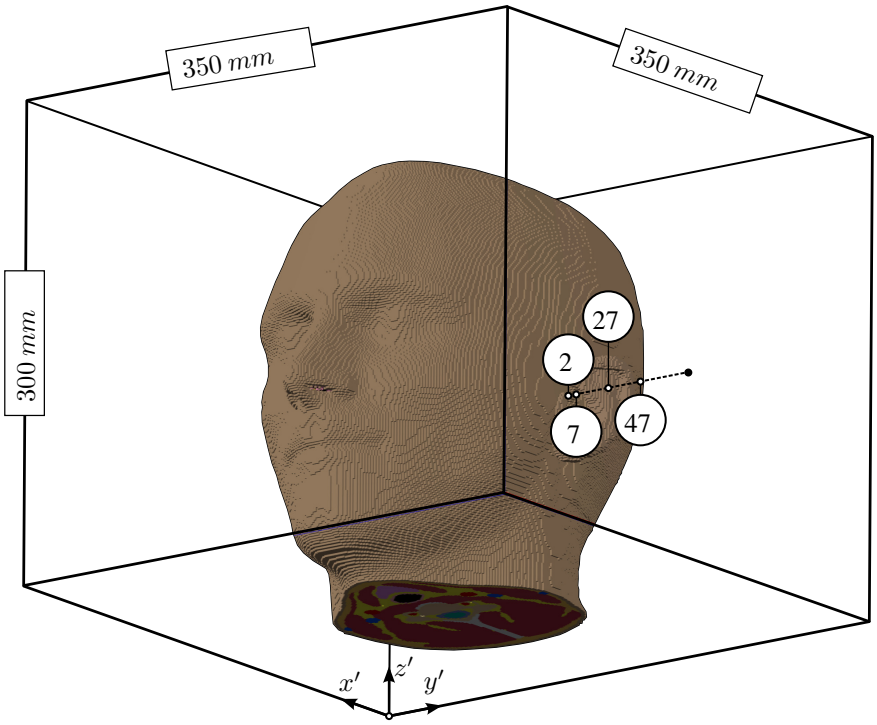

Figure 5.2: The FDTD simulation domain. Voxels of the Duke phantom's head included in the domain are shown. The points at which the UE radiation pattern is evaluated are marked with white dots, and their distance to the head (in mm) is marked with a call-out.

The FDTD simulation domain is shown in Fig. 5.2. The setup is similar to the one described in Chapters 3 and 4 and uses the same human phantom model (ViP v.3.1 Duke [14]). The domain dimensions were increased up to 350 mm by 350 mm by 300 mm to allow the UE to be positioned further away from the phantom's head and gain more insight into the EMF distribution in the residual peaks around the hot-spot, The head's bounding box is centered with respect to the domain in the xy-plane.

To interface the RT and the FDTD domains, a UE position is fixed relative to the phantom's head (some of the UE locations studied in the following sections are shown with white dots in Fig. 5.2). The head-UE separation distance is further denoted as δ. A UE location corresponds to the location of an Rx point in the RT simulation, and the directions of coordinate axes of both simulation domains coincide. For a fixed Rx point k, the RT solution provides a set of incident rays

emanating from each Tx point n. DoAs of the incident rays are then discretized by replacing them with the outer normal vectors of an icosahedral sphere, to which they have the shortest angular distance. An icosahedral sphere of frequency 3 was used, which has $m = 220$ triangular faces. After that, the discretized rays with matching DoAs are superimposed by taking a sum of their complex amplitudes, producing a reduced set of rays per Tx-Rx pair, which we further denote as $\{r_i\}_{kn}$. Performing this procedure for each Tx-Rx pair yields a discretized set of rays in an RT simulation $\{r_i\} = \bigcup\{r_i\}_{kn}$. Index i tracks the icosahedral sphere normal and does not exceed their overall count.

5.2.3 Channel matrix

In Chapter 4 a half-wavelength dipole was representing the UE antenna. In this section, a more straightforward and realistic approach to model an electrically-small 5G antenna [15] is used. The channel matrix $\mathbf{H}_{kn}$ is constructed using the discretized rays $\{r_i\}_{kn}$ (see (3.3)). Presence of the head disrupts the EMF at the UE obtained with the RT method (in free space). To take this into account, vertical component of the E-field E_z is sampled at the UE (at distance d from the head) from the single-plane-wave FDTD simulation performed for each of the discretized rays incidence directions, yielding a set of complex coefficients $A_i(d)$. According to the receive-transmit antenna reciprocity, A_i is proportional to the far-field radiation pattern of a small vertically-polarized dipole separated by distance d from the head in the DoA corresponding to the direction outer normal of the icosahedral sphere with index i.

Then, the channel coefficient h_{kn} between the Tx antenna with index n and the Rx antenna with index k is found as

$$h_{kn}(d) = \sum_{r \in \{r_i\}_{kn}} A_i(d) \tilde{E}_r^{\theta}, \tag{5.1}$$

where $\tilde{E}_r^{\theta}$ is given by (4.2) and r tracks the index of all rays in $\{r_i\}_{kn}$. Compared to (4.3), (5.1) is less computationally expensive, as the summation is taken over a much smaller (and fixed) number of incident directions than the overall number of rays produced by the RT solver. Evaluating (5.1) for every Tx-Rx pair, we obtain the full massive MIMO channel matrix $\mathbf{H}(d)$ with a UE at distance d from the head.

5.2.4 Transmission precoding

A massive MIMO BS dynamically sets the amplitudes and phases of its antenna elements (according to the UE channels), which are described by the *transmit vector* $\mathbf{t} \in \mathbb{C}^{N \times 1}$. In general, $\mathbf{t}$ depends on the *precoding scheme* used by the BS, active UEs in the network with their channel coefficients, and symbols transmitted to

(possibly a subset of) these UEs. In the following sections we analyze the Maximum Ratio Transmission (MRT) precoding scheme. The MRT precoding matrix $\mathbf{W}_{\mathrm{MRT}}$ is given by (4.5).

The user selection vector $\mathbf{s} \in \{0,1\}^{K\times 1}$ selects the UEs to which the transmission occurs (*target UEs*). Its length equals to the number of rows in the channel matrix, its k^{th} element equals 1 if the k^{th} UE is targeted, and 0 otherwise. With this we obtain the transmit vector as

$$\mathbf{t} = \alpha \mathbf{W}_{\mathrm{MRT}} \mathbf{s}, \tag{5.2}$$

where α is a normalization coefficient that determines the total BS output power. In this chapter, α is always chosen such that $\mathbf{t}$ has unit norm, setting the BS output power to 1 W.

5.2.5 EMF distributions

To determine the EMF distribution in proximity of the head and the UE, an FDTD simulation based on the RT output is performed. A ray with index r was modelled as a plane wave (PW) traversing the entire computational domain. For every direction i, an FDTD simulation with a single vertically-polarized PW is performed. We denote the resulting single-PW E-field distribution, normalized to the amplitude of the incident plane wave, as $\mathbf{e}_i(x,y,z)$.

To obtain the EMF distribution for the k^{th} UE in the DL of the BS, $\mathbf{e}_i(x,y,z)$ are superimposed with elements of the transmit vector t_n as weights.

$$e_t(x,y,z) = \sum_{i=1}^{m} \left[\mathbf{e}_i(x,y,z) \sum_{n=1}^{N} t_n \left(\sum_{r\in\{r_i\}_{kn}} \tilde{E}_r^{\theta} \right) \right]. \tag{5.3}$$

Here, the inner-most sum is taken over the amplitudes of the (discretized) rays that share the incidence direction (index i in $\{r_i\}_{kn}$), and the outer-most sum combines the E-field distributions. Therefore, it is only necessary to sum at most m E-field distributions, which greatly reduces the computation time compared to using the full set of the RT rays directly. The described procedure is also computationally more efficient than performing one FDTD simulation for each scenario, as was done in Chapters 3 and 4.

5.2.6 Exposure assessment

Evaluating (5.3) yields the E-field distribution in the FDTD domain. The ratio of the EMF power dissipated in the FDTD voxel to the mass of that voxel approximates the local Specific Absorption Rate (SAR). First, SAR is calculated in the phantom's tissues with the knowledge of their density and dielectric properties. Then, around each lossy voxel in the domain, the SAR is averaged over a cube containing 10

grams of media, according to the IEEE/IEC 62704-1 standard [16]. Finally, the cube with the highest average SAR is determined (peak-cube). The corresponding SAR value is called peak-spatial SAR averaged over a 10-g cube ($\text{psSAR}_{10\text{g}}$). $\text{psSAR}_{10\text{g}}$ in the head is one of the quantities for which basic restrictions are specified by International Comission on Non-Ionizing Radiation (ICNIRP) [17]. $\text{psSAR}_{10\text{g}}$ limit at 3.5 GHz for non-occupational exposure is 2 W/kg. In addition ICNIRP specifies the basic restrictions for the incident EMF power density (10 W/m^2). The power density below the reference level in the *far field* of an antenna is considered to result in the $\text{psSAR}_{10\text{g}}$ complying to the basic restrictions. Indeed, extensive numerical studies [18–20] in the sub-6 GHz frequency range, in which human phantoms were exposed to a *single* PW in full range of incident directions with vertical and horizontal polarization found $\text{psSAR}_{10\text{g}}$ in the head to closely approach the ICNIRP reference. It was also shown in Chapter 4 (see also [21]) that in favourable propagation conditions, a collocated 36-antenna BS array transmitting to a single UE with the MRT precoding, resulted in $\text{psSAR}_{10\text{g}}$ that is on average 5 dB lower than the ICNIRP basic restriction, with the BS power normalized such that the peak ('hot-spot') power density in the domain was 10 W/m^2 with the phantom present. In this chapter, we extend the approach proposed earlier in Chapter 4 and introduce the normalized $\text{psSAR}_{10\text{g}}$, that now includes the explicit dependence on the EMF sampling location ($\mathbf{r}$), as

$$\eta = \frac{\text{psSAR}_{10\text{g}}}{\mathbf{s}(\mathbf{r})}, \tag{5.4}$$

where $\mathbf{s}(\mathbf{r})$ is the time-averaged EMF power flux density at point $\mathbf{r}$. It is important to keep track of the location at which the EMF is assessed, as in proximity to a hot-spot its value may vary significantly over sub-wavelength distances. In 'hot-spot' scenarios the time-averaged EMF distribution varies greatly within sub-wavelength distances, and the exact location in which the EMF is assessed (e.g., when measured for compliance testing) plays an important role, as shown further.

5.3 Results

This section presents the simulation results. First, the EMF distribution in vicinity of the head are discussed and its variation with the change of the UE-to-head distance is established. Then, we look at the EMF exposure and compare different normalization approaches. Lastly, we also look at the organ-specific SAR to find out which parts of the head are more easily exposed in each scenario.

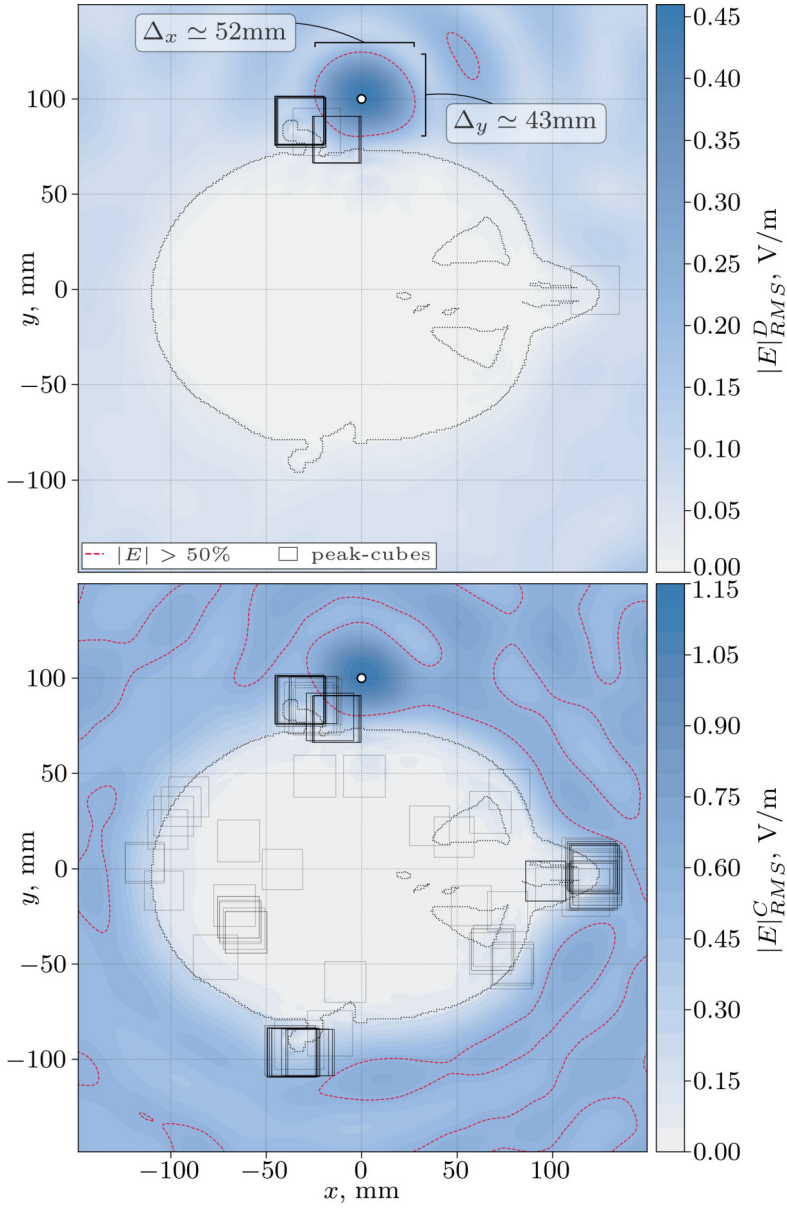

Figure 5.3: Horizontal plane cross-section of the Rx^+ track-average RMS E-field with MRT precoding and $\delta = 27$ mm head-UE distance (top: distributed BS, bottom: collocated BS). At all UE positions from the Rx^+ track, the phantom head blocks the LOS paths to the collocated BS elements. The white circle marks the UE position. The black solid rectangles show the peak-cube sizes and positions. The black dotted line shows the outline of the phantom's head. The half-maximum E_{RMS} level is outlined with the dashed red lines. The BS input power is 1 W at 3.5 GHz.

5.3.1 EMF Distributions

First, we examine the E-field focusing produced by the two studied BS layouts using the MRT precoding to target a single UE with a fixed 27 mm distance to the phantom's head δ (see Fig. 5.2). We consider the UE locations that belong to the Rx^+ and Rx^- tracks (see Fig. 5.1). The arithmetic average of the root-mean-square (RMS) E-field (E_{RMS}) taken over the UEs from one track approximates the time-average E-field of a user moving along that track with a constant speed in the direction indicated in Fig. 5.1 with arrows. Here, the effects of the non-zero UE speed on the channel are neglected, i.e. the movement is assumed to be quasi-static.

5.3.1.1 Hot-spot size

Fig. 5.3 shows the E_{RMS} in the horizontal slice coincident with the UE and averaged over the Rx^+ track in 10 environment samples (190 E_{RMS} samples per configuration). For all Rx locations in this track, the phantom's head blocks the LOS paths from all collocated BS antenna elements, thus shadowing the UE (Fig. 5.3, bottom). This is not the case for the distributed BS (Fig. 5.3, top), for which around a quarter of all Tx elements are in LOS, some of which are possibly blocked by the PEC scatterers in the environment. Nevertheless, due to a higher average propagation loss (larger average Tx-Rx distance) of the distributed BS, the maximum E-field produced by the collocated BS array exceeds it more than twofold (compare the pseudo-color scales in Fig. 5.3). The MRT precoding 'hot-spot' is centered around the UE location in both cases, marked with the white dot in Fig. 5.3. One parameter of interest we use to characterize the hot-spot is its half-maximum width in x and y directions, which we denote as Δ_x and Δ_y, respectively. Δ_x (Δ_y) is defined as the x (y) dimensions of the axes-aligned boundary box drawn around the contiguous region in which E_{RMS} exceeds its half-maximum level in the domain. The red dashed contours in Fig. 5.3 show the E_{RMS} half-maximum level. The time-average hot-spot is clearly identified for the distributed BS topology, and $\Delta_x \simeq 52$ mm ($\simeq 0.6\lambda$), $\Delta_y \simeq 43$ mm ($\simeq 0.5\lambda$), as indicated (Fig. 5.3, top). With the collocated BS, the half-maximum boundaries extend outside the FDTD domain. This is caused by a relatively high (approaching the half-maximum value) *background* E_{RMS}, i.e. the E-field levels observed in proximity of the head, but outside of the peak E_{RMS} neighborhood.

We then examine the distribution of the *instantaneous* Δ_x and Δ_y over those samples for which the averaging was performed. The Cumulative Distribution Functions (CDFs) of Δ_x and Δ_y for the two BS layouts and two Rx tracks are shown in Fig. 5.4.

We first discuss the hot-spot size distributions for the UEs on the Rx^+ track. In the distributed BS configuration transmitting to Rx^+, nearly no instantaneous hot-spots are larger than 100 mm ($\simeq 1.1\lambda$) in x and 75 mm ($\simeq 0.9\lambda$) in y (black

and red solid lines in Fig. 5.4). Their distributions' median value approximately equals the hot-spot size calculated for the sample-average E_{RMS}, indicating that the hot-spot shape and position are consistent throughout the E_{RMS} samples. The median value of Δ_x^C and Δ_y^C (green and blue solid lines in Fig. 5.4) is slightly above 70 mm, and 51 mm, respectively, which is larger than what is found with the distributed BS. Importantly, a significant portion of hot-spots extends outside the FDTD domain. For Δ_x^C that means having values greater than around 75 mm (approximately 30% of samples) and for Δ_y^C - greater than 150 mm (nearly 20% of samples). This shows that in some cases the collocated BS produces notably worse E-field focusing, which might result from its propagation diversity deficiency, i.e. narrow DoA spread shared by a large fraction of the collocated BS elements.

We also look at the hot-spot properties of Rx^- track. The distributions of $\Delta_x^D(\text{Rx}^-)$ and $\Delta_y^D(\text{Rx}^-)$ (black and red dashed lines in Fig. 5.4) are almost identical to those of $\Delta_x^D(\text{Rx}^+)$ and $\Delta_y^D(\text{Rx}^+)$, respectively, with slightly fewer $\Delta_y^D(\text{Rx}^-)$ samples having values above 50 mm. Interestingly, the collocated BS performs worse compared to the Rx^+ track. This is especially distinct in case of $\Delta_x^C(\text{Rx}^-)$ (green dashed line), for which the median value is around 100 mm, and around a quarter of all samples approaches 300 mm. The distribution of $\Delta_y^C(\text{Rx}^-)$ is nearly identical to that of $\Delta_x^C(\text{Rx}^+)$. As more antenna elements of the collocated BS reach Rx^- in LOS, experiencing less reflections, the DoA diversity is further reduced, resulting in poorer EMF focusing. However, it is clear that Δ is sensitive to the choice of the E_{RMS} threshold value for the hot-spot size evaluation.

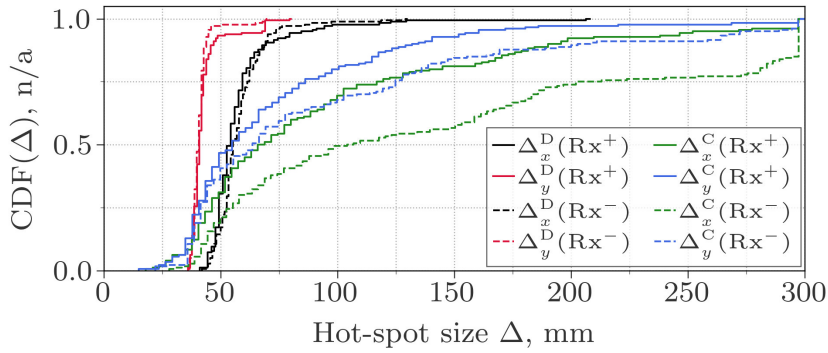

Figure 5.4: Cumulative distributions of the hot-spot widths Δ at half-maximum in x and y directions for Rx^+ (solid) and Rx^- (dashed). Hot-spots produced by the distributed BS are displayed in black (Δ_x^D) and red (Δ_y^D). The collocated BS Δ are shown in green (Δ_x^D) and blue (Δ_y^D).

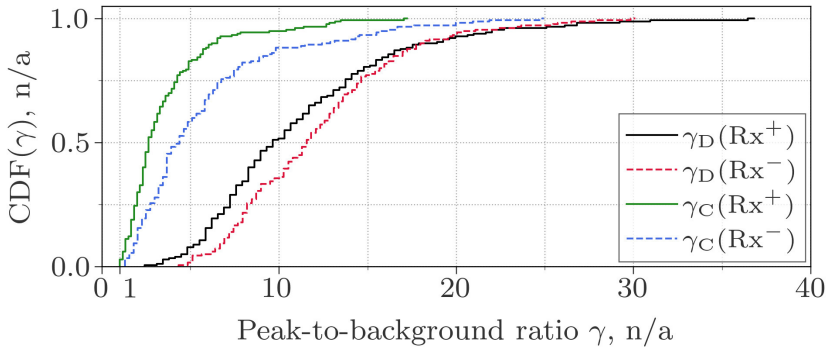

Figure 5.5: Cumulative distributions of the peak-to-background ratios γ for Rx^+ (solid) and Rx^- (dashed). The values obtained with $\mathrm{BS_D}$ are displayed in solid black ($\gamma_D(\mathrm{Rx}^+)$) and dashed red ($\gamma_D(\mathrm{Rx}^-)$). The values obtained with $\mathrm{BS_C}$ are displayed in solid green ($\gamma_C(\mathrm{Rx}^+)$) and dashed blue ($\gamma_C(\mathrm{Rx}^-)$).

5.3.1.2 Peak-to-background ratio

Another metric with which we characterize the EMF focusing is the E_{RMS} peak-to-background ratio γ, defined similar to the power density ratio S_k (4.9) in Chapter 4. We calculate it by taking the ratio of the maximum E_{RMS} in the domain (hot-spot) to the E_{RMS} value at the location symmetrical to the maximum location with respect to the xz-plane, which is also (approximately) a symmetry plane of the phantom's head. Therefore, γ quantifies a small-scale E_{RMS} gain that the massive MIMO precoding achieves by comparing E_{RMS} at two locations equivalent with respect to the geometry in their closest vicinity. Fig. 5.5 shows CDFs of γ for different BS layouts transmitting to different Rx tracks. All samples of γ in every configuration have values greater than one, meaning that the MRT precoding always enhances the signal strength at the UE side of the phantom's head, compared to the opposite side. This is indeed not a trivial result, in particular in scenarios with the collocated BS. For example, the Rx in the center of Rx^+ has around 60% of all power incident from the right side (direction to the BS). This would result in $\gamma < 1$ due to the effect of shadowing by the phantom's head, if not for the BS transmission precoding. As a reference, if exposed by a single plane wave propagating in the positive direction of the y-axis, γ can be as low as 0.25. However, the median value of $\gamma_C(\mathrm{Rx}^+)$ is only slightly above 2, which explains why the hot-spot cannot be clearly resolved at its half-maximum level: at least half of the time the E_{RMS} enhancement is not strong enough. The median of $\gamma_C(\mathrm{Rx}^+)$ is just below 5, the shadowing effect in this case aids the E_{RMS} focusing.

With the BS in the distributed configuration, significantly higher values of γ are observed. The median values of $\gamma_D(\mathrm{Rx}^+)$ and $\gamma_D(\mathrm{Rx}^-)$ are around 10 and 12,

respectively. The difference between the tracks is not as pronounced as with the collocated BS. Indeed, with the BS antennas distributed at the ceiling, though the UE at the Rx^{+} track is facing around three times more antenna elements than the UE at the Rx^{-} track, most of these extra antenna elements are also considerably further away from the UE, which reduces their contribution to the total incident power.

5.3.2 Head-to-UE distance

To generalize the results obtained in the previous section, we repeat the same set of simulations that was executed for $\delta = 27$ mm for four more UE-head separation distances $\delta \in \{2\text{ mm}, 7\text{ mm}, 12\text{ mm}, 47\text{ mm}\}$. The E_{RMS} distributions in proximity of the hot-spot are compared for $\delta \in \{7\text{ mm}, 27\text{ mm}, 47\text{ mm}\}$ with $\mathrm{BS_D}$ (top row) and $\mathrm{BS_C}$ (bottom row) of Fig. 5.6. The FDTD domain is cropped such that only its portion around the UE (white dot in Fig. 5.6) is shown in each configuration. In addition, the red cross marks the location of the peak E_{RMS} in the hot-spot, which we consider to be the hot-spot center.

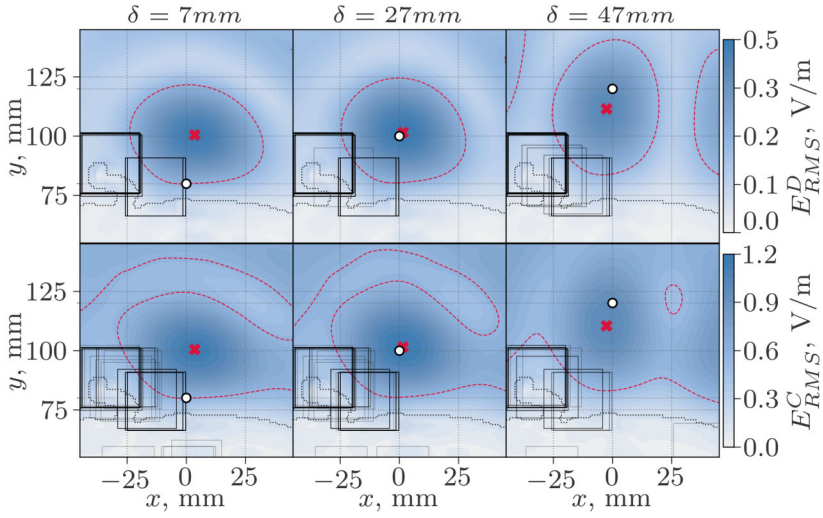

Figure 5.6: The average E_{RMS} hot-spots for different head-UE separation distances δ. The top and bottom rows show scenarios with $\mathrm{BS_D}$ and $\mathrm{BS_C}$ array layout, respectively. The value of δ is fixed in each column and indicated at the top. The peak E-field location is marked with the the red cross. The UE location is marked with the white circle. In addition, the red dashed line delimits the half-maximum E-field region. The BS input power is 1 W at 3.5 GHz.

It is clear that the hot-spot (on average) is not centered around the UE for

$\delta \in \{7\text{ mm}, 47\text{ mm}\}$. The hot-spot position and shape for $\delta = 7$ mm are nearly identical to those when $\delta = 27$ mm, as can be seen comparing the left and the center columns of Fig. 5.6. With the UE further away from the head ($\delta = 47$ mm), the hot-spot increases in size in y direction, and at the same time its center is shifted towards the UE (but does not coincide with it). These results are counterintuitive: one would expect the MRT precoding to ensure the optimal constructive interference of the incident EMF at the UE location, and the large BS antenna count - to make the same unlikely at any other location. An explanation to this observation is given in the following section.

5.3.2.1 Peak-to-UE distance

To study this effect in more detail, in Fig. 5.7 we plot the CDFs of the distance ρ from the instantaneous hot-spot to the UE calculated for the 6 configurations shown in Fig. 5.6.

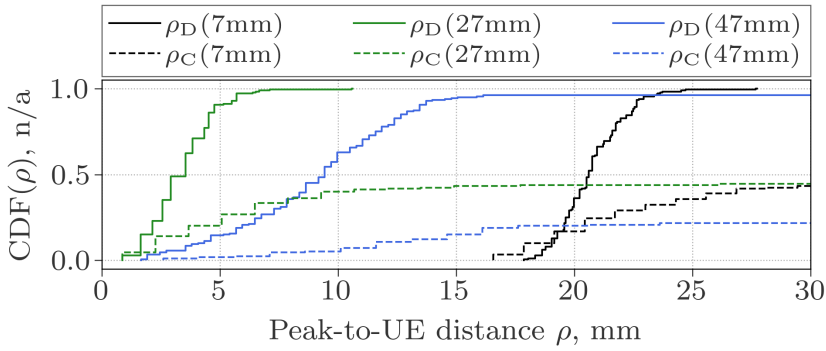

Figure 5.7: Cumulative distributions of the hot-spot center distance from the UE ρ for Rx^+. Hot-spots produced by the BS_D and BS_C are drawn with solid and dashed lines, respectively. The black, blue, and green lines show ρ for scenarios with $\delta = 7$ mm, 27 mm, and 47 mm, respectively.

Interestingly, with the BS_C configuration irrespective of the UE-to-head distance δ, in around half of all samples the hot-spot peak was not found near the UE ($\text{CDF}(\rho_\text{C}) \lesssim 0.5$ in Fig. 5.7). However, this does not mean that the collocated BS often fails to produce the EMF gain at the UE (as Fig. 5.5 shows the opposite). This rather suggests that the gain is not strong enough to dominate the EMF peaks that occur naturally (e.g., in single-PW exposure scenarios [18]) near the irregular the anatomical features of the phantom model (i.e., ears' edges, nostrils).

The distributed BS forms the hot-spot around the UE at $\rho = 27$ mm with the accuracy of around 5 mm in almost all simulated samples (green solid line in Fig. 5.7). If the UE is 47 mm away from the head, nearly in all cases the hot-spot

peak was not further than 15 mm from it (not exceeding 10 mm most of the time). However, with the UE very close to the head ($\delta = 7$ mm, black solid line in Fig. 5.7), the hot-spot was never formed around it. The similarity of the average EMF distributions in Fig. 5.6 and, at the same time, the shapes of the CDFs of ρ for scenarios with $\delta = 7$ mm and $\delta = 27$ mm suggests that, in fact, a nearly identical transmission precoding is performed by $\mathrm{BS_D}$.

5.3.2.2 Radiation pattern correlation

To understand how this happens we examine the evolution of the UE radiation pattern ($A_i(d)$ in (5.1)) as it moves further away from the head (along the black dashed line in Fig. 5.2). We calculate the correlation coefficient

$$\chi(d_j, d_k) = \frac{|\sum_i^m A_i(d_j) A_i^*(d_k)|}{\sum_i^m |A_i(d_j)||A_i(d_k)|}, \tag{5.5}$$

where $(\cdot)^*$ denotes the complex conjugate, and $|\cdot|$ is the absolute value of a complex number. In (5.5), the icosahedral sphere facet index i tracks the components of the radiation patterns, viewed as vectors $\mathbf{A} = [A_1, A_2, \ldots, A_m]^T \in \mathbb{C}^{m\times 1}$. The closer $\chi(d_j, d_k)$ is to unity, the more similar $\mathbf{A}(d_j)$ and $\mathbf{A}(d_k)$ are. Equation (5.5) is first evaluated with the electrically small antenna pattern for $d = \delta \in [2 \text{ mm}, 72 \text{ mm}]$. In addition, we also evaluate (5.5) with the radiation pattern $\mathbf{A}_{\lambda/2}(d)$ of the half-wave dipole model used in Chapter 4, with its center matching the small dipole location. Fig. 5.8 shows $\chi(d_j, d_k)$ matrices of the short (below the diagonal) and the half-wave (above the diagonal) dipoles. The correlation is strong ($\chi(d_j, d_k) \simeq 1$ for $d_j \simeq d_k$) for both dipole models, and the near-diagonal elements are close to 1. The red dashed line in Fig. 5.8 delimits the area, within which χ exceeds 80%.

Interestingly, the short dipole radiation pattern is highly-correlated for all values of δ from 2 mm to around 35 mm. Therefore, the channel matrix (5.1), the precoding matrix (4.5), and hence the BS transmit vector (5.2), do not change significantly with the small dipole position in that range. This explains the similarity of the EMF distributions in the hot-spots for $\delta = 7$ mm and $\delta = 27$ mm in Fig. 5.6: the BS transmits with almost the same weight.

To explain why the hot-spot is formed consistently around the small dipole at $\delta = 27$ mm and *not* at $\delta = 7$ mm, even when the latter was targeted, we also plot the arithmetic mean ($|\bar{\mathbf{A}}| = \frac{\beta_1}{m}\sum_i^m |A_i(d)|$) and the maximum magnitudes $\max(|\mathbf{A}|) = \max_i |A_i(d)|$, as (normalized with β_1 and β_2) functions of δ, shown in Fig. 5.9.

Both the average and the maximum magnitude of the small dipole pattern fall off rapidly as it approaches the head (dashed black lines in Fig. 5.9). $A_i(\delta)$ are defined as the E_{RMS} measured at distance δ from the phantom's head after it is exposed with a plane wave incident with the DoA i (see section 5.2.3). Taken together with the observation in the previous paragraph, this means that the combination

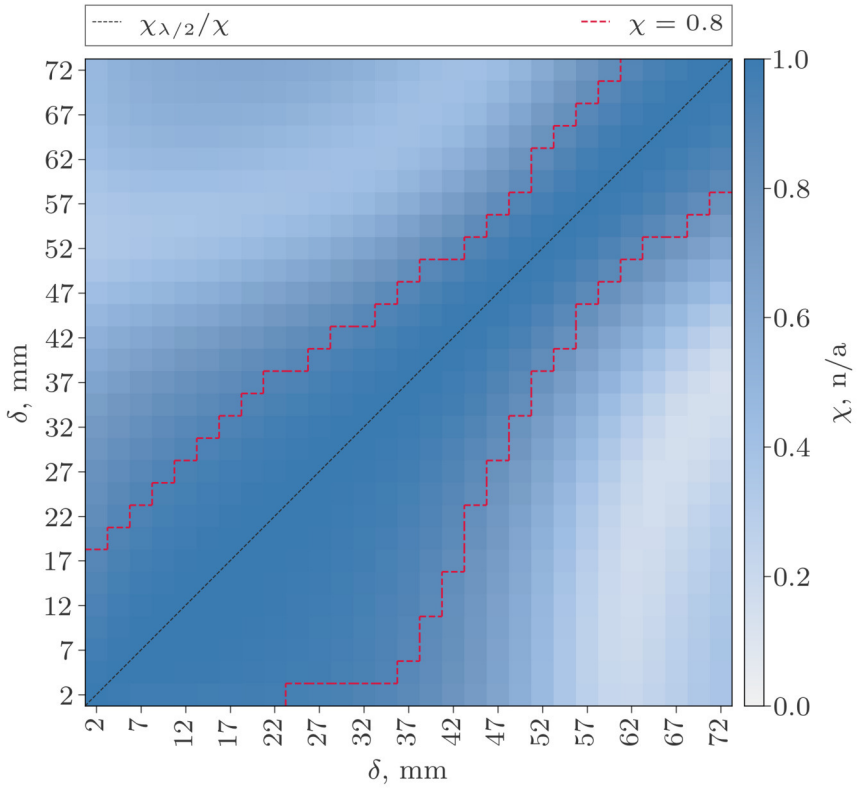

Figure 5.8: Correlation matrix of the UE radiation pattern as a function of the UE-head separation distance δ. The top-left and the bottom-right triangles (delimited by the dashed black line) show the matrices corresponding to the half-wave ($|\mathbf{A}|_{\lambda/2}(d)$) and the small dipole ($|\mathbf{A}|(d)$) antennas, respectively. The red dashed lines mark the boundary of the region where the correlation crosses the 80% level.

of plane waves interfering constructively close to the head (e.g., at $\delta = 7$ mm), combine (nearly as) constructively, but with a larger amplitude further away (e.g., at $\delta = 27$ mm). Quantitatively, as shown in figure Fig. 5.9, at $\delta = 7$ mm both $|\bar{\mathbf{A}}|$ and $\max(|\mathbf{A}|)$ are approximately two times smaller than at $\delta = 27$ mm, where they (nearly reach their maximum). This agrees well with what is shown in the first two columns of Fig. 5.6.

At even larger distances from the head (e.g., $\delta = 47$ mm shown in the third column of Fig. 5.6), the correlation of $\mathbf{A}$ decreases considerably (down to around 67% relative to $\delta = 27$ mm), while $|\bar{\mathbf{A}}|$ and $\max(|\mathbf{A}|)$ are only around 10% lower, as can be seen from Figs. 5.8 and 5.9. Hence, it is possible to form the hot-spot more accurately at $\delta = 47$ mm, though its peak tends to up to 15 mm lower values

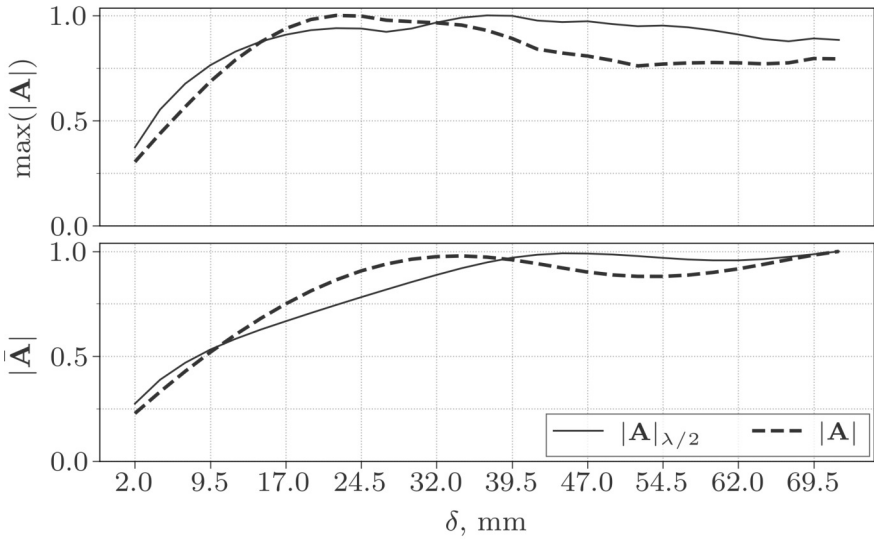

Figure 5.9: UE directivity magnitude as a function of the UE-head separation distance. Solid and dashed lines show the half-wave ($|\mathbf{A}|_{\lambda/2}(d)$) and the small dipole ($|\mathbf{A}|(d)$) values, respectively. Top: maximum pattern magnitude (directivity). Bottom: pattern magnitude averaged over the direction of arrival.

of δ, as shown in Fig. 5.7.

The half-wave dipole's radiation pattern $\mathbf{A}_{\lambda/2}(d)$ correlation and magnitudes are shown in Figs. 5.8 (upper triangle) and 5.9 (solid black lines), respectively. $\mathbf{A}_{\lambda/2}(d)$ exhibits more variation (Fig. 5.8), especially at small δ, compared to $\mathbf{A}(d)$, possibly due to its larger size. This could help to decorrelate two closely spaced receivers near the head, e.g., in a multi-antenna UE. The variation of $|\mathbf{A}|_{\lambda/2}(d)$ (Fig. 5.9) is qualitatively similar to that of $|\mathbf{A}|(d)$, though in this case it cannot be directly related to E_{RMS} at the UE location.

In the next section we analyze the exposure in the hot-spots produced with the small dipole. Investigation of the hot-spots with the half-wavelength dipole (or a more realistic UE antenna model) is out of this chapter's scope, but could be one of the future research topics, as indicated in Chapter 8.

5.3.2.3 Peak-spatial SAR

This section presents η the peak-spatial SAR averaged over a 10 g cube ($\text{psSAR}_{10\text{g}}$), normalized to the time-averaged power flux density ($\mathbf{s}(\mathbf{r})$), as defined in (4.10). As mentioned in Section 5.2.6, it is important to keep track of the point $\mathbf{r}$ at which $\mathbf{s}$ is sampled, as the time-averaged EMF levels may vary significantly in vicinity of a hot-spot. In this section two normalization strategies are compared. First,

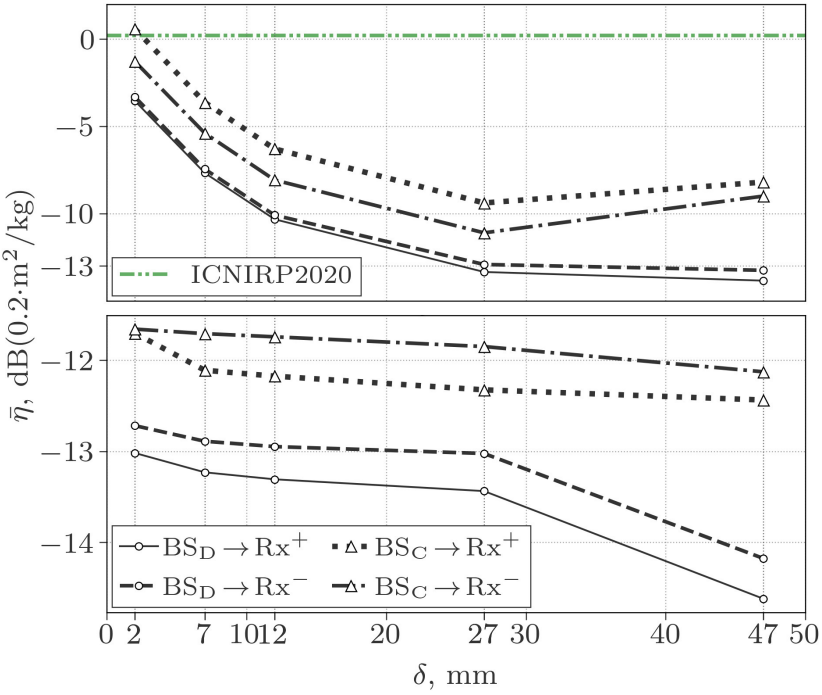

Figure 5.10: The sample-average psSAR$_{10g}$ normalized to the time-average power density (η) at the UE location (top) or at the FDTD domain maximum (bottom), as a function of δ. η in scenarios with BS$_D$ (BS$_C$), calculated for the Rx$^+$ and Rx$^-$ tracks are shown with the black solid (dotted) and dashed (dash-dotted) lines with circle (triangle) markers, respectively. η calculated from the ICNIRP reference values is shown with the dash-double-dotted horizontal green line as a reference.

$\mathbf{s}_{\mathrm{UE}} = \mathbf{s}(\mathbf{r}_{\mathrm{UE}})$ is measured at the UE location, which is known in advance in each scenario. Second, the maximum of $\mathbf{s}(\mathbf{r})$ over the complete FDTD domain $\mathbf{s}_{max}$ is taken. The location of the maximum $\mathbf{r}_{max}$ is determined for each sample, and often is not found close the UE, especially with BS$_C$, as mentioned in Section 5.3.2.1 and is seen in Fig. 5.7. Fig. 5.10 shows the sample-average values of η_{UE} (top) and η_{max} (bottom), for the BS$_D$ and BS$_C$ configurations, averaged over the Rx$^+$ and Rx$^-$ UE tracks.

The psSAR$_{10g}$ normalized with both strategies is higher in scenarios with BS$_C$ than in the corresponding scenarios with BS$_D$. The sample-average of η_{max} with BS$_C$ (Fig. 5.10, bottom) slightly decreases with δ, staying around 12 dB lower than the ICNIRP reference (0.2 m^2/kg) for both Rx$^+$ (dotted line) and Rx$^-$ (dash-dotted line). For BS$_D$, the sample-average of η_{max} is approximately constant and around

13 dB below the ICNIRP reference for $\delta \in [2\text{mm}, 27\text{mm}]$ and drops to around 14 dB below at $\delta = 47$ mm.

In contrast to that, the sample-average of η_{UE} goes up rapidly at small δ. However, this is only due to the fact that it is less likely to find the peak EMF near the UE for $\delta < 27$ mm, as was discussed in Section 5.3.2.1. Thus, while the average $\mathrm{psSAR}_{10\mathrm{g}}$ does not increase at small δ, the EMF at the UE location decreases, causing the increase of the normalized quantity η_{UE}. $\hat{\eta}_{\mathrm{UE}}$ with $\mathrm{BS_C}$ and Rx^+ (the collocated BS and the UE blocked by the head) reaches the ICNIRP reference at $\delta = 2$ mm (dashed line in Fig. 5.10, top), and falls to the level of around -10 dB at $\delta \geqslant 27$ mm. $\hat{\eta}_{\mathrm{UE}}$ is around 2 dB lower than that at all δ for $\mathrm{BS_C}$ transmitting to Rx^- (dash-dotted line). With $\mathrm{BS_D}$, $\hat{\eta}_{\mathrm{UE}}$ has nearly equal values in scenarios with Rx^+ and Rx^- (solid and dashed lines in Fig. 5.10, top), reaching their maximum of around -4 dB at $\delta = 2$ mm and falling to around -13 dB at $\delta = 27$ mm (where it coincides with $\hat{\eta}_{max}$).

$\hat{\eta}_{\mathrm{UE}}$ can be interpreted as the normalized $\mathrm{psSAR}_{10\mathrm{g}}$ under the assumption that the BS performing the power control that maintains the received signal level at the UE. As the UE close to the user head cannot be accurately focused towards, the BS is bound to higher the output power, which increases $\mathrm{psSAR}_{10\mathrm{g}}$. In addition, functional dependencies similar to the ones shown in Fig. 5.10 (top), e.g., with site-specific RT simulations, and BS/UE parameters, could be applied to the DL exposure estimation by measuring the UE received power. By first simulating the EMF distribution around the phantom head and then using the UE measurements (at a known position with respect to the head) as the calibration factor, the $\mathrm{psSAR}_{10\mathrm{g}}$ can be determined. It is worth pointing out that currently the reference levels are assessed in free space, according to the ICNIRP guidelines. The presented results indicate that it is essential to carefully consider both the UE and the user body position relative to each other and the BS, to accurately measure the actual peak EMF levels.

Finally, a comparison with the normalized $\mathrm{psSAR}_{10\mathrm{g}}$ determined in Chapter 4 can be made. In Section 4.3.4 (see Fig. 4.8), the average value of $\eta_{hs} \simeq -5$ dB is given, with the UE-head distance of 20 mm. In this chapter, a value from around -7 dB to -10 dB is found by linear interpolation of $\bar{\eta}_{max}$ in a similar (collocated) BS configuration transmitting to Rx^+ or Rx^-. The 2 dB to 5 dB lower result is likely due to a larger BS antenna count (100 elements in this chapter vs. 36 in Chapter 4), resulting in a better EMF focusing.

5.4 Comparison with ATTO-cells

The normalized exposure results allow comparing the massive MIMO deployment to the ATTO-floor network, studied in Chapter 2. It is worth noting that the two technologies are complementary in terms of the wireless coverage, use-cases and the

exposure they induce. The ATTO-floor was shown to always induce the psSAR_{10g} in the phantom's feet, while massive MIMO produces highly-focused psSAR_{10g} in the head.

In Chapter 2 it was shown that to violate the ICNIRP basic restrictions, a power of around 1 W per ATTO-cell would be needed. The same approach, with respect to the ICNIRP basic restrictions for the head (2 W/kg), calculated with the sample-average psSAR_{10g} of BS_C yields the threshold value of around 10^4 W per BS, or 100 W per antenna element. The same analysis with BS_D yields an even higher value of around 10^3 W per antenna element, which is around an order of magnitude higher than the maximum *total* BS power [22]. Such high values are explained by a large BS-UE separation distance (> 25 m), compared to the near-field EMF interaction (< 0.1 m) with the ATTO-floor. This allows to conclude that the existing exposure protection standards are conservative enough with respect to the DL transmission of both collocated and distributed massive MIMO in indoor scenarios.

5.5 Conclusion

In this chapter, the EMF distributions and the psSAR_{10g} induced in the collocated and distributed massive MIMO configurations were compared in a model of an industrial indoor environment. It was shown that in both cases the hot-spot produced by the BS transmitting with the MRT scheme does not coincide with the UE (small dipole) antenna, if its distance to the user head is shorter than 27 mm. The psSAR_{10g} induced in the phantom's head normalized to the time-averaged power flux density assessed at the hot-spot maximum, showing values from 12 dB to 14 dB lower than the ICNIRP reference. If the EMF values are measured at the UE location, the normalized psSAR_{10g} approaches the ICNIRP reference with the UE-head distance of 2 mm. The obtained insights can be useful in practical DL 5G exposure assessment procedures.

This chapter concludes the study of the FDTD-based massive MIMO exposure. In Chapter 6 the exposure to large antenna arrays outdoors will be investigated. In addition to the MRT precoding scheme studied so far, we will also consider a codebook-based beamforming approach, relevant to the currently deployed 5G-NR BSs, and the Zero-Forcing interference-cancelling scheme, which is expected to be implemented in the near-future 5G releases. The exposure will be assessed indirectly by means of the time-averaged antenna array gain - an important BS property when determining the compliance boundary, as mentioned in Chapter 1.

References

[1] Imadur Rahman, Sara Modarres Razavi, Olof Liberg, Christian Hoymann, Henning Wiemann, Claes Tidestav, Paul Schliwa-Bertling, Patrik Persson, and Dirk Gerstenberger. *5G evolution toward 5G advanced: An overview of 3GPP releases 17 and 18*.

[2] Hien Quoc Ngo, Erik G. Larsson, and Thomas L. Marzetta. *Aspects of favorable propagation in Massive MIMO*. In 2014 22nd European Signal Processing Conference (EUSIPCO), pages 76–80, 2014.

[3] Xiaoyong Wu, Norman C. Beaulieu, and Danpu Liu. *On Favorable Propagation in Massive MIMO Systems and Different Antenna Configurations*. IEEE Access, 5:5578–5593, 2017.

[4] Alexei Ashikhmin and Thomas Marzetta. *Pilot contamination precoding in multi-cell large scale antenna systems*. In 2012 IEEE International symposium on information theory proceedings, pages 1137–1141. IEEE, 2012.

[5] Emil Björnson, Erik G Larsson, and Thomas L Marzetta. *Massive MIMO: Ten myths and one critical question*. IEEE Communications Magazine, 54(2):114–123, 2016.

[6] Upamanyu Madhow, Donald Richard Brown, Soura Dasgupta, and Raghuraman Mudumbai. *Distributed massive MIMO: Algorithms, architectures and concept systems*. In 2014 Information Theory and Applications Workshop (ITA), pages 1–7. IEEE, 2014.

[7] Jiayi Zhang, Emil Björnson, Michail Matthaiou, Derrick Wing Kwan Ng, Hong Yang, and David J. Love. *Prospective Multiple Antenna Technologies for Beyond 5G*. IEEE Journal on Selected Areas in Communications, 38(8):1637–1660, 2020.

[8] Hien Quoc Ngo, Alexei Ashikhmin, Hong Yang, Erik G Larsson, and Thomas L Marzetta. *Cell-free massive MIMO: Uniformly great service for everyone*. In 2015 IEEE 16th international workshop on signal processing advances in wireless communications (SPAWC), pages 201–205. IEEE, 2015.

[9] Zheng Chen and Emil Björnson. *Channel Hardening and Favorable Propagation in Cell-Free Massive MIMO With Stochastic Geometry*. IEEE Transactions on Communications, 66(11):5205–5219, 2018.

[10] Jan Hederen and Pål Frenger. *Improved Antenna Arrangement for Distributed Massive MIMO*, December 17 2020. US Patent App. 16/764,126.

[11] Giovanni Interdonato, Emil Björnson, Hien Quoc Ngo, Pål Frenger, and Erik G Larsson. *Ubiquitous cell-free massive MIMO communications*. EURASIP Journal on Wireless Communications and Networking, 2019(1):1–13, 2019.

[12] Emil Björnson, Luca Sanguinetti, Henk Wymeersch, Jakob Hoydis, and Thomas L. Marzetta. *Massive MIMO is a reality-What is next?: Five promising research directions for antenna arrays*. Digital Signal Processing, 94:3 – 20, 2019. Special Issue on Source Localization in Massive MIMO.

[13] REMCOM. *Wireless InSite 3.2.0 Reference Manual*. 2017.

[14] Marie-Christine Gosselin, Esra Neufeld, Heidi Moser, Eveline Huber, Silvia Farcito, Livia Gerber, Maria Jedensjö, Isabel Hilber, Fabienne Di Gennaro, Bryn Lloyd, et al. *Development of a new generation of high-resolution anatomical models for medical device evaluation: the Virtual Population 3.0*. Physics in medicine and biology, 59(18):5287, 2014.

[15] Duixian Liu, Wonbin Hong, Theodore S. Rappaport, Cyril Luxey, and Wei Hong. *What will 5G Antennas and Propagation Be?* IEEE Transactions on Antennas and Propagation, 65(12):6205–6212, 2017.

[16] *IEC/IEEE P62704-1/D2, October 2013: IEC/IEEE Draft Standard for Determining the Peak Spatial Average Specific Absorption Rate (SAR) in the Human Body from Wireless Communications Devices, 30 MHz - 6 GHz. Part 1: General Requirements for Using the Finite Di*. IEEE, 2013.

[17] International Commission on Non-Ionizing Radiation Protection et al. *Guidelines for limiting exposure to Electromagnetic Fields (100 kHz to 300 GHz)*. Health Physics, 118(5):483–524, 2020.

[18] T Uusitupa, I Laakso, S Ilvonen, and K Nikoskinen. *SAR variation study from 300 to 5000 MHz for 15 voxel models including different postures*. Physics in Medicine & Biology, 55(4):1157, 2010.

[19] JF Bakker, MM Paulides, A Christ, Niels Kuster, and Gerard C van Rhoon. *Assessment of induced SAR in children exposed to electromagnetic plane waves between 10 MHz and 5.6 GHz*. Physics in Medicine & Biology, 55(11):3115, 2010.

[20] JF Bakker, MM Paulides, E Neufeld, A Christ, Niels Kuster, and GC Van Rhoon. *Children and adults exposed to electromagnetic fields at the ICNIRP reference levels: theoretical assessment of the induced peak temperature increase*. Physics in Medicine & Biology, 56(15):4967, 2011.

[21] Sergei Shikhantsov, Arno Thielens, Günter Vermeeren, Piet Demeester, Luc Martens, Guy Torfs, and Wout Joseph. *Massive MIMO Propagation Modeling With User-Induced Coupling Effects Using Ray-Tracing and FDTD*. IEEE Journal on Selected Areas in Communications, 38(9):1955–1963, 2020.

[22] Ericsson. *Antenna Integrated Radio Unit Description AIR 6488*.

6

Massive MIMO Exposure in Outdoor Urban Environment

In Chapters 3 to 5 we devised a methodology for the evaluation of human exposure in terms of psSAR_{10g} in hot-spots formed by the massive MIMO arrays. The proposed methodology was applied to calculate psSAR_{10g} in a human phantom model positioned in indoor environments, though the same approach could be used with models of outdoor environments as well. We determined the ratios between the hot-spot EMF and the exposure induced in the phantom's head, such that it could be directly compared to the ICNIRP basic restrictions. However, it is often desirable to know how much power, on average a BS can output in a certain direction, e.g., when determining the compliance boundary size, as mentioned in Chapter 1. The compliance boundary is determined by the distance from the BS, beyond which the EMF it induces complies with both the ICNIRP basic restrictions *and* reference levels.

Methods for numerical estimation of the compliance boundary size were developed for the previous generations' technologies [1–3], in which BSs have fixed radiation patterns. The radiation pattern of an antenna array depends on the amplitude and phase ratios of its element excitation signals. By selecting the elements' amplitudes and phases in a specific way, a BS can produce directed 'beams' in its far-field - the main lobes of the array radiation pattern. This technique is referred to as beamforming, as explained in Chapter 1. The more elements the antenna array has (up to a certain limit), the more narrow the beams it is capable of forming. A more narrow beam means a higher maximum gain for equal total transmit power, as

the EMF energy gets focused more tightly in the desired direction. Several different beamforming and precoding techniques are discussed below.

Multi-User Multiple-Input Multiple-Output (MU-MIMO) with codebook-based beamforming simultaneously generates a subset of a predefined set of beams (the 'codebook') at a time. A user equipment (UE) uplink (UL) signaling is processed at the BS to choose the beam that best reaches the UE location. In line-of-sight (LOS) conditions, this typically is the beam which has the closest direction-of-departure (DoD) to the true direction to the UE. However, in non-LOS (NLOS), the largest portion of the EMF power might reach the UE through interactions with the propagation environment (e.g. reflections, diffractions), and thus the DoD of the beam chosen by codebook-based precoding does not necessarily correlate with the path of the shortest distance to the UE.

The Maximum Ratio Transmission (MRT) precoding scheme aims at maximizing the signal-to-noise ratio (SNR) at the target UEs [4]. If the UE in focus has a dominant LOS path, this results in forming a precisely directed single beam. If the UE is in a deep shadow region with multiple scattering paths, the BS distributes the available power over all these paths. This results in a less directive array pattern that forms a compact region with an elevated EMF around the target UE, a so-called *hot-spot*. The Zero-Forcing (ZF) on the other hand, aims to maximize the signal-to-interference ratio (SIR) at the target UEs. If the target UEs' channels correlate considerably, a large portion of the BS resources is spent for interference mitigation. By doing so, unintended hot-spots might be created in the regions of the environment without active UEs. The effect of these precoding schemes on the power distributions in the angular domain serviced by the BS will be investigated in the following sections.

Human EMF exposure in the far-field is directly related to the incident electric field (E-field) strength, typically averaged over time. The International Commission on Non-Ionizing Radiation (ICNIRP) specifies a time duration of 6 min to be used for the EMF averaging in compliance assessment [5], [6]. The averaging interval of 30 min is specified for the whole-body surface area of the E-field averaging in the most recent version of the guidelines [5]. In free space, the E-field can be directly derived from the antenna gain, which is used in practice to establish the BS compliance boundary [7]. Actual E-field values observed in an environment are influenced by propagation or blockage of the transmitted signals. Nevertheless, the time-averaged array gain is a meaningful indicator of the typical EMF exposure induced by a BS. Since array antennas adapt their radiation patterns to the environment, it is essential to include this inherently dynamic attribute in the modeling. In this chapter, we compare codebook beamforming and the aforementioned Massive MIMO transmission precoding schemes in terms of the maximum time-averaged antenna array gain they yield to distill conclusions about their effect on the EMF exposure in the serviced area.

This problem was first addressed in [8, 9] for a single antenna array performing codebook-based beamforming. Several analytically-defined DoD distributions, acting as a proxy for the distributions of users inside the serviced area (i.e. uniform, cosine in elevation and azimuth) were analyzed. All UEs were modeled in free space, thus having the LOS to the BS (no environment model was included). An analytic network utilization model was implemented to determine the number of simultaneously active UEs. The results showed around 6 dB reduction for the 95$^{\text{th}}$ percentile (p^{95}) of the maximum time-average BS gain as compared to the theoretical maximum, for high system utilization values.

In [10] the approach of [8] was extended to a BS capable of MRT precoding (dubbed eigen-beamforming [10] or conjugate beamforming [11]). The 3GPP statistical model [12] was used with an urban environment, a single 64-element BS, and both indoor and outdoor UEs. Depending on the number of simultaneously served UEs, the 95$^{\text{th}}$ percentile of the compliance distance (which is proportional to the maximum time-averaged BS gain [7]) constituted 30% to 50% of the theoretical maximum.

The method presented in this chapter builds upon and extends the approach proposed in [8, 10] to more realistic precoding schemes and a more advanced Ray-Tracing (RT) channel model. The RT modeling yields *spatially consistent* channels, which depends on the environment geometry and UEs locations. For the MU-MIMO systems one important implication is a realistic UE DoD distribution, which governs the beam directions. The magnitude of the inter-UE channel correlation depending on the distance between the UEs is captured in the RT modeling - a factor that greatly impacts the BS pattern when using interference-canceling precoding schemes such as ZF. It has been shown that the RT method reproduces key parameters of measured Massive MIMO channels [13], whereas the state-of-the-art statistical model (WINNER-II) tends to underestimate the amount of correlation in the channels of closely spaced UEs [14]. Various other approaches to 5G channel modelling have been proposed in the literature, and we direct an interested reader to recent overview articles [15, 16].

6.1 Materials and Methods

In this section we describe the environment model used in the RT simulations and methods for the results processing. An overview of the beamforming and precoding schemes is given.

6.1.1 Environment model

The RT model consists of the environment geometry description and the transmitter-receiver (Tx-Rx) parameters. A geometrical entity is represented by the coordinates

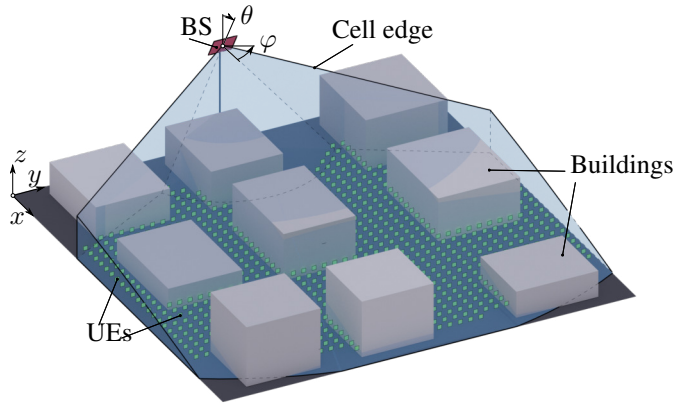

Figure 6.1: An example of an environment sample. The BS array is depicted in red. The cell boundaries are shown in blue. The Rx locations are shown in green.

of its boundary faces (polygons) and the dielectric parameters (relative permittivity ε_r and conductivity σ) of each face. A Tx (Rx) antenna is defined with its location, radiation pattern and the carrier frequency. For every Tx antenna *rays* are launched from its location, in directions (nearly) uniformly distributed on a surface of a sphere centered at the Tx [17]. A ray is an abstraction which represents a flat wavefront, described with its (complex) EMF amplitudes and the propagation direction. The rays are propagated (traced) through the environment and their interactions (reflections, diffractions and transmissions), as well as the Path Loss (PL) and time-of-flight (ToF), are tracked by the ray-tracer. If a ray passes sufficiently close to an Rx location, it is considered to be received and its state is recorded. The output of the simulation is a set of received rays for every defined Tx-Rx pair.

The RT output is site-specific, i.e. the channel between a fixed Tx-Rx pair depends on the surrounding geometry. To generalize the results a number of geometrical entities was generated stochastically, based on a few macroscopic parameters. Each realization of the environment geometry we call an *environment sample* [18]. Fig. 6.1 presents one of the environment samples obtained from the model we describe below.

We simulate an outdoor urban macrocell bounded by a fixed flat square area 100 m by 100 m in size. Building blocks are represented by cuboids, width and length of which are sampled from a uniform random distribution in range from 15 m to 25 m. The height of a building block is drawn from a uniform random distribution in range from 5 m to 20 m. The buildings are positioned on a rectilinear grid, such that any two neighboring blocks are separated by exactly one empty grid cell. Rows of building blocks and straight lanes form a Manhattan-like urban city landscape. The spacing (lane) width is set equal to 10 m, 15 m or 20 m randomly with equal probability. The dielectric properties of the cuboids model concrete

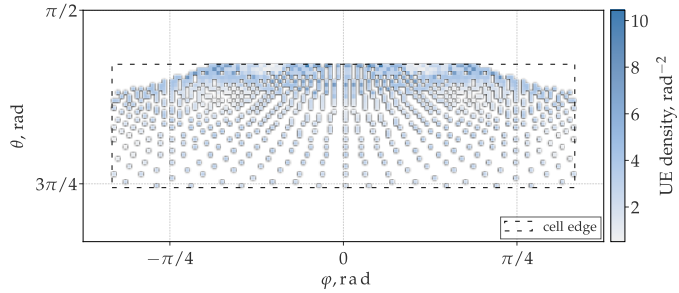

Figure 6.2: UE DoD density averaged over 25 environment samples, viewed from the center of the BS array. The dashed line marks the cell limits.

material with $\varepsilon_r = 7, \sigma = 1.5 \cdot 10^{-2}$ S/m. The ground plane is assigned asphalt dielectric properties with $\varepsilon_r = 5.7, \sigma = 5 \cdot 10^{-4}$ S/m.

The locations and properties of the Tx and Rx antennas are fixed in the model. The simulations are performed at a single frequency of 3.5 GHz, foreseen to be heavily used in 5G networks. The BS (Tx) is a rectangular 10-by-10 element array of vertically polarized half-wave dipole antennas with a half-wavelength uniform inter-element spacing ($\lambda \simeq 85$ mm at 3.5 GHz). The center of the Tx array is positioned at $x = 1$ m, $y = 50$ m and $z = 25$ m (Fig. 6.1). The BS height of 25 m correspond to the macrocell scenario in the 3GPP model [12].

In the following simulations the BS coverage range spans from $-60°$ to $+60°$ in azimuthal (φ) and from $105°$ to $135°$ in polar angular directions (θ) in coordinate system shown in Fig. 6.1. This is in accordance to the model used in [8]. To include most of the simulated ground-plane area within its coverage range, the BS array is tilted down by $30°$ around the y-axis through its center.

A UE (Rx) is modeled as a single-terminal device equipped with a vertically-oriented vertically-polarized half-wave dipole antenna. The UEs are arranged on a regular rectilinear grid with 2 m spacing in x and y directions, at a height of 1.5 m above the ground-plane (z-axis). Only the grid nodes that fall within the cell and are located outside the building block interiors are kept in the simulation, which, on average, results in around 600 UEs per simulation. These UEs are used as potential active receivers in the analysis described in Section 6.1.3.

The density of the UE locations obtained in 25 environment samples is presented in Fig. 6.2. The (φ, θ) coordinate system is shown in Fig. 6.1. Fig. 6.2 describes the UE locations in the DoD space, as viewed from the BS. The UE distribution averaged over the environment samples is symmetric with respect to the plane $\varphi = 0$, as a result of the matching (statistical) symmetry of the environment geometry. The UE density increases towards the upper cell edge (further away from the BS) as the polar angle of incidence decreases.

The RT simulation parameters were set as recommended in [19], limiting the environment interactions to up to 6 reflections, 1 diffraction and 1 transmission.

6.1.2 MIMO Channel Matrix, Beamforming and Precoding

The free-space channel coefficient, denoted in this chapter as $\hat{h}_{kn}$, where indices k and n track the Rx and Tx antennas, respectively, is given by (4.1) (see also e.g. [20]). The MIMO channel matrix $\hat{\mathbf{H}}$ is obtained by evaluating $\hat{h}_{kn}$ for each Tx-Rx pair in the simulation. Rows $\hat{\mathbf{h}}_k$ of $\hat{\mathbf{H}}$ are channel vectors to the Rx with index k. The distance from different UEs to the BS in the outdoor environment may vary significantly. Therefore, UEs will experience differences in PL in comparison to one another. Thus, channel equalization is performed by normalizing $\hat{\mathbf{H}}$ row-wise [4]

$$\mathbf{H} = [\frac{\mathbf{h}_1}{||\mathbf{h}_1||}, \frac{\mathbf{h}_2}{||\mathbf{h}_2||}, \ldots, \frac{\mathbf{h}_K}{||\mathbf{h}_K||}]^T, \tag{6.1}$$

where $||\cdot||$ denotes the Frobenius norm.

Elements of the MRT precoding matrix $\mathbf{W}_{MRT}$ are given by (4.5), in which h_{kn} are understood as the elements of $\hat{\mathbf{H}}$. Using the same normalized channel matrix $\mathbf{H}$, the ZF precoding matrix $\mathbf{W}_{ZF}$ is given by [11]

$$\mathbf{W}_{ZF} = \alpha \mathbf{H}^H (\mathbf{H}\mathbf{H}^H)^{-1}, \tag{6.2}$$

where $(\cdot)^H$ denotes the Hermitian transpose and α is a real-valued normalization coefficient, chosen such that $\mathbf{W}$ has unit Frobenius norm.

The codebook steering matrix $\mathbf{W}_{CB}$ is constructed from the steering column-vectors $\mathbf{b}_k \in \mathbb{C}^N$ as [21]

$$\mathbf{b}_k = [\exp(2\pi i(\mathbf{d}_1, \mathbf{c}_k)/\lambda), \exp(2\pi i(\mathbf{d}_2, \mathbf{c}_k)/\lambda), \ldots, \exp(2\pi i(\mathbf{d}_N, \mathbf{c}_k)/\lambda)]^T, \tag{6.3}$$

$$\mathbf{W}_{CB} = \alpha[\mathbf{b}_1, \mathbf{b}_2, \ldots, \mathbf{b}_K]. \tag{6.4}$$

In (6.3), $\mathbf{d}_n$ is a distance vector from the BS array center to the n^{th} element, $\mathbf{c}_k$ is a unit vector in the codebook direction assigned to the k^{th} UE, and $(\cdot, \cdot)$ denotes the dot product. Knowing the channel vector $\hat{\mathbf{h}}_k$, the beamforming direction $\mathbf{c}_k$ is chosen as

$$\mathbf{c}_k = \arg\max_{\{\mathbf{c}_i\}} [(\hat{\mathbf{h}}_k, \mathbf{b}_i)]. \tag{6.5}$$

In (6.5) the maximization is carried out over the set of all beamforming directions $\mathbf{c}_i$ supported by the BS. The beamforming direction vector $\mathbf{c}_i$ is a unit vector in the direction (θ_i, φ_i) of the i^{th} beam center

$$\mathbf{c}_i = \mathbf{c}(\theta_i, \varphi_i), \tag{6.6}$$

$$\mathbf{c}(\theta, \varphi) = [\sin\theta\sin\varphi, \sin\theta\sin\varphi, \cos\theta]^T, \tag{6.7}$$

where θ and φ are the polar and azimuthal angles, respectively, in the spherical coordinate system depicted at Fig. 6.1. The modeled system differentiates 32 beam directions in azimuth and 8 in elevation.

The transmit vector $\mathbf{t} \in \mathbb{C}^N$ is obtained by multiplying the precoding or steering matrix by the vector of transmitted symbols $\mathbf{s}$

$$\mathbf{t} = \mathbf{W}\mathbf{s}. \tag{6.8}$$

As the EMF exposure is further assessed in terms of the time-average root mean square (RMS) values, with no loss of generality we set all transmitted symbols to be real-valued and positive. In addition, we assume that no per-user power management is implemented at the BS and equal share of transmit power is directed to each UE. Therefore, we define $\mathbf{s} = [\sqrt{1/K}, \sqrt{1/K}, \ldots, \sqrt{1/K}]^T$. The normalization $\sqrt{1/K}$ is needed for the transmit vector $\mathbf{t}$ in (6.8) with $\mathbf{W}$ given by (6.2) or (6.4) to satisfy the overall transmit power constrain.

6.1.3 Time-average Antenna Array Patterns

An instantaneous array pattern is calculated as a sum of the patterns of its individual elements, weighted with the components of the transmit vector $\mathbf{t}$. As all antennas in the BS array are identical dipoles, this gives

$$A(\theta, \varphi, \mathbf{t}) = \sum_{n=1}^{N} A_{dip}(\theta, \varphi) t_n \exp(-2\pi i(\mathbf{d}_n, \mathbf{c}(\theta, \varphi))/\lambda), \tag{6.9}$$

where A_{dip} is a half-wave dipole radiation pattern [22], and t_n denotes the n^{th} element of $\mathbf{t}$. Here we do not account for the effect of mutual coupling in the antenna array, i.e. the modification of the free-space antenna element pattern by the currents in the neighboring elements.

In the far-field region of a BS, the incident EMF is proportional to the antenna gain in the direction where the measurement is preformed. As mentioned above, ICNIRP specifies [6] an EMF time-averaging interval $T_{avg} = 6$ min for the human exposure assessment. At the same time, it is foreseen that in a typical scenario 5G DL traffic will be transmitted in short bursts (in the order of tens of seconds [8]), switching between sets of UEs that demand it at any given moment. If the served UEs are distributed uniformly enough within the cell, the BS would focus the transmission in many different directions over a sufficiently long time interval.

Therefore, a *realistic* time-average BS antenna array gain is expected to differ significantly from the theoretical maximum one.

To quantify how much the time-averaged gain is reduced relative to the theoretical maximum we follow the approach proposed in [8, 10]. We introduce a constant T - the duration of one connection ('drop duration' in [10] or 'scheduling time' in [8]). We model a network in which independent sets of K UEs are served for time T in series with no overlaps. Then the time-average BS array radiation pattern $\tilde{A}_m^{N,K}(\theta,\varphi)$ is calculated as a weighted mean of the instantaneous patterns i produced during the averaging interval

$$\tilde{A}_m^{N,K}(\theta,\varphi) = \sum_i \omega_i A_m^{N,K}(\theta,\varphi,\mathbf{t}^i), \tag{6.10}$$

where $m \in \{CB, MRT, ZF\}$ denotes the transmission precoding scheme used at the BS; N, K are the number of utilized antenna elements and the number of simultaneously served UEs, respectively, and ω_i is the fraction of the averaging time during which pattern i was active, varying from 0 (not in the averaging interval) to T/T_{avg} (fully inside the averaging interval). In the following for convenience we choose T such that T_{avg} is its integer multiple, then $\omega_i = T/T_{avg}$. Next, the normalized gain $G_m^{N,K}$ is given by

$$G_m^{N,K}(T) = \frac{\max_{\theta,\varphi}\left[\tilde{A}_m^{N,K}(\theta,\varphi)\right]}{G_{max}^N}, \tag{6.11}$$

where G_{max}^N is the maximum gain of an array of N elements. The maximum gain of a planar antenna array is calculated as a product of the maximum antenna element gain and the maximum array factor. The maximum array factor equals to the number of elements in the array [23]. Therefore, for an antenna array composed of identical half-wave dipoles, $G_{max}^N = \max_{\theta,\varphi}[A_{dip}] \cdot N \simeq 1.64 \cdot N$. This value is further used in (6.11) as a normalization factor.

The RMS E-field strength at the location of the UE, to which $G_m^{N,K}$ would be directed, can be estimated using a free-space approximation according to the following expression

$$E_{RMS} = \frac{\cos(\pi - \theta_{max})}{h_{BS} - h_{UE}} \sqrt{\frac{ZPG_m^{N,K}G_{max}^N}{2\pi}}, \tag{6.12}$$

where θ_{max} is the polar angle of $G_m^{N,K}$, $Z \simeq 376$ Ohm is the impedance of free space, P is the BS total radiated power, and $h_{BS} = 25$ m and $h_{UE} = 1.5$ m are the BS and the UE height above the ground, respectively. For example, taking a BS with 64 antenna elements and 200 W nominal power [24], the highest achievable E_{RMS} ($G_m^{N,K} = 1$) in pure LOS path in the direction normal to the BS array plane ($\theta_{max} = 120°$) equals around 18.6 V/m, which falls below the ICNIRP reference level of 61 V/m [6].

To calculate $G_m^{N,K}(T)$ for given m, T, N, and K, a numerical experiment is performed. Figure 6.3 shows a flowchart describing the procedure.

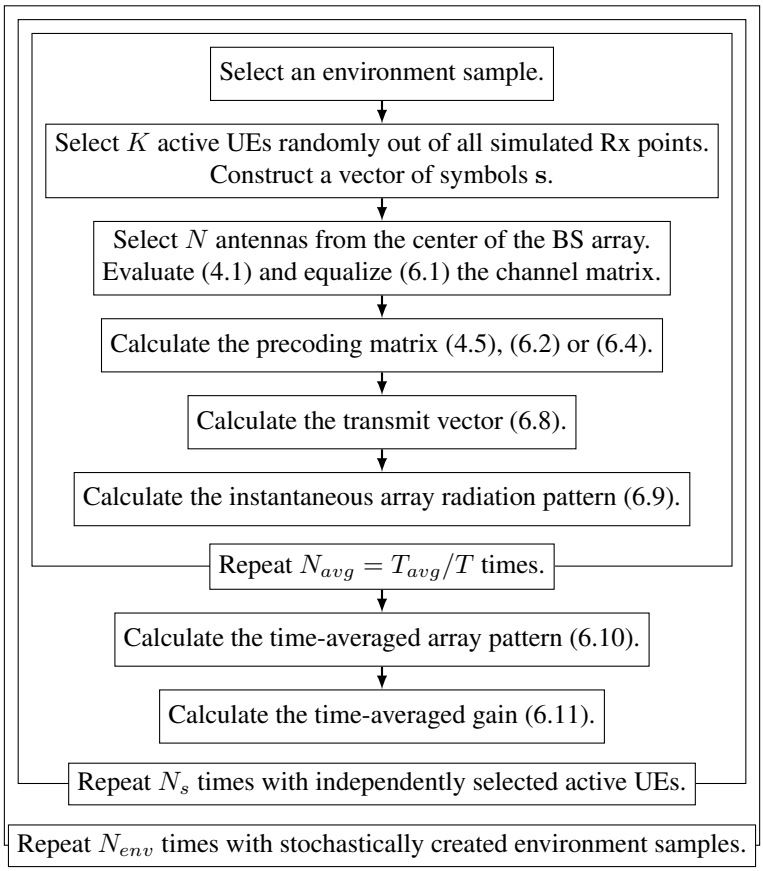

Figure 6.3: A flowchart of the procedure used to generate distributions of the time-averaged gain values $G_m^{N,K}(T)$. The complete procedure yields $N_{env} \cdot N_s$ time-averaged gain evaluations.

We studied configurations with 2-by-2, 4-by-4, 6-by-6, 8-by-8 square sub-arrays selected from the center of the simulated 10-by-10 Tx array, as well as the complete array itself. These correspond to total array counts N of 4, 16, 36, 64 and 100 elements. Scenarios with $K = 1$, 2, 5 and 10 simultaneously active UEs were studied for each N. Connection duration T_{avg} equal to 60 s, 10 s and 1 s was considered for each N and K. In total $N_{env} = 25$ environment samples were simulated. Including gain values obtained from the 25$^{\text{th}}$ sample were found to change the 95$^{\text{th}}$ percentiles of the time-averaged gain distributions by less than 1%, which was accepted as a sufficient level of accuracy. Finally, in every environment

sample $N_s = 100$ time-averaged gain evaluations were performed, which amounts to 2500 evaluations of $G_m^{N,K}(T)$ for each value of N, K, T and precoding scheme m. In the following section, the distributions of $G_m^{N,K}$ are presented and discussed.

6.2 Results

6.2.1 Average Array Patterns

Fig. 6.4 shows the DoDs of $G_{CB}^{N,5}$ (first column), $G_{MRT}^{N,5}$ (second column) and $G_{ZF}^{N,5}$ (third column), for $N = 4$ (first row), $N = 36$ (second row) and $N = 100$ (third row), calculated with a connection time $T = 60$ s. The DoD of each time-averaged gain sample is depicted with a black circle in the (φ, θ) coordinate system. The circle size is proportional to $G_m^{N,K}$, and its opacity is proportional to the number of samples observed at the corresponding DoD. The background pseudocolor plot shows the sample-average of $\tilde{A}_m^{N,K}(\theta, \varphi)$, illustrating the difference in the average beamwidths of the obtained patterns. $G_{ZF}^{4,5}$ is undefined, as the condition $N > K$ must be satisfied for $\mathbf{H}\mathbf{H}^H$ to be invertible, which is necessary to calculate G_{ZF} according to (6.2). Its plot was therefore not included in Fig. 6.4.

6.2.2 Normalized Gain

Fig. 6.5 shows the Cumulative Distribution Functions (CDFs) of $G_m^{N,K}$ in the layout matching that of Fig. 6.4. Each plot in Fig. 6.5 presents a CDF for $K = 1$ (black), $K = 2$ (red), $K = 5$ (blue) and $K = 10$ (green). In addition, the 95$^{\text{th}}$ precentile of each CDF is marked with a vertical dashed line of the same color. Table 6.1 lists the 95$^{\text{th}}$ percentiles for all possible combinations of the studied parameters. Additionally, the table cell background color saturation is proportional to its numerical value, ranging from white for zero to deep blue for one. This gives a visual cue to how different parameter combinations affect the normalized time-averaged gain.

6.3 Discussion

6.3.1 Array patterns for CB, MRT and ZF

The left column of Fig. 6.4 shows the DoD of the time-averaged gain observed when applying codebook precoding. The maximum value of the time-averaged array pattern was always found within the cell boundary. This was expected, as any instantaneous single-user codebook pattern has its main lobe pointing approximately towards an active UE, which was always situated within the cell. As a result of the linearity of (6.4), (6.8) and (6.9) with respect to the steering vector $\mathbf{b}$, the 6-min time-averaged pattern is expressed as an average of the instantaneous patterns

towards the UEs served during the averaging interval. The maximum of such averaged pattern was most likely to be found at the intersection of the instantaneous array patterns, i.e. somewhere within the cell. In the scenario with a 2-by-2 BS array (top-left), the maximum tends to be located around the cell center in azimuth. The reason for that is the low directivity of a typical pattern produced by an array of only 4 elements. For $N = 36$ (center-left), then the maxima distribution follows the average UE density peaks (Fig. 6.2), with two clusters that correspond to the lanes between the building blocks, parallel to the x-axis (Fig. 6.1). With 100 BS antenna elements (bottom-left), finally, the gain maxima closely follow the regions of high UE density (Fig. 6.2), nearly covering the full azimuth range of $120°$.

The center column of Fig. 6.4 shows the DoDs of the time-averaged gain found using MRT precoding. Similarly to CB, when the antenna count is low ($N = 4$, top-center plot), the maxima tend to be concentrated around the cell center. As N increases, G_{MRT} tends to be directed towards the regions densely occupied with the UEs with higher probability. However, MRT shows an increased spread of the gain DoD compared to CB. This can be attributed to the fact that unlike CB, which assigns a single beam per active UE, MRT superimposes a set of multiple beams with powers proportional to the contributions of the corresponding propagation paths to the total signal received by the UE. If a UE has a direct propagation path to the BS (i.e. LOS), the instantaneous MRT pattern is likely to have a global maximum in that direction (second strongest path - the ground reflection, if present, being orders of magnitude weaker). In case the target UE resides in a shadow region (NLOS), several propagation paths typically contribute comparable amounts to the total received signal. E.g. if a UE is obstructed by a building, the main propagation mechanisms that make the connection possible are over-the-rooftop diffraction and reflections from the walls of the surrounding buildings. As a result, the time-average pattern maximum is sometimes found *outside* the cell boundary, as can be seen on the plots showing $G_{MRT}^{36,5}$ (center-center) and $G_{MRT}^{100,5}$ (bottom-center) in Fig. 6.4.

This effect is even more pronounced when ZF precoding was used, although the underlying reason is different. ZF minimizes interference between the target UEs by canceling the transmission via shared paths. In scenarios with a large number of spatially correlated UEs, a portion of the total transmit power dedicated to fighting interference may exceed that of the intended signal, i.e., an instantaneous ZF pattern can have higher gain in its side-lobes than in the beams intended to reach the UEs. Such effect is observed in the DoD distribution of $G_{ZF}^{36,5}$ (center-right) in Fig. 6.4. In the areas with the highest UE density, where both CB and MRT generally produced their time-average gain maxima most often, ZF showed very few time-average array pattern peaks. The ZF precoding efficiency generally increases with the N/K ratio [4]. For $N = 100$ the gain distribution (bottom-right) was similar in shape to what was obtained using MRT, although the spread of the gain locations noticeably exceeded both MRT and CB.

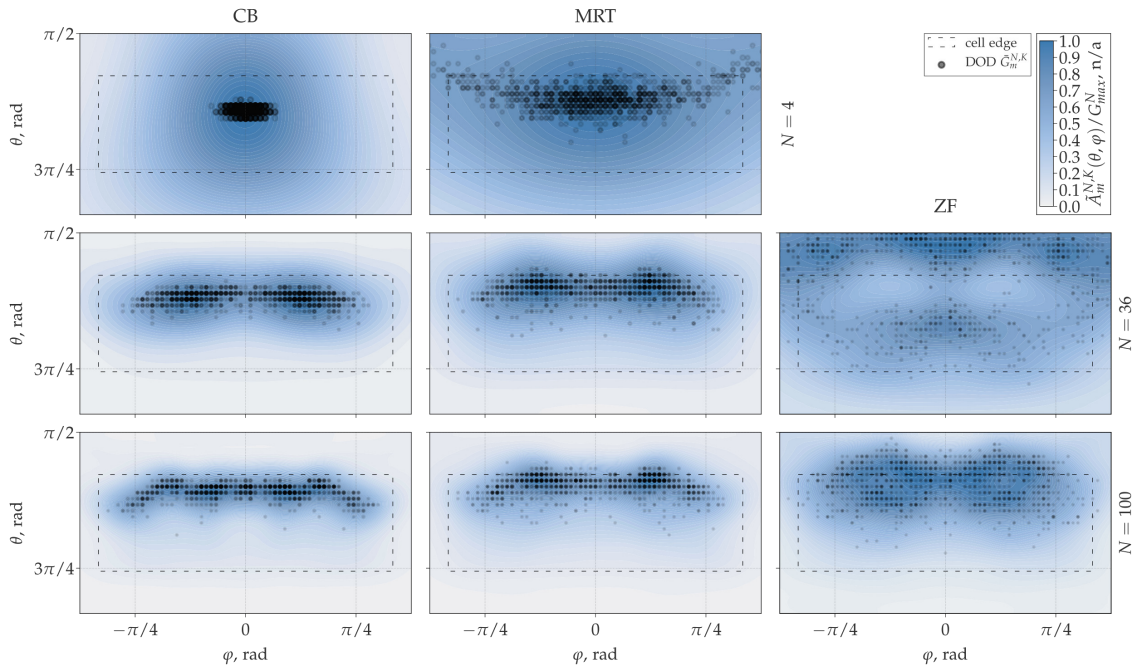

Figure 6.4: DoD (φ, θ) of the maxima of the time-averaged BS array patterns as observed over 2500 cases (100 simulations with randomly distributed UEs in 25 different environment samples) when serving $K = 5$ UEs simultanously, with connection time $T = 60$ s. Each maximum direction is marked with a black circle. The circle size is proportional to the corresponding value of the time-averaged maximum gain (normalized to the maximum of all samples of the respective parameter combination). The circle opacity is proportional to the number of maxima found in the corresponding (φ, θ) direction. Left, center, and right columns show data for CB, MRT, ZF transmission schemes, respectively. In the first, second, and third rows scenarios with 2-by-2, 6-by-6, and 10-by-10 base station arrays are depicted. The ZF transmission with 2-by-2 BS array ($N = 4$) is undefined and was omitted. The dashed line depicts the cell boundary. The normalized time- and sample-averaged BS array patterns are shown in blue.

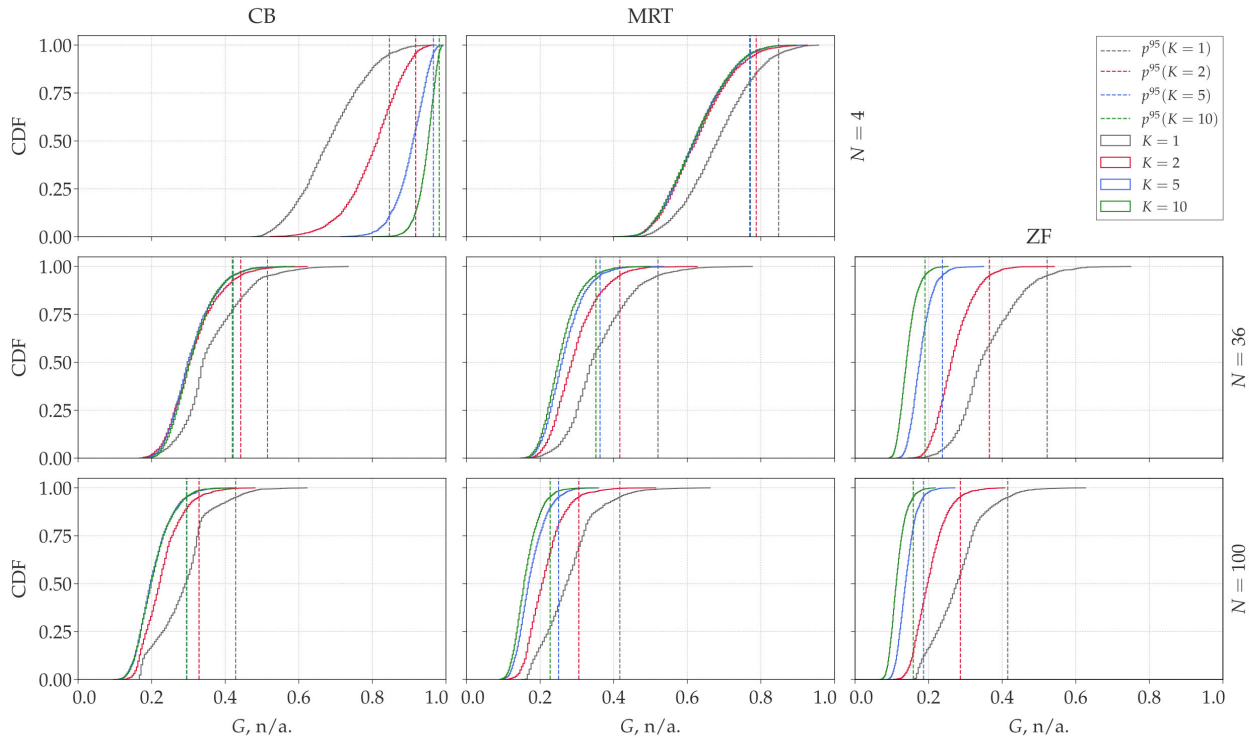

Figure 6.5: CDFs of the normalized 6 min average BS array gain $G_{CB}^{N,K}$ (first column), $G_{MRT}^{N,K}$ (second column), $G_{ZF}^{N,K}$ (third column) with $T = 60$ s. Scenario with base station array size $N = 4$, 36 and 10 are shown in the first, second and third row, respectively. Solid lines show CDFs for the number of simultaneously active UEs $K = 1$ (black), $K = 2$ (red), $K = 5$ (blue) and $K = 100$ (green). Dashed lines of matching color mark the 95$^{\text{th}}$ percentile of each distribution.

6.3.2 Normalized time-averaged gain

The CDFs in Fig. 6.5 compare the $G_m^{N,K}$ values for parameter configurations that correspond to those shown in Fig. 6.4. Increasing the BS antenna count N decreases the normalized time-averaged gain for all studied schemes, with other parameters fixed. Two factors are contributing to this effect. First, the normalization coefficient in (6.11) is proportional to N, which counteracts the increase in the absolute array gain. Second, with larger N the BS is capable of producing narrower beams, which are less likely to interlap in the DoD region within the cell, reducing the maximum of the average taken according to (6.10).

Decreasing the connection time T also decreases the time averaged gain, that is $G_m^{N,K}(T = 60\ s) > G_m^{N,K}(T = 10\ s) > G_m^{N,K}(T = 1\ s)$ for any fixed m, N or K. This observation is explained by the fact that the more independent UE sets are served in the averaging time-span T_{avg} (or, equivalently, the less the T value is), the closer $G_m^{N,K}$ approaches the normalized average of instantaneous array patterns $A(\theta, \varphi, \mathbf{t})$ over the cell. Conversely, in the limit of a single UE served with $T = T_{avg}$, as follows from (6.9), (6.10), (6.11), the time-averaged gain is the instantaneous BS pattern maximum. In this case, the CB beamforming realizes the maximum theoretical gain G_{max} for the codebook directions coinciding with the maxima of the BS antenna element's individual pattern. This can be seen by substituting $\mathbf{t} = \mathbf{b}_k$ into (6.9), assuming that the beam center DoD satisfies $(\theta_k, \varphi_k) = \arg\max_{\theta,\varphi}[A_{dip}]$.

When only a single UE is connected at a time ($K = 1$, shown in black in Fig. 6.5), CB, MRT, and ZF show very similar distributions of the normalized gain. In fact, as can be seen from (6.2) in the degenerate case of $K = 1$, the matrix inverse of $\mathbf{H}\mathbf{H}^H$ becomes a reciprocal of a squared channel coefficient magnitude. The ZF and MRT formulations are then equivalent, with appropriately chosen normalization coefficients α in (6.2). The minor discrepancy in Table 6.1 between the MRT and ZF ($< 1\%$) for $K = 1$ is due to the numerical round-off error propagation. The difference between $G_{MRT}^{N,1}$ and $G_{CB}^{N,1}$, gradually increases with increasing N and decreasing T. Both $G_{MRT}^{4,1}$ and $G_{CB}^{4,1}$ are decreasing monotonously from around 0.85 for $T = 60$ s to around 0.66 for for $T = 1$ s (see Table 6.1). At $N = 100$, $G_m^{N,1}$ drops rapidly to around a half of that ($\simeq 0.42$ for CB) for $T = 60$ s, around a third ($\simeq 0.22$ for MRT) for $T \simeq 10$ s and less than a quarter ($\simeq 0.15$ for MRT) for $T = 1$ s.

Increasing the number of simultaneously served UEs K was found to decrease $G_{MRT}^{N,K}$ and $G_{ZF}^{N,K}$ for any fixed N and T. Increasing K decreased $G_{CB}^{N,K}$ only for larger BS arrays ($N \geq 16$) for $T = 60$ s, and led to its increase with any N for shorter connection time values. For $N = 4$, the CB time-averaged gain closely approached the theoretical maximum for any T and $K \geq 5$ ($G_{CB}^{N,K} \geq 0.9$). This indicates that smaller BS antenna arrays implementing CB beamforming offer little to no benefit in terms of human EMF exposure reduction.

Scheme		**CB**					**MRT**					**ZF**			
K \ N		4	16	36	64	100	4	16	36	64	100	16	36	64	100
$T = 60$ s	1	0.85	0.63	0.51	0.46	0.43	0.85	0.63	0.52	0.47	0.42	0.63	0.52	0.46	0.42
	2	0.92	0.58	0.44	0.37	0.33	0.79	0.53	0.42	0.35	0.31	0.44	0.37	0.32	0.29
	5	0.97	0.57	0.42	0.35	0.29	0.77	0.49	0.36	0.30	0.25	0.29	0.24	0.21	0.19
	10	0.98	0.55	0.42	0.34	0.30	0.77	0.48	0.35	0.27	0.23	0.27	0.19	0.17	0.16
$T = 10$ s	1	0.70	0.40	0.29	0.24	0.20	0.71	0.42	0.31	0.25	0.22	0.42	0.31	0.26	0.21
	2	0.83	0.40	0.27	0.21	0.17	0.66	0.38	0.27	0.22	0.19	0.31	0.24	0.19	0.17
	5	0.92	0.42	0.28	0.22	0.18	0.65	0.36	0.27	0.20	0.16	0.20	0.15	0.13	0.11
	10	0.96	0.44	0.31	0.24	0.20	0.64	0.36	0.25	0.19	0.16	0.18	0.11	0.10	0.09
$T = 1$ s	1	0.66	0.32	0.21	0.17	0.13	0.67	0.36	0.26	0.20	0.15	0.35	0.25	0.19	0.16
	2	0.80	0.32	0.21	0.16	0.13	0.60	0.34	0.24	0.19	0.15	0.26	0.20	0.16	0.14
	5	0.90	0.37	0.25	0.18	0.14	0.60	0.33	0.23	0.18	0.14	0.16	0.12	0.10	0.09
	10	0.95	0.42	0.29	0.21	0.18	0.59	0.32	0.23	0.18	0.14	0.14	0.09	0.08	0.06

Table 6.1: Summary of the 95$^{\text{th}}$ percentiles of G_{CB}, G_{MRT}, and G_{ZF} for $T \in \{60\text{ s}, 10\text{ s}, 1\text{ s}\}$, $K \in \{1, 2, 5, 10\}$ and $N \in \{4, 16, 36, 64, 100\}$. The background color saturation is proportional to its numerical value, ranging from white for zero to deep blue for one.

In a realistic usage scenario, take $T \simeq 10$ s [8]. If the BS is equipped with 64 antenna elements, p^{95} of $G_{CB}^{64,K}$ is just above 0.2 (around 7 dB reduction) for any K. This is in agreement with the results in [10] obtained with a similar configuration in the outdoor macrocell environment. Direct comparison with [8] is not possible, as in that case the UE count was varied during the averaging time. Increasing the averaging time T to 60 s increases the 95$^{\text{th}}$ percentile of $G_m^{64,5}$ to 0.35 (4.6 dB) for CB, 0.30 (5.2 dB) for MRT and 0.21 (6.8 dB) for ZF.

Adding more BS antenna elements while using either the CB or MRT scheme, does not decrease $G_m^{N,K}$ significantly. Their lowest 95$^{\text{th}}$ percentile values were observed for $T = 1$ s: $G_{MRT}^{100,5} \simeq G_{MRT}^{100,10} \simeq 0.14$ and $G_{CB}^{100,1} \simeq G_{CB}^{100,2} \simeq 0.13$. The 95$^{\text{th}}$ percentiles of $G_{ZF}^{N,K}$ were lower than the respective $G_{MRT}^{N,K}$ and $G_{CB}^{N,K}$ values for all $K \geq 2$. This difference was larger with for larger K and shorter connection time T. In the realistic scenario with $T = 10$ s, the 95$^{\text{th}}$ percentiles of $G_{ZF}^{64,K}$ were equal to around 0.19 (7.2 dB), 0.13 (8.9 dB) and 0.1 (10 dB) for $K = 2,\ 5,$ and 10, respectively. These values are nearly two times lower that the MRT and CB schemes demonstrated in the same parameter configurations. The lowest p^{95} was found with $G_{ZF}^{100,10} \simeq 0.06$ (12.2 dB), which is around one third of the corresponding CB value, and more than two times lower than the minimum for the MRT or CB scheme.

As the time-averaged gain is directly related the average E_{RMS} measured at some location in the cell. The far-field instantaneous E-field magnitude is proportional to the square root of the antenna gain. Therefore, the time-averaged E_{RMS} is reduced at least in proportion to the square root of the time-averaged gain $G_m^{N,K}$, relative to the E_{RMS} estimate based on the maximum achievable gain G_{max}^{N}. In a scenario with $N = 64$, $K = 5$ and $T = 10$ s, this leads to the E-field reduction in 95% of the observations by at least a factor of around 2.1 (3.2 dB), 2.2 (3.4 dB) and 2.8 (4.5 dB) for the CB, MRT and ZF schemes, respectively, compared to the theoretical maximum. The theoretical maximum gain value was never reached in samples with $K \geq 5$.

6.4 Conclusions

A numerical approach that utilizes the RT method to model a time-averaged array gain of a 5G BS operating in a macrocell outdoor urban environment was presented. The RT approach provides a more realistic signal propagation and user spatial correlation properties compared to analytical and stochastic approaches. In a realistic scenario, with a BS consisting of 64 antenna elements that serves 5 UEs simultaneously and a 10 s per-user connection duration, 95% of the 6-minute time-average gain observations fell below 0.22 (more than 6.6 dB reduction), 0.20 (7 dB) and 0.13 (8.9 dB) of the theoretical maximum, using codebook beamforming, Maximum Ratio Transmission, and Zero-Forcing schemes, respectively. With user

connection duration of 60 s, the corresponding 95$^{\text{th}}$ percentiles increase to 0.35 (4.6 dB), 0.30 (5.2 dB) and 0.21 (6.8 dB), respectively. In all studied scenarios, increasing the BS element count decreased the normalized time-average gain. With the MRT and ZF transmission schemes, lower time-averaged gain was always observed when the number of multiplexed UEs was increased. With the CB beamforming that was the case only for larger BS arrays. In all multi-user scenarios, the ZF yielded the lowest p^{95} values of the normalized time-average gain (0.06 or 12.2 dB reduction with 100 BS antennas and 10 UEs), which is more than two times lower than any other studied precoding scheme.

This chapter concludes the numerical investigation of the massive MIMO exposure. One of the shared foundations of all simulations presented in Chapters 3 to 5 was the propagation prediction and channel matrix calculation using the RT method. Crucially, the amount of correlation in the channel vectors observed at closely-spaced receiver locations is one of the key properties, that can be directly linked to the hot-spot size (on a small scale) and the BS ability to multiplex UEs (at a larger scale). In the next chapter we will validate the RT approach by comparing the channels measured with a real massive MIMO test-bed to the simulated ones. Similar stochastic geometry elements used throughout the last four chapters will once again be applied to the environment modeling, which will give experimental basis to the obtained exposure results.

References

[1] Paolo Bernardi, Marta Cavagnaro, Stefano Pisa, and Emanuele Piuzzi. *Human exposure to radio base-station antennas in urban environment*. IEEE transactions on microwave theory and techniques, 48(11):1996–2002, 2000.

[2] Justin Cooper, Bernd Marx, Johannes Buhl, and Volker Hombach. *Determination of safety distance limits for a human near a cellular base station antenna, adopting the IEEE standard or ICNIRP guidelines*. Bioelectromagnetics: Journal of the Bioelectromagnetics Society, The Society for Physical Regulation in Biology and Medicine, The European Bioelectromagnetics Association, 23(6):429–443, 2002.

[3] Arno Thielens, Günter Vermeeren, Divya Kurup, Wout Joseph, and Luc Martens. *Compliance boundaries for multiple-frequency base station antennas in three directions*. Bioelectromagnetics, 34(6):465–478, 2013.

[4] Thomas L. Marzetta, Erik G. Larsson, Hong Yang, and Hien Quoc Ngo. *Fundamentals of massive MIMO*. Cambridge University Press, 2016.

[5] International Commission on Non-Ionizing Radiation Protection et al. *Guidelines for limiting exposure to Electromagnetic Fields (100 kHz to 300 GHz)*. Health Physics, 118(5):483–524, 2020.

[6] International Commission on Non-Ionizing Radiation Protection et al. *ICNIRP Guidelines for Limiting Exposure To Time-Varying Guidelines for Limiting Exposure To Time-Varying Electric, Magnetic and Electromagnetic fields*. Health Phys, 74:494–522, 1998.

[7] Björn Thors, Arno Thielens, Jonas Fridén, Davide Colombi, Christer Törnevik, Günter Vermeeren, Luc Martens, and Wout Joseph. *Radio frequency electromagnetic field compliance assessment of multi-band and MIMO equipped radio base stations*. Bioelectromagnetics, 35(4):296–308, 2014.

[8] Björn Thors, Anders Furuskär, Davide Colombi, and Christer Törnevik. *Time-averaged realistic maximum power levels for the assessment of radio frequency exposure for 5G radio base stations using massive MIMO*. IEEE Access, 5:19, 2017.

[9] Bo Xu, Davide Colombi, Christer Törnevik, Fatemeh Ghasemifard, and Jiajia Chen. *On Actual Maximum Exposure From 5G Multi-Column Radio Base Station Antennas*. 2020.

[10] Paolo Baracca, Andreas Weber, Thorsten Wild, and Christophe Grangeat. *A Statistical Approach for RF Exposure Compliance Boundary Assessment in*

Massive MIMO Systems. In WSA 2018; 22nd International ITG Workshop on Smart Antennas, pages 1–6. VDE, 2018.

[11] Hien Quoc Ngo. *Massive MIMO: Fundamentals and System Designs*. 2015.

[12] Bishwarup Mondal, Timothy A Thomas, Eugene Visotsky, Frederick W Vook, Amitava Ghosh, Young-Han Nam, Yang Li, Jianzhong Zhang, Min Zhang, Qinglin Luo, et al. *3D channel model in 3GPP*. IEEE Communications Magazine, 53(3):16–23, 2015.

[13] David Löschenbrand, Markus Hofer, Benjamin Rainer, and Thomas Zemen. *Empirical and Simulated Performance Evaluation of Distributed Massive MIMO*. In 2019 53rd Asilomar Conference on Signals, Systems, and Computers, pages 952–956. IEEE, 2019.

[14] Mehmet Mert Taygur and Thomas F Eibert. *Investigations on Massive MIMO Performance with Multi-Antenna Users by Ray-Tracing*. In 2019 IEEE 30th Annual International Symposium on Personal, Indoor and Mobile Radio Communications (PIMRC), pages 1–6. IEEE, 2019.

[15] Kapil Bhardwaj, Anant Singh, and Vibhav Kumar Sachan. *5G: An overview of Channels characteristics and modelling techniques*. In 2018 Fifth International Conference on Parallel, Distributed and Grid Computing (PDGC), pages 400–405. IEEE, 2018.

[16] Jonas Medbo, Pekka Kyosti, Katsutoshi Kusume, Leszek Raschkowski, Katsuyuki Haneda, Tommi Jamsa, Vuokko Nurmela, Antti Roivainen, and Juha Meinila. *Radio propagation modeling for 5G mobile and wireless communications*. IEEE Communications Magazine, 54(6):144–151, 2016.

[17] Greg Durgin, Neal Patwari, and Theodore S Rappaport. *An advanced 3D ray launching method for wireless propagation prediction*. In Vehicular Technology Conference, 1997, IEEE 47th, volume 2, pages 785–789. IEEE, 1997.

[18] Sergei Shikhantsov, Arno Thielens, Günter Vermeeren, Piet Demeester, Luc Martens, Guy Torfs, and Wout Joseph. *Massive MIMO Propagation Modeling With User-Induced Coupling Effects Using Ray-Tracing and FDTD*. IEEE Journal on Selected Areas in Communications, 38(9):1955–1963, 2020.

[19] Georgia E Athanasiadou and Andrew R Nix. *Investigation into the sensitivity of the power predictions of a microcellular ray tracing propagation model*. IEEE transactions on Vehicular Technology, 49(4):1140–1151, 2000.

[20] Jialai Weng, Xiaoming Tu, Zhihua Lai, Sana Salous, and Jie Zhang. *Indoor massive MIMO channel modelling using ray-launching simulation*. International Journal of Antennas and Propagation, 2014, 2014.

[21] Hamid Krim and Mats Viberg. *Two decades of array signal processing research: the parametric approach*. IEEE signal processing magazine, 13(4):67–94, 1996.

[22] Simon R. Saunders. *Antennas and Propagation for Wireless Communication Systems*. John Wiley & Sons, Inc., New York, NY, USA, 1st edition, 1999.

[23] Wolfgang H Kummer. *Basic array theory*. Proceedings of the IEEE, 80(1):127–140, 1992.

[24] Ericsson. *Antenna Integrated Radio Unit Description AIR 6488*.

Part III

Experimental validation

7

Massive MIMO Test-Bed Measurements

7.1 Introduction

This chapter provides the experimental evidence to support the results of the massive MIMO simulations presented in Chapters 3 to 6. Measuring psSAR_{10g} directly is technically challenging, as a complex setup including a phantom (filled with tissue-simulating liquid) and a high-precision 3D-positioning system equipped with a calibrated EMF probe is required. To measure the EMF in free space (e.g. in the hot-spot around a receiver), a compact in size (to approach the receiver close enough) and at the same time highly-sensitive EMF probe is needed. In addition, the movement of the probe might significantly disturb the channel estimate at the massive MIMO base station, which in turn alters the hot-spot EMF being measured. An alternative to these approaches is to utilize the BS estimates of the channel to the receiver, the position of which is controlled with precision, to indirectly evaluate the hot-spot EMF distribution. A large number of elements in the BS array and precoded transmission ensure that the EMF strength decreases with distance from the intended receiver, as the observed channel vector becomes less and less similar to the one at the initial location. The rate at which the correlation between two channel vectors decreases with the distance between the corresponding receiver locations, determines the size of the hotspot.

The correlation properties at the transmitter (Tx) side are studied extensively in the literature from analytical [1] and experimental [2] standpoints. The Rx side

received less attention so far. Relevant information can be found in [3], where performance of a wireless power harvesting beacon was studied. From these results, we estimate the hotspot cross-section radius to be around 0.3 m, or 3 wavelengths at 2.6 GHz and 1.6 m Tx-Rx separation distance. In Chapters 3 to 5 (see also [4, 5]) the hot-spot power density distribution was modeled as an interference pattern of a large number of plane-waves incident at the Rx. The hot-spot size almost never exceeded 1 wavelength (86 mm) at 3.5 GHz. Relevant results are found in the COST 2100 model [6] study of the temporal autocorrelation function of moving users in LOS 64-antenna element massive MIMO channels at 2.6 GHz. The correlation coefficient rapidly dropped to around 0.5 at a distance of approximately 0.1 m (1λ), and remained at the same level at larger distances. In [7], scalar products of channel vectors measured at 5.8 GHz are reported for users in LOS at approximately 15 m distance from a 64-element BS. The scalar product was around 0.4 for 0.2 m (4λ) between users and dropped to nearly 0.2 at 1 m (20λ).

This chapter presents the study of the spatial correlation properties of Massive MIMO at the Rx side, comparing measured and simulated channels. The measurements were conducted using a Massive MIMO test-bed with 64 elements [2, 8] (KU Leuven, Belgium), operating at the center-frequency of 2.61 GHz. The simulations were performed using the Ray-Tracing (RT) method in a synthetic environment, approximating the one in which the measurements were taken. The main goal of this chapter is the validation of the Ray-Tracing approach for prediction of the correlation properties of Massive MIMO channels.

In addition, to evaluate the multipath contribution we studied pure line-of-sight (LOS) channels, derived from the RT simulations. The effect of the environment on the correlation profile was quantified by comparing the LOS and measured channels at different distances from the BS. The power ratios of LOS and diffuse fractions of the RT channels were analyzed at different distances from the BS to explain how the environment alters the correlation profile.

7.2 Materials and methods

7.2.1 Measurements

A top view of the measurement setup is shown schematically (to scale) at Fig. 7.1a. The KU Leuven massive MIMO testbed is a TDD-LTE based system controlled by the MIMO Application Framework of National Instruments, with a center frequency of 2.61 GHz. The testbed comprises two parts, the BS and user equipment (Rx). The BS is equipped with $N = 64$ dual-band patch antennas, located as a planar array of 8-by-8 elements. For the user equipment a single dipole antenna is used per data stream. The BS parameters are summarized in Table 7.1. The center of the BS array is located at $x = 5$ m, $y = 0$ m, $z = 1$ m in the coordinate system

Name	Element # (N)	Frequency	Subcarrier #	Bandwidth
Value	64	2.61 GHz	100	20 MHz

Table 7.1: Parameters of the KU Leuven massive MIMO test-bed.

depicted in Fig. 7.1a.

Two pairs of Rx antennas, (Rx_1^l, Rx_1^r) and (Rx_2^l, Rx_2^r) in Fig. 7.1a, are each mounted on a positioning system 2.2 m and 3.5 m shortest distance from the plane of the BS, 0.3 m above the ground. The positioning systems are controlled from the operator's center (Fig. 7.1a). Simultaneously, they move the Rx antennas parallel to the y-axis. Rx_1^l and Rx_2^l are moved from $y = 1.45$ m to $y = 0.17$ m, and Rx_1^l and Rx_2^l are moved from $y = -0.17$ m to $y = -1.45$ m (1.28 m of movement range for each Rx). This receiver arrangement was chosen to collect channel samples in the left (upper index l) and right (upper index r) half-space of the BS array symmetrically. In the following sections we evaluate how much the deviation from symmetry in the measurement environment influences the absolute channel values and their correlation properties. After each 10 mm traveled, the positioners halt the motion for 10 s to allow the BS control unit (CU) to record enough channel state samples, resulting in $K = 129$ fixed positions per Rx. The positioners report the local coordinates of each halted Rx and the Network Time Protocol (NTP) timestamp [9] at the moment it arrives at the location.

The BS CU records the complex channel coefficients of each Tx-Rx pair at every subcarrier frequency and the NTP timestamps of the measurements. This procedure is carried out simultaneously for all Rx antennas with a sample rate of approximately 1.3 sample per second.

The wireless channel between each UE dipole antenna and the 64 antennas at the BS is recorded as $H \in \mathbb{C}^{M \times F}$, where $M = 64$ is the number of the BS antennas, and $F = 100$ is the number of subcarrierrs.

Fig. 7.2 shows the channel coefficients' $(h_{j,0}^i)$ absolute values measured at one of the BS elements (with index 0) for 16 consecutive fixed Rx positions. Red and green colors in Fig. 7.2 show channels to Rx_j^l and $Rx_j^r, j \in \{1, 2\}$, respectively. Lines depict the channel magnitudes for the sub-carrier with the center-frequency of 2.61 GHz, and the shaded regions show the minimum-maximum range across all sub-carriers. Solid dots mark the channel values at the NTP timestamps which have the smallest time difference with the timestamps reported by the positioning system.

The channel magnitude shows a staircase-like behavior - periods with relatively stable values are followed by abrupt jumps, forming an alternating pattern. The stable periods correspond to the time instances when the Rx antennas are static and the channel variation is caused by thermal noise or changes in the environment. Rapid jumps of the channel always occur when the Rx antennas are moved from one

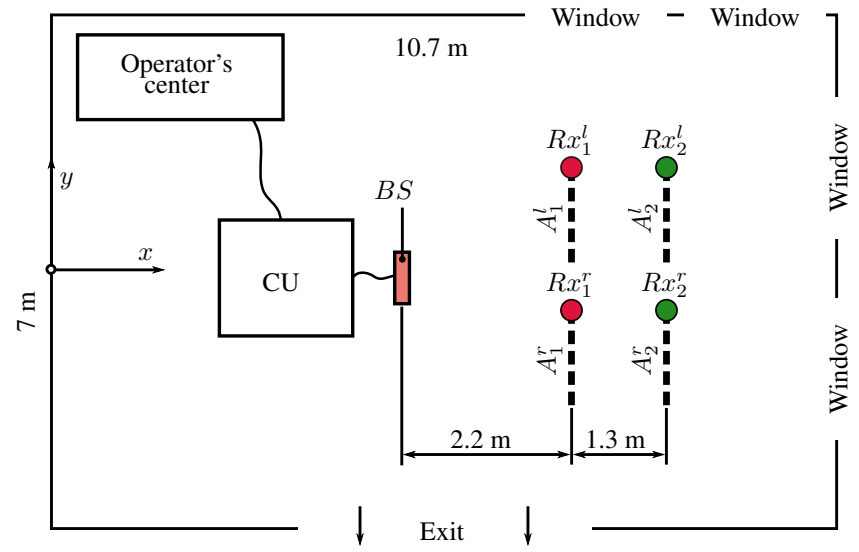

(a)

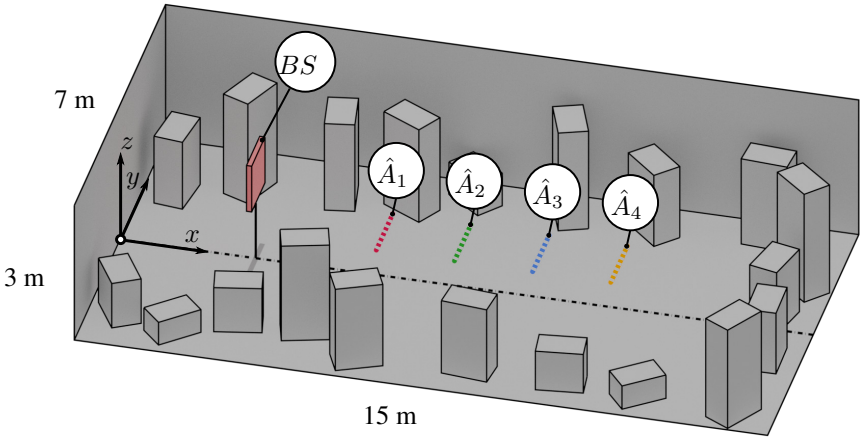

(b)

Figure 7.1: a) Top view of the measurement environment. The BS is shown with a red rectangle, two Rx tracks are shown with dashed lines. b) RT environment sample. The BS is shown with a pink box, while the dashed colored lines indicate the locations of $A_i, i \in \{1, 2, 3, 4\}$ in the simulation.

stationary location to another. This can be seen from the positioner NTP timestamps Fig. 7.2 (marked with solid dots) which follow these jumps.

It should also be noted that none of the channel sample series are correlated between receivers (absolute value of the Pearson's correlation coefficient ≤ 0.02.), which is expected, as Rx are separated by over 1 m (around 7λ) distance at any time-instance. The inter-subcarrier correlation decreases monotonously with frequency and its average over all BS elements and Rx locations drops to around 0.15 over the complete frequency band (20 MHz). The channel coefficient variation across the subcarriers is significant, as can be seen from Fig. 7.2. The amount of time it takes for the Rx to be moved from one stationary position to another is below 0.5 s and at most a single channel sample can be measured by the BS CU during this time period. These samples are undesirable and therefore excluded from further analysis.

Each stationary Rx position is treated as an element of a virtual array of receivers with channel matrices $H_j^i \in \mathbb{C}^{N\times K}, j \in \{1,2\}, i \in \{l,r\}$. The matrix element $h_{j,kn}^i$ of H_j^i is then defined as the arithmetic mean of the channel coefficient samples measured between the BS element n and the Rx_j^i at the location k. The average relative standard error of both real and imaginary parts of $h_{j,kn}^i$ (ripple of the channel samples with stationary Rx) is around 3% and is much smaller than its variation across the subcarriers.

7.2.2 Ray-Tracing

The RT simulations were conducted with the Wireless InSite 3.3 (REMCOM) software suite. Environment geometry, dielectric material properties, transmitter (Tx) and receiver (Rx) positions are the input for the RT solver at 2.61 GHz.

7.2.2.1 Model of the environment

A simplified model of the measurement site is constructed. The reason for such simplification is twofold. First, low polygon count of the RT geometry saves computational resources and speeds up the simulation. Second, this allows to determine whether key massive MIMO channel properties can be accurately reproduced by using an approximate representation of the environment, similar to the ones studied in chapter 3 and **??????**.

The complete RT geometry is contained within a single cuboid (the floorplan). A dielectric material with parameters $\varepsilon_r = 7,\ \sigma = 1.5 \cdot 10^{-2}$ S/m was assigned to its walls, floor and ceiling (concrete material model). Its sides are aligned with the coordinate axes. In addition, scatterers are distributed randomly inside the floorplan to diversify the propagation process. The scatterers are non-intersecting cuboids of a fixed footprint. Their centers are positioned in the horizontal plane using the Poisson Disc Sampling algorithm [10] inside the room. Each scatterer is rotated around the vertical axis, that passes through its center, at an angle, sampled independently from the uniform distribution in $[0, 2\pi]$. After the positions of all

scatterers have been determined, those that are not contained within a given distance from any wall are discarded. A geometry with defined scatterer positions is further referred to as *environment sample*.

One of the simulated environment samples is depicted in Fig. 7.1b. The coordinates of the BS center and relative positions of its antenna elements match those used during the measurements. The Rx arrays are shown with solid colored lines in Fig. 7.1b. The $\hat{A}_1$ and $\hat{A}_2$ arrays have the same coordinates as the measured A_1^l and A_2^l. The $\hat{A}_3$ and $\hat{A}_4$ arrays have the same y and z coordinates, but are shifted along the x-axis to $x = 9.8$ m and $x = 11.1$ m, respectively. Indexed this way, the larger the index of an array, the larger the distance of this array from the BS.

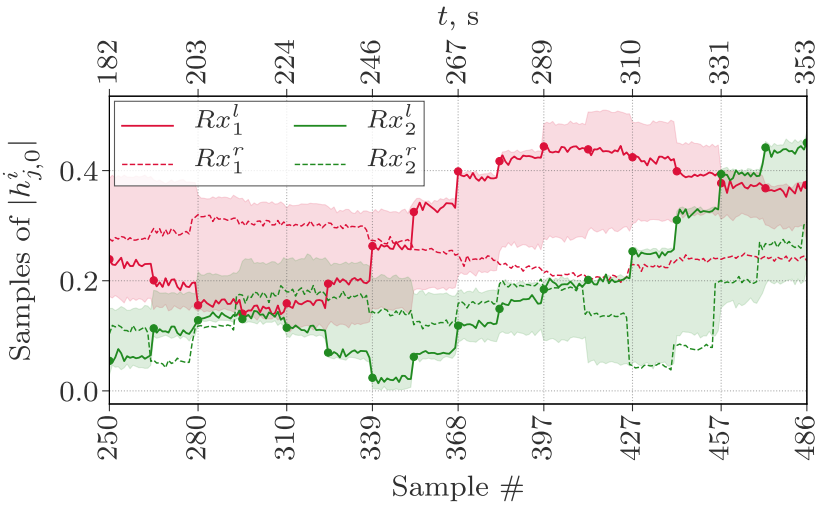

Figure 7.2: Channel magnitudes at the first BS element (2.61 GHz subcarrier) as the Rx antennas pass through 16 stationary locations are shown with solid and dashed lines. Bottom axis tracks the channel sample number, top axis - time since the first measured sample. Shaded regions show the channel magnitude $\min - \max$ range across all 100 subcarriers. Channels of Rx_1 and Rx_2 are shown in red and green, respectively.

The y and z dimensions of the room are equal to the corresponding dimensions of the measurement site (7 m and 3 m, respectively). The room size in the x direction was extended to 15.5 m (compared to 10.7 m of the measurement site), in order to fit the A_3 and A_4 arrays into the simulation domain. All geometric entities are assigned identical dielectric properties $\varepsilon_r = 7,\ \sigma = 1.5 \cdot 10^{-2}$ S/m, modeling concrete material [11].

Vertically polarized half-wave dipole patterns are assigned to the antennas of all BS array elements and receivers. The RT simulations are narrow-band, that is, transmitters are excited with a continuous sinusoidal signal. The RT simulations were

carried out at a single frequency $f_c = 2.61$ GHz (the test-bed center frequency).

7.2.2.2 Channel matrix calculation

The ray-tracer calculates the channel coefficient between the n^{th} BS antenna element and k^{th} Rx location as

$$\hat{h}_{j,kn} = \sum_{r \in s_j(n,k)} u_r \exp(-2\pi i f_c \tau_r), \tag{7.1}$$

where j is the virtual array index, $s_j(n,k)$ is the set of indices of rays found for the (n,k) Tx-Rx pair, u_r is the amplitude of the voltage induced by the ray r at the Rx antenna terminal and τ_r is the time-of-flight of the ray r. The RT channel matrix $\hat{H}_j$ is obtained by evaluating (7.1) for each Tx-Rx pair in the BS and the A_j.

7.2.3 Free-Space Line-of-Sight model

It is possible to modify (7.1), such that only the direct paths between the Tx-Rx pairs are accounted for. Replacing $s_j(n,k)$ with the LOS ray $r_{j,kn}^{LOS}$ (the LOS path exists for all Rx locations in the studied scenario), we obtain the Free-Space LOS (FS-LOS) channel coefficients

$$h_{j,kn}^{\rightarrow} = u_r \exp(-2\pi i f_c \tau_r)|_{r_{j,kn}^{LOS}}, \tag{7.2}$$

that form the channel matrix $H_j^{\rightarrow}$.

7.2.4 Channel equalization

To exclude the effect of the Path Loss (PL) we equalize the channel vectors. This is achieved by multiplying the channel matrix by the vector of its inverse column norms. For any channel matrix H,

$$\bar{H} = [\|\mathbf{h}_0\|^{-1}, \|\mathbf{h}_1\|^{-1}, \ldots, \|\mathbf{h}_K\|^{-1}]H, \tag{7.3}$$

where $\mathbf{h}_k = [h_{k0}, h_{k1}, \ldots, h_{kN}]^T$ is the k^{th} channel vector.

Equalization (7.3) removes the channel magnitude variation, but preserves the BS antenna amplitude and phase ratios.

7.2.5 Spatial correlation function

The equalized channel correlation matrix is defined using the equalized channels as

$$G = \bar{H}\bar{H}^{*T}. \tag{7.4}$$

As $g_{kk} = \bar{h}_k \bar{h}_k^{*T} = \|\bar{h}_k\| = 1$, any diagonal element of G equals to unity, as a norm of the equalized channel vector. The absolute value of the off-diagonal element g_{kl} is the signal magnitude received by the l^{th} Rx, when the BS transmits to the k^{th} Rx using the Maximum Ratio Transmission (MRT) precoding, with signal fading variation removed. This is proportional to the interference between the k^{th} and l^{th} Rx locations, assuming the MRT precoding.

As the distance between any two consecutive Rx positions is constant ($\delta = 10$ mm), the absolute values of the elements on the l-diagonal of G are also the interference signals received by the elements separated by distance $\Delta(l) = l \cdot \delta$. Therefore, we define a correlation function $\rho_j(\Delta)$, the argument of which is the distance $\Delta(l)$ between *any* two Rx locations in A_j, as the arithmetic mean of the absolute values of the elements on the l^{th} diagonal of G_j

$$\rho_j(\Delta) = \frac{\sum_{i=1}^{K-l} |g_{i,i+l}^j|}{K-l}, \tag{7.5}$$

where $g_{k,l}^j$ is the element of G^j. Due to the channel equalization (7.3), $\rho(0) = 1$, which means that the channel of any element is fully correlated with itself. If $\rho(\Delta) = 0$, then all elements separated by the distance d_l are pairwise fully decorrelated, that is, their channel vectors are orthogonal. From (7.5) and (7.4) it also follows that $\rho_j(\Delta)$ is an estimate of the average normalized power received at the distance $\Delta(l)$ from the intended receiver parallel to the Rx array. Thus, the correlation function can be viewed as a hotspot power cross-section in the direction parallel to the BS array, averaged over the location of an intended receiver in the Rx array.

7.3 Results

In this section we compare the correlation functions of the measured and simulated massive MIMO channels. On the one hand, comparing the measurements and the FS-LOS model, we quantify the effect that the multipath propagation paths have on the spatial correlation properties of the channels. On the other hand, by comparing the measured and RT-simulated channels, we demonstrate that including a generic RT environment significantly improves the accuracy of the correlation prediction, especially as the Tx-Rx distance increases.

7.3.1 RT vs. measurements

By $\hat{\rho}_j$ we denote the correlation function of the RT channel matrix of the virtual array j. 25 environment samples were simulated and in each one $\hat{\rho}_j$ was calculated with (7.5), in which the correlation matrices of the channels are given by (7.1). Similarly, by ρ_j^i we denote the correlation function measured in the array A_j^i.

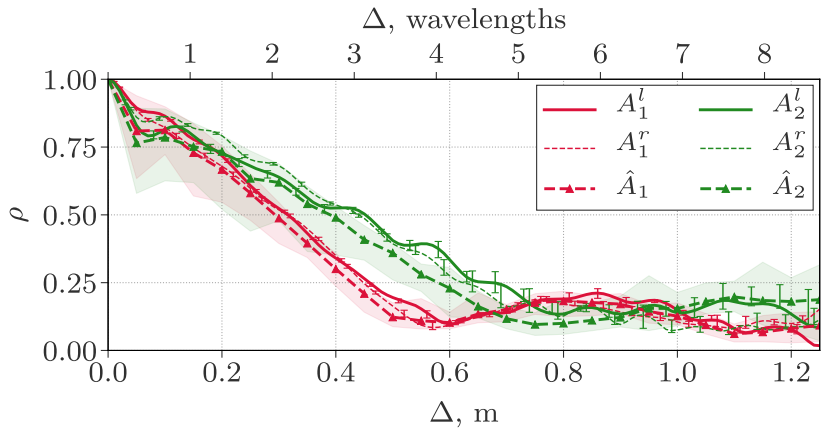

Figure 7.3: Correlation function ρ calculated using measured and simulated channels. ρ_1 and ρ_2 are shown with red and green color, respectively. The RT channels are shown with dashed with triangle markers lines and shaded regions depict $\min - \max$ range over the 25 environment samples. The measured channels are shown with solid and doted lines for A_j^l and A_j^r, respectively, and error-bars show 5-95 percentile range over subcarriers.

Fig. 7.3 compares ρ in channels obtained from the measured (A_j^l, A_j^l) and simulated $(\hat{A}_j)$ arrays for Δ up to 1.25 m.

The top axis at the Fig. 7.3 displays Δ in the units of wavelength at 2.61 GHz. In general, all presented functions are decreasing with Δ. The distance to the BS is the primary factor influencing the rate at which the correlation drops.

The measured receiver array pair (A_1^l, A_1^r) is the closest to the BS (2.2 m). ρ_1^l and ρ_1^r are similar and fall off steeper than ρ_2^l and ρ_2^r. They reach their minimum of around 0.12 at $\Delta \simeq 0.6$ m ($\simeq 4\lambda$). ρ_2^l and ρ_2^r both fall more steadily and bottom out at $\Delta \simeq 0.8$ m ($\simeq 5.5\lambda$) at a level of approximately 0.2.

The RT simulations show a very good agreement with measurements, predicting the absolute values and general behavior of the correlation functions. For A_1 arrays the largest absolute error was found at the sub-wavelength distances, where the RT underestimates the initial drop by around 0.1. The underestimation is slightly higher for A_2 arrays, but unlike the previous case, the largest absolute error of around 0.13 was observed at $\Delta \simeq 0.55$ m. To further quantify the accuracy of the RT method in predicting the correlation function, we performed the least-square fit of the Gaussian function

$$f(\Delta, \sigma) = \exp\left(-\frac{\Delta^2}{2\sigma^2}\right), \tag{7.6}$$

to ρ_j^r, ρ_j^l and $\hat{\rho}_j$ over parameter σ. By $\sigma(\rho)$ we denote the value of σ obtained after fitting (7.6) to ρ. We found that $\sigma(\rho_1^l) \simeq \sigma(\rho_1^l) \simeq 0.27$, while $\sigma(\hat{\rho}_1) \simeq 0.25$,

which means that the RT estimate relative error was around 8% at 2.2 m distance from the BS. At 3.5 m, $\sigma(\rho_2^l) \simeq 0.39, \sigma(\rho_2^l) \simeq 0.37$, and $\sigma(\hat{\rho_2}) \simeq 0.34$, which resulted in the relative error of around 10%.

7.3.2 FS-LOS vs. RT

We constructed the FS-LOS channels of all four RT-simulated receiver arrays, as described in the Section 7.2.3. We denote the correlation function derived from the FS-LOS channel matrix $H_j^{\rightarrow}$ as $\rho_j^{\rightarrow}$. Graphs of $\hat{\rho}_j$ and $\rho_j^{\rightarrow}, j \in \{1, 2, 3, 4\}$ are given at Fig. 7.4

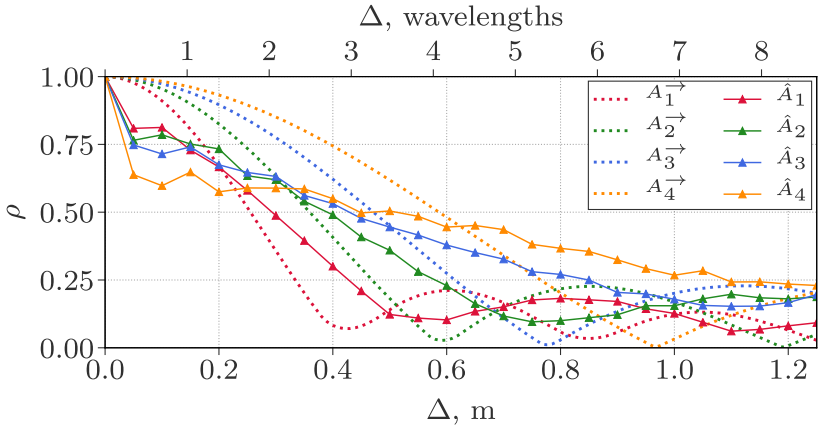

Figure 7.4: The correlation function RT/FS-LOS comparison. Graphs of $\hat{\rho}$ for full RT and FS-LOS channels are shown with solid and dotted lines, respectively. The line colors matches the color of the arrays shown in Fig. 7.1b.

The FS-LOS correlation functions overestimate the RT at smaller values of Δ and underestimate it for larger Δ. While FS-LOS model predicts a smooth concave fade-out of the correlation with Δ, the full RT simulations show an abrupt drop at $\Delta \leq 1\lambda$, followed by a nearly linear descent at larger Δ. The initial drop at a sub-wavelength scale increases in magnitude with the Tx-Rx distance: for A_4, it approaches 40%.

7.4 Conclusions

This chapter we experimentally explored the spatial correlation of the massive MIMO channels with controlled distance between the receivers. We introduced the spatial correlation function as a measure of the average correlation profile in proximity of a given location. The channels measured with the massive MIMO

test-bed were compared to the simulations using the RT method and the FS-LOS model at different separation distances between the BS and receiver.

The correlation functions calculated from the measured channels were decreasing with the inter-receiver distance, with the higher decrease rate the further the BS to receiver distance was. In general, the RT simulations show a good agreement with measurements, predicting the correlation minima and values. The FS-LOS model was unable to accurately predict the correlation profiles, overestimating their falloff at the sub-wavelength distances and underestimating their minima locations and values.

These results show that the RT-based simulations in an environment model augmented with stochastic elements are able to predict the realistic correlation properties of massive MIMO channels. Though the measurements were carried out in an indoor environment with a limited Tx-Rx distance range, their excellent agreement with the RT simulations in that range gives more credibility to the RT simulations' results conducted in Chapters 3 to 6 in different environments and at larger distances. Extending the experimental support of the RT massive MIMO simulations to more diverse environments (e.g., outdoor) and scenarios (e.g., pure non-LOS) could be a major track of the future research, as will be mentioned in the next chapter.

References

[1] J. Choi and D. J. Love. *Bounds on Eigenvalues of a Spatial Correlation Matrix*. IEEE Communications Letters, 18(8):1391–1394, 2014.

[2] Cheng-Ming Chen, Vladimir Volski, Liesbet Van der Perre, Guy AE Vandenbosch, and Sofie Pollin. *Finite large antenna arrays for Massive MIMO: characterization and system impact*. IEEE Transactions on Antennas and Propagation, 65(12):6712–6720, 2017.

[3] Steven Claessens, Cheng-Ming Chen, Dominique Schreurs, and Sofie Pollin. *Massive MIMO for SWIPT: A measurement-based study of precoding*. In 2018 IEEE 19th International Workshop on Signal Processing Advances in Wireless Communications (SPAWC), pages 1–5, 2018.

[4] Sergei Shikhantsov, Arno Thielens, Günter Vermeeren, Emmeric Tanghe, Piet Demeester, Luc Martens, Guy Torfs, and Wout Joseph. *Hybrid ray-tracing/FDTD method for human exposure evaluation of a massive MIMO technology in an industrial indoor environment*. IEEE Access, 7:21020–21031, 2019.

[5] Sergei Shikhantsov, Arno Thielens, Günter Vermeeren, Piet Demeester, Luc Martens, Guy Torfs, and Wout Joseph. *Massive MIMO Propagation Modeling With User-Induced Coupling Effects Using Ray-Tracing and FDTD*. IEEE Journal on Selected Areas in Communications, 38(9):1955–1963, 2020.

[6] Xiang Gao, Jose Flordelis, Ghassan Dahman, Fredrik Tufvesson, and Ove Edfors. *Massive MIMO channel modeling-extension of the COST 2100 model*. In Joint NEWCOM/COST Workshop on Wireless Communications (JNCW), 2015.

[7] Alex Oliveras Martinez, Elisabeth De Carvalho, and Jesper Ødum Nielsen. *Massive MIMO properties based on measured channels: Channel hardening, user decorrelation and channel sparsity*. In 2016 50th Asilomar Conference on Signals, Systems and Computers, pages 1804–1808. IEEE, 2016.

[8] Andrea P Guevara, Sibren De Bast, and Sofie Pollin. *Weave and Conquer: A Measurement-based Analysis of Dense Antenna Deployments*. arXiv preprint arXiv:2003.11467, 2020.

[9] David Mills, Jim Martin, Jack Burbank, and William Kasch. *Network time protocol version 4: Protocol and algorithms specification*. 2010.

[10] Daniel Dunbar and Greg Humphreys. *A spatial data structure for fast Poisson-disk sample generation*. ACM Transactions on Graphics (TOG), 25(3):503–508, 2006.

[11] REMCOM. *Wireless InSite 3.2.0 Reference Manual*. 2017.

Part IV

Conclusions

8 Conclusions and Future Work

This chapter concludes the dissertation by briefly summarizing the obtained results and outlining promising directions of the future research.

8.1 Conclusions

This dissertation presented several approaches for numerical modeling of the downlink human Radio Frequency (RF) Electromagnetic field (EMF) exposure to ultra-small cell and massive MIMO antenna array 5G techologies. In Part I, the exposure to a prototype ultra-small cell technology - ATTO-floor, was studied. In Part II, the exposure of users in the indoor and outdoor environments served by massive MIMO base stations was investigated. In Part III, the experimental validation of the numerical methods used in Part II is presented.

Part I

In Chapter 2, the exposure of a human worker standing on the ATTO-floor was evaluated in terms of the peak-spatial Specific Absorption Rate, averaged over 10 grams ($\mathrm{psSAR}_{10\mathrm{g}}$) of tissue in the legs. The studied ATTO-floor network operated at the center frequency of 3.5 GHz and the output power per cell was 1 mW. The Finite-Difference Time-Domain (FDTD) method with a realistic male human phantom model was used to calculate $\mathrm{psSAR}_{10\mathrm{g}}$, based on the EMF induced in its tissues. It was shown that limiting the ATTO-floor size included in the simulation domain to a patch of 4-by-4 cells underestimates the exposure induced by the

complete ATTO system by at most 2.5%. It was then established that the average ATTO-floor exposure is around 5 mW/kg, while the worst-case exposure was found to be around 21 mW/kg. These values were found to constitute no more than 0.5% of the basic restrictions for general public specified by the International Commission on Non-Ionizing Radiation Protection (ICNIRP) guidelines. The average exposure of the realistic phantoms having different body morphologies, age, and gender was found to be below the values found with the male phantom. Therefore, the ATTO-floor was concluded to comply with the existing regulations by a wide margin, largely due to the low power at which it operates.

Part II

In Chapter 3, a methodology for assessment of psSAR_{10g} in the phantom's head induced by a massive MIMO base station (BS) in an indoor environment was introduced. The EMF propagation at the frequency of 3.5 Ghz in a model of an indoor industrial environment was calculated using the RF Ray-Tracing (RT) method. Scenarios with users having the line-of-sight (LOS) propagation paths from the BS and users with no LOS paths (NLOS) were considered. The wireless channels were calculated based on the RT results, showing that the NLOS scenarios offered more favourable propagation conditions for the massive MIMO system, as indicated by lower channel matrix condition numbers and higher matrix power ratios of the channel correlation matrix, compared to the LOS scenarios. In addition, the EMF enhancement (hot-spot) resulting from the BS precoding its transmission with the Equal Gain Transmission scheme, was evaluated in free space. The average EMF hot-spot size was found to be around 51 mm, or 0.59λ at 3.5 GHz, in both LOS and NLOS scenarios. The EMF gain, expressed in terms of the time-averaged power flux density in the hot-spot normalized to its non-precoded value, was found to be around 14 dB in both LOS and NLOS. The psSAR_{10g} in the head to the free-space hot-spot EMF was evaluated and based on that a maximum permissible BS output power satisfying the ICNIRP basic restrictions was derived. At the distance of 8 m, the maximum permissible BS power was found to be 35 W and 110 W for the LOS and the NLOS scenarios, respectively.

In Chapter 4, the approach developed in Chapter 3 was extended to account for the presence of the user head in proximity of the user equipment (UE). Influence of the head on the massive MIMO channel matrix, and thus precoded transmission, was included in the model by simulating the radiation pattern of the UE coupled with the head, at the distance of 20 mm from it, using the FDTD method. The results showed that presence of the head has a positive impact on the massive MIMO channel properties, decreasing for up to 30% the channel correlation between the UEs that are close to each other. The BS was transmitting using the Maximum Ratio Transmission precoding scheme. The hot-spot time-averaged power flux

density enhancement relative to its value at the location symmetrical with respect to the head sagittal plane, was found to be around 10 dB, taken over the exposure sample average. The psSAR_{10g} location was highly correlated with the position of the UE (relative to the head), and in around 78% of the exposure evaluations was found in its closest vicinity. The psSAR_{10g} normalized to the time averaged power flux density in the hot-spot was compared to the same quantity derived from the ICNIRP basic restrictions and reference values. The hot-spot normalized psSAR_{10g} was found to be on average 5 dB lower that the value derived from the ICNIRP guidelines. This means that the ICNIRP incident power density reference is conservative in the context of massive MIMO, i.e. the massive MIMO hot-spot with the peak power density level equal to the ICNIRP reference induces, on average, 5 dB lower psSAR_{10g} than that of the ICNIRP basic restrictions.

In Chapter 5, the methodology developed in Chapters 3 and 4 is applied to study and compare the exposure induced by a distributed and a collocated massive MIMO arrays. A model of an industrial indoor environment was proposed, in which the distributed massive MIMO BS deployment was uniformly covering the entire ceiling surface, while the collocated BS was a compact ($\lambda/2$ element separation distance) uniform linear array, positioned in the center of the ceiling, both operating at 3.5 GHz frequency. It was shown that in scenarios when the phantom head blocks the LOS paths from the UE to the collocated BS, the latter was not able to produce compact hot-spots. At the same time, the instantaneous hot-spots produced by the distributed BS rarely exceeded 100 mm (around 1.1λ) in size. In addition, the UE was positioned at a varying distance from the phantom's head. Importantly, it was found that for short UE-to-head distances (e.g., 7 mm), the hot-spot maximum location does not coincide with the UE. An explanation was proposed based on the analysis of the UE radiation pattern as a function of its distance from the head. The exposure of a phantom in a series of consecutive locations across the environment was evaluated in terms of psSAR_{10g} normalized to the time-averaged power flux density assessed at either the hot-spot peak, or the UE location. The psSAR_{10g} normalized to the hot-spot peak EMF level was found to be around 12 dB lower with the collocated BS, and from 13 dB to 14 dB lower with the distributed BS, than the ICNIRP reference. This is at least 7 dB lower than the results of Chapter 4, possibly due to a larger number of the BS antennas used in this chapter's system modeling. However, if the EMF is assessed at the UE location, the normalized psSAR_{10g} closely approaches the ICNIRP reference (and exceeds it at the 2 mm UE-to-head distance, in the collocated BS array configuration). The importance of accurately specifying the location in which the EMF is assessed (e.g., in experimental compliance testing) is pointed out.

In Chapter 6, an outdoor urban environment with a single BS capable of the multi-user codebook beamforming, Maximum Ratio and Zero-Forcing massive MIMO transmission precoding schemes was studied. The exposure of users in

the environment was assessed in terms of the time-averaged BS array gain. It was evaluated by first, simulating the propagation in the environment with the RT method, then modeling the user scheduling stochastically, and finally generating and averaging the array radiation patterns, according to one of the BS transmission regimes. The statistical distributions of the maximum time-averaged BS gains, calculated for different numbers of the simultaneously active UEs and the BS array elements, were presented and analyzed with respect to their theoretical maximum values. The results showed lower maximum time-averaged gain values for the BS arrays with larger number of elements (e.g., 100) compared to those with a smaller number of elements (e.g., 16) regardless of the transmission scheme. It was also found that the massive MIMO transmission schemes always result in lower time-averaged gain values with larger numbers of the simultaneously served UEs. At the same time, the opposite was observed with the beamforming BS that had 16 or fewer elements and was serving fast-switching UEs. The lowest average maximum time-averaged gain (around 6% of the theoretical maximum) was produced by the Zero-Forcing BS having the largest studied element count (100), and transmitting to 10 UEs concurrently.

Part III

In Chapter 7, the spatial correlation of the massive MIMO channels was studied experimentally. The channels measured with the massive MIMO test-bed were compared to the simulations using the RT method and the free-space LOS model at different separation distances between the BS and receiver. The spatial correlation function was introduced as a measure of the average correlation profile in proximity of a given location. The correlation functions calculated from the measured channels were decreasing with the inter-receiver distance, with the higher decrease rate the further the BS to receiver distance was. In general, the RT simulations showed a good agreement with measurements, predicting the correlation minima and values. The free-space LOS model was unable to accurately predict the correlation profiles, overestimating their falloff at the sub-wavelength distances and underestimating their minima locations and values.

8.2 Future work

The results presented in Parts II and III of this thesis can be potentially extended in several ways, some of which are briefly outlined below.

8.2.1 Huygens' box approach in FDTD

One major improvement in the accuracy of the FDTD hot-spot modeling can be achieved by realizing the Huygens' box RT-FDTD hybridization interface [1],

that could replace the plane-wave-based FDTD excitation proposed in Chapter 3. This will allow introducing highly complex and inhomogeneous EMF excitations into the FDTD domain, e.g. in scenarios when the RT rays' reception spheres intersect the FDTD domain only partially. Such scenarios are especially relevant for the mmWave technologies (short wavelengths), or when the EMF distribution around the entire phantom model is of interest (large FDTD domain size). However, this approach is computationally challenging, especially at high domain size to wavelength ratios, as every boundary FDTD grid cell has to be represented by a receiver in the RT simulation. A thorough performance optimization of the complete simulation pipeline will have to be performed.

The new approach can then be applied to study the exposure of the future (6G) wireless communication technologies, such as the holographic massive MIMO and Intelligent Reflecting Surfaces [2, 3], e.g. in context of the SHAPE project. In these systems, the number of independently controlled antennas and their surface density are so high that practically continuous wavefronts of arbitrary shape can be radiated towards users. The Huygens' box approach is very well suited for introducing such wavefronts in the FDTD domain, to further evaluate the interaction of the resulting EMF with realistic human phantoms.

8.2.2 Realistic environment models

Throughout the dissertation, simplified environment models were used to model the EMF propagation with the Ray-Tracing method. In the future, more realistic environments will be studied, e.g., site-specific scenarios of potential 5G deployments. The environment will be constructed based on the openly available 3D GIS data obtained with Light Detection And Ranging (LiDAR) scanning, photogrammetry methods or a combination thereof [4]. Raw meshes obtained using LiDAR scanning or aerial imaging photogrammetry contain millions of facets per square kilometer, making them unusable directly in the Ray-Tracing simulations. To render it suitable for the RF propagation modeling at sub-6GHz and mmWave (26-28 GHz, 140 GHz) frequencies, the geometry will be segmented and simplified, e.g., using the level of detail generation algorithms [5]. Frequency-specific dielectric material properties to facets will be assigned to the simplified geometry facets, e.g., based on their texture color or entity type. Lastly, accurate vegetation data will be extracted, improving the modeling accuracy, particularly at the mmWave frequencies.

8.2.3 Future exposure metrics

In Chapters 2 to 6, the main dosimetric quantity was the peak-spatial Specific Absorption Rate (SAR) averaged over a 10 g cube, in line with the ICNIRP guidelines below 6 GHz. However, as was shown in Chapters 2, 4 and 5, most of the time the peak cube was found in the ear close to the receiver in the hot-spot or in the toes

close to the transmitting antennas. Due to the geometrical features of the ear and the definition of the averaging procedure, such peak-cubes are mostly filled with air and often contain disconnected sections of the phantom body. An alternative approach could be to assess the organ-specific SAR [6], e.g. in the brain or the ear cartilage tissue. This metric account for the anatomical features and assures spatial continuity during the absorption averaging. Absorbed power density was introduced as the new restricted quantity at frequencies above 6 GHz in the most recent ICNIRP guidelines release [7]. It accounts for a short EMF penetration depth into the biological tissues at higher frequencies. Being a surface-averaged quantity, it could allow more efficient numerical assessment methods, compared to SAR.

8.2.4 Realistic network-level effects

One particularly important aspect of the real massive MIMO operation, with regard to the downlink exposure, is the imperfect channel state knowledge at the base station. The simulations and analysis conducted in Chapters 3 to 5 assumed that the channel matrix is known exactly at any given moment, and the BS is able to calculate the transmission weights accordingly. In reality, however, this is never the case. First, the channel state is quantized before sent uplink by the user equipment, as only a limited portion of the time-frequency resources can be allocated for that to avoid excessive overhead. In addition, noise and (inter-cell) interference introduce errors to the channel estimates [8, 9]. As a result, the BS transmission may differ significantly from the model case, which is likely to alter the location and shape of hot-spots the BS creates. These effects can be studied by combining the RT (exact) channel prediction and the massive MIMO network model that accounts for the channel estimate uncertainty.

8.2.5 Direct hot-spot EMF measurements

In the measurement campaign presented in Chapter 7 the correlation of the channel vectors of a receiver at different locations was used to derive the spatial correlation profiles, which were then linked to the EMF hot-spot shape. This approach has several drawbacks. First, the EMF (e.g., the E-field, which is the quantity of interest in exposure assessment) is not measured directly, but indirectly derived after the fact from the recorded channel state. Second, the receiver antenna had only one (vertical) polarization, and was not calibrated, i.e. its antenna factor was unknown. Third, The movement of the positioner itself (mostly metal) also altered the channel, and this uncertainty was not accounted for. The aspects outlined above will be improved upon in the next measurement campaign. A calibrated 3-axial E-field probe in combination with a spectrum analyzer (e.g. NARDA SRM-3006) is going to be used to measure the frame-averaged E_{RMS} over each sub-carrier bandwidth and derive the the 6-minute time-averaged values, according to the ICNIRP guidelines. The

effect of the positioning system movement on the channel state will be quantified using the method developed in Chapters 3 and 4 and minimized, e.g., by increasing the probe to any moving part of the positioner, covering the positioner with the EMF-absorbing pads, etc. The actual disruption of the channel state is then going to be measured to validate to the simulated data.

References

[1] Sébastien Reynaud, Rodolphe Vauzelle, Alain Reineix, and Christophe Guiffaut. *A hybrid FDTD/UTD radiowave propagation modeling: Application to indoor channel simulations*. Microwave and Optical Technology Letters, 49(6):1312–1320, 2007.

[2] Emil Björnson, Luca Sanguinetti, Henk Wymeersch, Jakob Hoydis, and Thomas L. Marzetta. *Massive MIMO is a reality-What is next?: Five promising research directions for antenna arrays*. Digital Signal Processing, 94:3 – 20, 2019. Special Issue on Source Localization in Massive MIMO.

[3] Qingqing Wu and Rui Zhang. *Intelligent Reflecting Surface Enhanced Wireless Network via Joint Active and Passive Beamforming*. IEEE Transactions on Wireless Communications, 18(11):5394–5409, 2019.

[4] Ruisheng Wang. *3D building modeling using images and LiDAR: A review*. International Journal of Image and Data Fusion, 4(4):273–292, 2013.

[5] Yannick Verdie, Florent Lafarge, and Pierre Alliez. *LOD generation for urban scenes*. ACM Transactions on Graphics, 34(ARTICLE):30, 2015.

[6] Arno Thielens, Günter Vermeeren, Wout Joseph, and Luc Martens. *Stochastic method for determination of the organ-specific averaged SAR in realistic environments at 950 MHz*. Bioelectromagnetics, 34(7):549–562, 2013.

[7] International Commission on Non-Ionizing Radiation Protection et al. *Guidelines for limiting exposure to Electromagnetic Fields (100 kHz to 300 GHz)*. Health Physics, 118(5):483–524, 2020.

[8] Luca Sanguinetti, Emil Björnson, and Jakob Hoydis. *Toward Massive MIMO 2.0: Understanding Spatial Correlation, Interference Suppression, and Pilot Contamination*. IEEE Transactions on Communications, 68(1):232–257, 2020.

[9] Emil Björnson and Luca Sanguinetti. *Power scaling laws and near-field behaviors of massive MIMO and intelligent reflecting surfaces*. IEEE Open Journal of the Communications Society, 1:1306–1324, 2020.

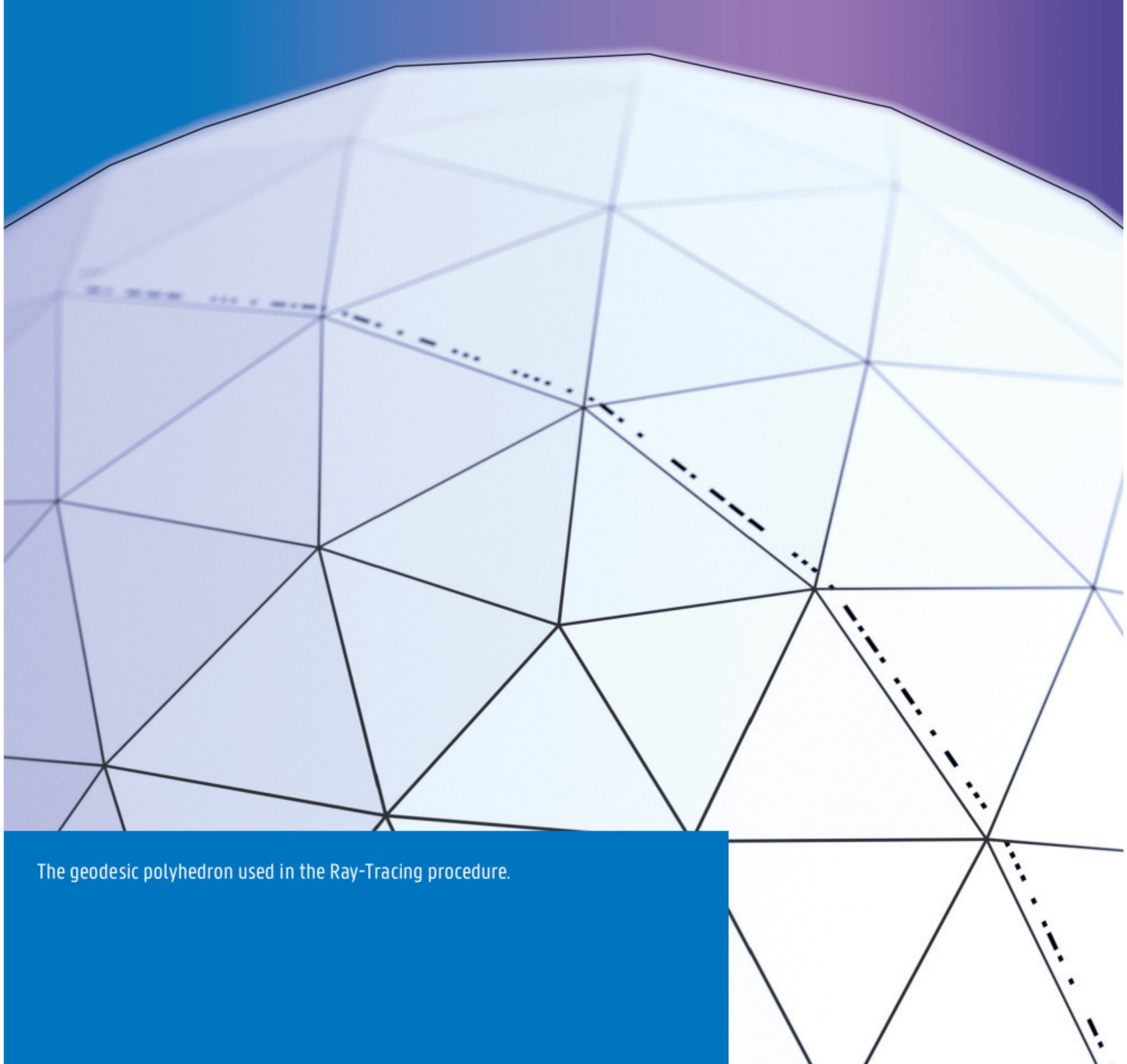

The geodesic polyhedron used in the Ray-Tracing procedure.